INVESTIGATIONS ON ELECTROMAGNETIC INTERFERENCE SHIELDING BEHAVIOUR OF GRAPHENE BASED POLYPYRROLE NANOCOMPOSITES

THESIS SUBMITTED FOR THE FULFILMENT OF THE DEGREE OF

DOCTOR OF PHILOSOPHY (Ph.D.)

IN

PHYSICS

BY

NISHA GILL

(Reg. No. 901412001)

under the supervision of

Dr. DWIJENDRA P. SINGH
(ASSOCIATE PROFESSOR)

PROF. O. P. PANDEY
(SENIOR PROFESSOR)

SCHOOL OF PHYSICS AND MATERIALS SCIENCE
THAPAR INSTITUTE OF ENGINEERING AND TECHNOLOGY

PATIALA, PUNJAB, INDIA

OCTOBER 2020

DECLARATION

Certified that the thesis entitled "**INVESTIGATIONS ON ELECTROMAGNETIC INTERFERENCE SHIELDING BEHAVIOUR OF GRAPHENE BASED POLYPYRROLE NANOCOMPOSITES**" submitted by Ms. Nisha Gill is in fulfilment for the degree of Doctor of Philosophy of this university. This work has been done under the supervision of Dr. Dwijendra P. Singh, Associate Professor and Prof. O. P. Pandey, Senior Professor, School of Physics and Materials Science (SPMS), Thapar Institute of Engineering and Technology, Patiala, Punjab. The work presented in this thesis is original to the best of our knowledge and has not been submitted for any other degree of this or any other university.

(Nisha Gill)
(Candidate)

(Dwijendra P. Singh)

(O. P. Pandey)

Supervisors

ACKNOWLEDGEMENT

I would like to express my deep and sincere gratitude to my supervisors Dr. Dwijendra P. Singh, Associate Professor and Prof. O. P. Pandey, Senior professor, School of Physics and Materials Science (SPMS), Thapar Institute of Engineering and Technology, Patiala, for their invaluable guidance at every stage of research work. My deepest thanks to Dr. Dwijendra P. Singh, a genius person who continually and convincingly conveyed a spirit of experimentation and persistence with regard to my research work. It was a great privilege and honour to work and study under his guidance. My cordial thanks is also to Prof. O. P. Pandey for his support, suggestions and initiatives in garnering scholarship for my research work.

I am also grateful to Dr. Amit Lochan Sharma, Principal Scientist, CSIO-Chandigarh, Dr. Vinay Gupta, Professor, University of Delhi and Dr. Monika Tomar, Assistant Professor, University of Delhi for their support, encouragement and guidance. I would like to thanks the IRB committee members, Dr. Puneet Sharma, Dr. Bhaskar Chadra Mohanty and Dr. Rajeev Mehta for their encouragement, insightful comments, and helpful suggestions.

A very special thanks to my close friends Ms. Navneet Kaur, Ms. Shobhneek Kaur, Ms. Indu Gupta and Ms. Meenu Singla for their genuine support (academic, emotional and humorous) in this prolonged research endeavour. I like to extend my thanks to my talented and youthful lab mates Mr. Sachin Jaidka and Ms. Lovepreet Kaur Dhugga, for their contribution throughout my research work.

I appreciate the help received from the faculty and the supporting staff of SPMS, library and, laboratories to complete this thesis successfully. Financial support of project under the Department of Electronics and Information Technology (DeitY) is highly acknowledged.

I am extremely grateful to my father (Mr. Jagat Singh) and mother (Mrs. Nirmla Dahiya)for their love and sacrifice in bringing me up and encouragement throughout my life and career. I am thankful to my father-in-law (Mr. Suresh Kumar Gill) and mother-in-law (Mrs. Jagmaya Gill) for providing support in my prolonged research project. I am thankful to my husband (Mr. Sumit Gill) for providing emotional support in this endeavour. My special thanks to my brother (Mr. Adwait Dahiya) for his support, encouragement and care at every stage of my life. I am thankful to bhabhi (Mrs. Tanuja

Dahiya) and sister in law (Mrs. Suruchi Gill Balyan) for their love and cooperation. I am appreciative to my relatives, friends and siblings for their love and blessings. Special thanks to my daughter (Aadhya) for her unbound love and unspeakable patience exhibited during this research assignment.

My sincere thanks to all the people who have supported me in completing my research work and the ALMIGHTY.

(Nisha Gill)

PREFACE

The electromagnetic interference (EMI) shielding of different electronic gadgets have attracted a lot of attention due to its various applications in industries, defence and electronic communication. The electromagnetic interference present in the environment through different possible ways may also affect the human health. Therefore, essentiality of EMI shielding has also been considered for checking the electromagnetic pollution. In order to attenuate the electromagnetic radiation, a shielding material is required. The electromagnetic shielding is done by three ways i.e. reflection, absorption and multiple reflection. The ability of a material to attenuate the intensity of electromagnetic wave is given by shielding effectiveness (SE). The total SE greater than 30 dB corresponds to 99.9 % attenuation of microwave radiation and is useful for various defence, military applications. Metals, ceramics and various other composites have been investigated in the quest of vary good EMI shielding materials. These composites have several advantages such as low cost, easy to process, free from corrosion etc. There are several frequency bands of microwave defined by Radio Society of Great Britain (RSGB) such as L, C, X, Ku band etc., which are important for different specific purposes ranging from defence to atmospheric science, microwave communication to checking of environmental pollution etc. The X-frequency band of microwave (8.2-12.4 GHz) is useful for many commercial and military application such as Doppler weather radar, TV transmission etc. These applications require high shielding due to absorbing along with decreased shielding due to reflection.

The materials having high dielectric permittivity and high magnetic permeability may having very good microwave absorbing properties by virtue of presence of electric and magnetic dipoles. When the electromagnetic wave interact with these dipoles, the electromagnetic field of electromagnetic wave may lead/lag with respect to the internal field of these dipoles which causes the attenuation of electromagnetic wave.

Therefore, the nanocomposite materials consisting of conducting polymer and carbon based nanofillers along with ferrite nanoparticles could be an alternative choice of EMI shielding material. These materials may exhibit very good microwave absorbing behaviour in the X-band. Therefore, investigations on electromagnetic shielding behaviour of graphene based polypyrrole nanocomposites have been carried out. The

basic, analysis and outcome of these investigations are compiled in five chapters in the present thesis.

The first chapter discuss the fundamentals of electromagnetic theory and its relevance to the electromagnetic interference (EMI) shielding phenomena. A brief review of different class of EMI shielding materials (*viz.* metals, ceramic, ceramic based composites and polymer based composite materials) are also presented. The role of the interfacial modification, dielectric and magnetic losses, mechanical strength have significant effect on the shielding effectiveness behaviour of the polymer based composite. These studies are helpful in deciding the aim of thesis, which is mentioned in the last section of this chapter.

The second chapter describes the various methods and experimental techniques used for synthesis and characterization of graphene based polypyrrole nanocomposites. Synthesis of cobalt ferrite nanoparticles and graphene nanosheets have been done by hydrothermal method and liquid phase exfoliation method respectively. Synthesis of the polypyrrole based nanocomposites is carried out by *in-situ* chemical oxidative polymerization technique. Structural and morphological characterization have been done by X-ray diffraction (XRD), transmission electron microscopy (TEM), Fourier transform infrared (FTIR) and Raman spectroscopy. The magnetic measurement has been studied by vibrating sample magnetometer (VSM). The brief description of all these characterization techniques are also included in this chapter. Electrical studies has been done by current-voltage measurements at room temperature. The electromagnetic shielding effectiveness, dielectric and magnetic parameters in X-band (8.2-12.4 GHz) have been measured by vector network analyzer (VNA). The various parameters associated with EMI shielding such as dielectric permittivity, magnetic permeability, ac conductivity and skin depth are explained in the last portion of this chapter.

Third chapter discusses the electromagnetic shielding behaviour of polypyrrole-graphene nanocomposite in X-band. The polypyrrole-graphene nanocomposites have been synthesized by *in-situ* chemical oxidative polymerization method. X-ray diffraction, transmission electron microscopy, Fourier transform infrared and Raman spectra have been carried out for structural and morphological studies. The electromagnetic shielding and dielectric relaxation behaviour of nanocomposite have been investigated in X-band (8.2-12.4 GHz) of microwave. Microwave absorption and reflection behaviour have been

analyzed and, correlated with the dielectric permittivity, skin depth, ac conductivity and attenuation constant. The qualitative explanation of mechanism of observed shielding effectiveness by various processes is also given. This chapter is concluded with important outcomes of experimental results.

Fourth chapter deals with the investigation on the effect of inclusion of graphene nanosheets on EMI shielding behaviour of polypyrrole-cobalt ferrite-graphene nanocomposite in X-band. Polypyrrole-cobalt ferrite-graphene nanocomposites have been synthesized by *in-situ* chemical oxidative polymerization. The formation of nanocomposites with different loading percentage of graphene have been confirmed by X-ray diffraction, Fourier transform infrared and transmission electron microscopy. The effect of graphene loading in nanocomposite on shielding effectiveness, dielectric permittivity, magnetic permeability, ac conductivity and skin depth has been studied in X-band (8.2-12.4 GHz). Mechanism of shielding effectiveness by various processes i.e. reflection, absorption, multiple reflections etc. is also illustrated qualitatively. This chapter is concluded with important outcomes of experimental results.

The summary and the conclusions drawn from the study of investigation of electromagnetic interference shielding of graphene based polypyrrole nanocomposites has been given in the fifth chapter. The future scope for further investigation has also been suggested.

LIST OF PUBLICATIONS

1. Enhanced microwave absorption and suppressed reflection of polypyrrole-cobalt ferrite-graphene nanocomposite in X-band.

   Nisha Gill, Amit L. Sharma, Vinay Gupta, Monika Tomar, O. P. Pandey, Dwijendra P. Singh.

   Journal of Alloys and Compound **797** (2019) 1190-1197.

2. Improved electromagnetic shielding behaviour of graphene encapsulated polypyrrole-graphene nanocomposite in X-band.

   Nisha Gill, Vinay Gupta, Monika Tomar, Amit L. Sharma, O. P. Pandey, Dwijendra P. Singh.

   Composite Science and Technology **192** (2020) 108113.

LIST OF CONFERENCES

1. **Nisha Gill**, Dwijendra P. Singh, "In-situ synthesis and characterization of polypyrrole-ferrite nanocomposite", 2nd **conference on microscopy in materials science** (AMST) held at Thapar Institute of Engineering and Technology, Patiala, 2016 (Poster presentation).

2. **Nisha Gill**, O. P. Pandey and Dwijendra P. Singh "Microwave Shielding Behaviour of Graphene based Polypyrrole nanocomposite", **6th Global Nanotechnology Congress and Expo** held in Dubai, 2019 (oral presentation).

3. **Nisha Gill**, O. P. Pandey and Dwijendra P. Singh, "Microwave absorption Behaviour of Graphene based Polypyrrole nanocomposite", **International Conference on Advanced Materials (ICAM)** held at Nirmalgiri College, Kerala, 2019 (Poster presentation) .

4. **Nisha Gill**, Navneet Kaur, Amit L. Sharma, Vinay Gupta, Monika Tomar, O. P. Pandey and Dwijendra P. Singh, "Microwave Absorption and Reflection Behaviour of Polypyrrole-PMMA-$Co_{0.5}Ni_{0.5}Fe_2O_4$ Nanocomposite in X-band", **64th *DAE* Solid State Physics Symposium**, Indian Institute of Technology Jodhpur, 2019 (Poster presentation).

CONTENTS

LIST OF FIGURES

CHAPTER 4

LIST OF TABLES

CHAPTER 1

INTRODUCTION

1.1. INTRODUCTION

Electromagnetic interference (EMI) has become a severe concern due to modern development in communication, electronic devices etc. This affect the performance of the device as well as human health [1–4]. A new terminology "electromagnetic pollution" is emerging as a topic of investigation due to effect of electromagnetic (EM) wave on human health [1,4–6]. This problem is overcome by electromagnetic shielding, where a barrier of material is placed that hinders the electromagnetic wave to interfere with the performance of electronic equipments.

The materials applied for this purpose are called as electromagnetic interference (EMI) shielding materials and the ability of a shielding material is quantified by a physical quantity called shielding effectiveness. Shielding effectiveness (SE) is the ability of a material to attenuate the intensity of electromagnetic wave. A SE of 20 dB which corresponds to 99% attenuation of microwave radiation, is useful for various electronic applications, whereas for defence applications SE should be greater than 30 dB which corresponds to 99.9% attenuation [7]. There are wide class of materials which are being used for EMI shielding purposes i.e. metals [8], ceramics [9], ceramic-ceramic composite [10], polymer-ceramic composites [11], carbon based ceramic composites [11] and carbon based polymer composites [12].

The electromagnetic shielding is mainly done in three ways i.e. reflection, absorption and multiple reflection. Reflection is the primary mechanism of EM shielding. Reflection occurs when the shielding materials have charge carriers such as holes and electrons which create impedance mismatch between the impedance of free space and the impedance of shielding material. Metals are the shielding materials where EMI shielding is mainly dominated by reflection. Metals have good shielding effectiveness along with good mechanical properties [13,14]. The metals are generally based on the faraday cage principle in which the EM wave creates the charges on the surface of cage which is cancel by the charges inside the cage [15]. Metals are good conductors, therefore they are best reflecting materials. But they have the disadvantages such as heavy weight, poor processibility, exposure to corrosion etc [16,17]. The second mechanism of shielding is absorption where ohmic losses occurs by the heating of material due to the induced current in the material. This is caused by the attenuation of electromagnetic wave by its interaction with magnetic and electric dipoles present inside the material [7,18–21]. Historically, the need of microwave absorbing or electromagnetic shielding materials have emerged during second world war for strengthening the defense related equipment

such as RADAR, fighter jets, submarines etc. [22–24]. The third mechanism is multiple reflection, where the electromagnetic wave is reflected multiple times back and forth and get attenuated [25]. There are several frequency bands of microwave defined by Radio Society of Great Britain (RSGB) such as L, C, X, Ku Band etc., which are important for different specific purposes ranging from defense to atmospheric science, microwave communication to checking of environmental pollution etc. [26–30]. Shielding behaviour of a material in X-band (i.e. 8.2-12.4 GHz) frequency range of microwave is of particular importance in Doppler weather radar, TV transmission, vehicular detection, defense etc. [22,27,31–33]. High shielding due to absorption (SE_A) along with negligible shielding due to reflection (SE_R) is important for aerospace applications, better known as "stealth technology" where microwave transmitter does not have capability to locate the position and velocity of aircraft [22]. For a material with good microwave absorption and suppressed reflection, the composite based on intrinsically conducting polymers have emerged as favourable materials. Carbon nanofillers based polymer nanocomposites have been observed as a promising material for EMI shielding by virtue of their good mechanical strength, electrical and thermal behaviour, light weight, low cost and ease of processing etc [34–39].

To resolve the issues associated with optimization of EMI, international Special Committee on Radio interference has been formed in 1934 and has given the rules for controlling the EMI in the electrical and electronic devices [15]. According to the guidelines, EMI shielding effectiveness should be greater than 30 dB for commercial applications which corresponds to 99.9% of the incident radiation.

This chapter briefly discusses about the theory of electromagnetic wave and mechanism of electromagnetic interference shielding. The shielding behaviour of different class of materials have been briefly reviewed. This chapter also, concludes with the aim of thesis.

1.2. THEORY OF ELECTROMAGNETIC WAVE

The electromagnetic (EM) wave contains the electric and magnetic vector orthogonal to each other. The electromagnetic wave propagates in a direction perpendicular to the electric and magnetic field vector. The ratio of electric field to magnetic field strength gives the wave impedance (Z), which comes out to be ~ 377 Ohm in free space. The electromagnetic wave characteristics depends upon the distance from the source and the nature of source. The distance from the source is divided into two regions i.e. the near field region, where the distance from the source is less than $\lambda/2\pi$ and the wave in near

field region has spherical wave front and the second region is far field region where the distance from the source is greater than λ/2π. Here, λ is the wavelength of electromagnetic wave. In the far field region, the curvature of radiated EM wave is lost and become plane wave. The radiation field i.e., the intensity of electric field and magnetic field, depends on the medium in which the electromagnetic wave is propagating. The medium at a distance λ/2π from the source which is between far field and near field is called as the transition region [40]. In the near field, if the voltage is high and the current is low, then the EM wave is magnetic field (H) dominated. If current is high and voltage is low, the EM wave is electric field (E) dominated. The plane electromagnetic wave strike the interface between two media having different impedances. The reflection loss will be higher when the impedance mismatch between two media is higher [41].

In this thesis, we are discussing about the plane electromagnetic wave for EM shielding applications.

The electric and magnetic vector for a plane electromagnetic wave in x-direction is given by equations:

$$\vec{E} = E_y(x,t)\vec{\mathbf{j}} = E_o \cos(\mathrm{kx} - \mathrm{wt})\vec{\mathbf{j}} \quad \text{.....(1.1)}$$

$$\vec{H} = H_z(x,t)\vec{k} = H_o \cos(kx - wt)\vec{k} \quad \text{.....(1.2)}$$

where E_o and H_o are the amplitudes of the electromagnetic wave.

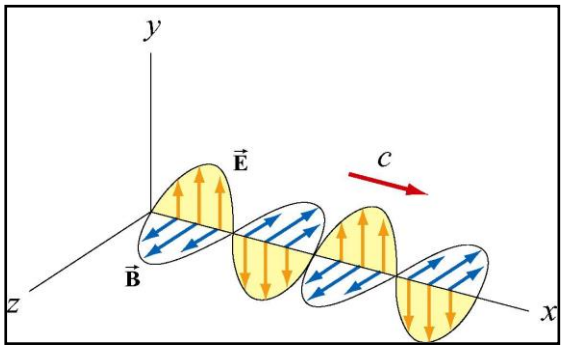

Fig. 1.1 The plane electromagnetic wave with electric and magnetic vector perpendicular to each other [40].

The propagation of plane electromagnetic wave is shown in Fig. 1.1 where the plane wave is propagating in x-direction with electric field vector in y-direction and magnetic field vector in z-direction. The propagation of electromagnetic wave depends on the intrinsic impedance and is given as

$$\eta = \sqrt{\frac{j\omega\mu}{\sigma + j\omega\varepsilon}} \quad \text{.....(1.3)}$$

In case of dielectric material, $\sigma \ll j\omega\varepsilon$, then $\eta = \sqrt{\mu/\varepsilon}$. This shows that the intrinsic impedance depends on the dielectric permittivity and the magnetic permeability.

In case of conductor, $\sigma \gg \omega\varepsilon$, then

$$\eta = \sqrt{\frac{j\omega\mu}{\sigma}} = (1+j)\sqrt{\frac{\pi\mu f}{\sigma}} \quad \text{.....(1.4)}$$

Now, the propagation constant can be defined as

$$\gamma = (\alpha + i\beta) = \sqrt{j\omega\mu(\sigma + j\omega\varepsilon)} \quad \text{.....(1.5)}$$

where α is the attenuation constant and β is the phase constant of EM wave.

In case of good conductor, $\gamma = \sqrt{j\omega\mu} = (1+j)\sqrt{\pi\mu f\sigma}$ and $\alpha = \beta = \frac{1}{\delta} = \sqrt{\pi\mu f\sigma}$ where δ is the skin depth of the material. Skin depth is defined as the distance in the material at which the amplitude of EM wave decreases to 1/e of its maximum amplitude.

1.3. PRINCIPLE OF EMI SHIELDING

The materials applied for the purpose of electromagnetic interference (EMI) shielding are characterized by a physical quantity called shielding effectiveness. The following subsection discusses about the shielding effectiveness.

1.3.1. EMI shielding effectiveness

The ability of attenuation of electromagnetic wave is known as EMI shielding effectiveness of a shielding material. It is expressed as the ratio of incident field strength to the transmitted field strength and is expressed as [42]:

$$SE = 10\log\left(P_{in}/P_o\right) \quad \text{.....(1.6)}$$

$$SE_E = 20\log\left(E_{in}/E_o\right) \quad \text{.....(1.7)}$$

$$SE_H = 20\log\left(H_{in}/H_o\right) \quad \text{.....(1.8)}$$

where P_{in}, P_o, E_{in}, E_o, H_{in} and H_o are the plane wave field strength, electric field and magnetic field strength of incident and transmitted EM wave from the EMI shielding material respectively. Here, SE, SE_E and SE_H are denoting as total shielding effectiveness, shielding effectiveness by electric field and shielding effectiveness by magnetic field respectively. The SE is measured in terms of decibels (dB). Considering the equation 1.6, the shielding effectiveness of 20 dB corresponding to 99% attenuation and shielding effectiveness of 30 dB corresponds to 99.9 % attenuation of EM wave. Total shielding effectiveness is the contribution of all the shielding effectiveness due to reflection loss, absorption loss and the multiple reflection loss of the material and is given as:

$$SE = SE_R + SE_A + SE_M \quad \text{.....(1.9)}$$

The subsequent subsection is giving the details about the mechanism involved in EMI shielding.

1.3.2. EMI shielding mechanism

When a plane electromagnetic wave is incident on the surface of a material, some wave is

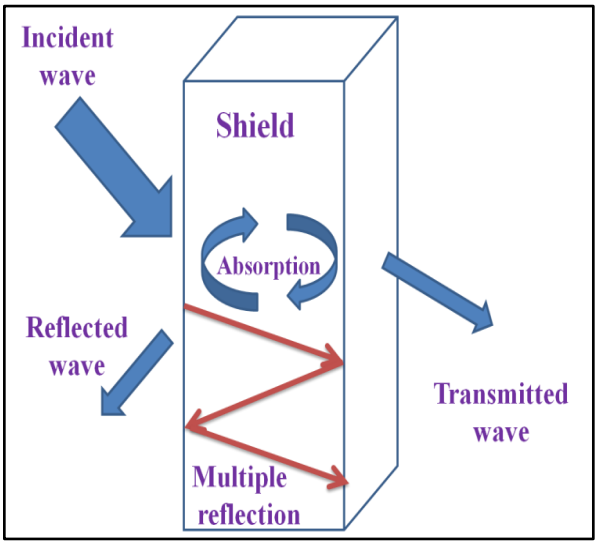

Fig. 1.2 Mechanism of electromagnetic shield.

reflected back in same environment, some is absorbed by material, some suffers multiple reflection inside the material. Fig. 1.2 represents the mechanism of electromagnetic shielding. Remnant EM wave after all these processes transmitted through the material. The part of incident wave reflected by the surface of the material is given by reflection coefficient. The conducting materials like metals are suitable for reflection as they contains mobile charge carriers. The mobile charge carriers create impedance mismatch between the impedances of free space and the shield. Because of the impedance mismatch, most of the incident EM wave is reflected from the shield. The part of incident wave is transmitted through the medium, the amplitude of the wave decreases by the factor $e^{-\alpha/x}$ (EM wave is represented as it is propagating along x-axis) where α is the attenuation constant and is also called as absorption loss. If the skin depth is less than the shielding material, the EM wave re-reflected by the surfaces of the material and finally absorbed, which is called as multiple reflection. Shielding by reflection, absorption and multiple reflection are described in the subsequent subsections.

1.3.3. Shielding by Reflection

Reflection is the primary mechanism of EM wave and it occurs when the shielding material have charge carriers such as electrons and holes which create impedance mismatch between free space and shielding material. The reflection depends on conductivity of material and frequency of propagation. The shielding effectiveness by reflection is given by [43]:

$$SE_R(dB) = 10log\left(\frac{\sigma_{ac}}{16\omega\varepsilon_0\mu'}\right) \quad \text{.....(1.10)}$$

where σ_{ac} is the ac conductivity, ω is the angular frequency and μ' is the real part of relative permeability. Wave impedance (Sec. 1.2) presents how the relative permeability and permittivity (material properties) can affect the reflection coefficient.

1.3.4. Shielding by Absorption

The secondary mechanism of electromagnetic shielding is absorption, where ohmic losses

occurs due to the heating of material by the induced current in the material. This is caused by attenuation of electromagnetic wave by its interaction with magnetic and electric dipoles present inside the material [20,44]. When an EM wave is incident on a material consisting of electric and magnetic dipoles; it will create an internal electric field and magnetic field which may lead/lag with respect to applied electromagnetic field [45]. Accordingly, magnetic loss and dielectric loss is created which is responsible for shielding effectiveness by absorption. Materials with high dielectric constant such as barium strontium titanate [46], barium titanate [47] etc. may offer electric dipoles and materials with high permeability such as ferrites [48] may provide high magnetic dipoles. Polymer nanocomposites with dielectric/magnetic fillers are also being used to attenuate EM radiation significantly by absorption.

Shielding due to absorption (SE_A) is given by [49]:

$$SE_A(dB) = 20\left(\frac{t}{\delta}\right) loge = 20t\sqrt{\frac{\mu_r \omega \sigma_{ac}}{2}}\, loge \quad \text{.....(1.11)}$$

where t is the thickness of material, δ is the skin depth, σ_{ac} is the ac conductivity of the shielding material, μ_r is the relative permeability and ω is the angular frequency. Shielding due to absorption is directly related to the thickness of material.

1.3.5. Shielding by multiple reflection

When an electromagnetic wave is incident on the shielding material, some fraction of amplitude of EM wave is reflected back and forth multiple times inside the material. These multiple reflection occurs in materials having large surface area. At high frequencies, the magnitude of EM wave decreases exponentially with the thickness of material. The thickness at which the amplitude of radiation reduces to the 1/e or 47% of the incident radiation is known as skin depth [50]. If the skin depth is greater than the thickness, multiple reflection occurs. The shielding due to multiple reflection is given as

$$SE_M = 20log_{10}(1 - e^{-\frac{2t}{\delta}}) \quad \text{.....(1.12)}$$

where t is the thickness and δ is the skin depth of the shielding material. The multiple reflection is neglected, when the material thickness become greater than the skin depth of the shielding material.

The different ways responsible for shielding mechanism are clarifying that shielding materials should have following properties:

1. Materials should be conducting in nature in order to attenuate the microwave by reflection.
2. Material must have high dielectric permittivity and permeability in order to attenuate the microwave by absorption.

1.4. MATERIAL EMPLOYED FOR EMI SHIELDING PURPOSES

There is a wide class of materials that are being employed for electromagnetic interference shielding, they have been subdivided into three categories *viz.* metals [8,13,16], ceramic and ceramic based composites [11,48,51] and polymer based composite materials [52–59]. They are briefly reviewed in the following subsections.

1.4.1. Metallic materials

Metals are preferable materials for EMI shielding applications due to their very good electrical and thermal conductivity [3,8,13,16,60–63] . Metals such as copper, aluminium, silver, gold exhibit reflection dominated shielding effectiveness due to their electrical conductivity, whereas metallic alloys such as supermeralloy, mumetal have absorption dominated shielding effectiveness due to their good magnetic permeability [64]. The metallic multilayer glass has been designed by electroless plating of Ni-Cu-P on Fe-Si-B glass. The maximum value of Shielding by absorption (SE_A) and reflection (SE_R) in X-band are reported as ~ 30 dB and 10 dB respectively [62]. Shielding due to absorption is dependent on the processing time of electroless plating but reflection remains nearly constant. Dielectric parameters shows the good impedance matching and, high conductivity and permeability have shown more interfacial interaction which enhanced the absorbance of microwave by multilayered metallic structures. The layer by layer dielectric and magnetic properties in the multilayered metallic structures are used to explain the electromagnetic shielding mechanism. The effect of addition of cerium (Ce) in magnesium alloy has been studied [63]. The maximum shielding effectiveness is found to be ~ 70 dB at 1.5 GHz frequency for only 1 wt% of Ce. The enhanced SE is attributed to increase in multiple reflection of electromagnetic radiation that occurs inside the material due to addition of Ce.

1.4.2. Ceramic based nanocomposites

Ceramic based composites also have been widely investigated in search of a material having very good shielding effectiveness [11,65–71].

Kumar *et al.* [65] designed a framework of carbon foam (CF) with multiwalled carbon nanotube (MWCNT) by two different techniques. The mechanical and electromagnetic shielding properties in X-band have been compared. It is found that MWCNT directly

grown on CF by chemical vapour deposition shows enhanced mechanical behaviour and maximum SE of 85 dB in X-band for 0.5 wt% of MWCNT loading in carbon foam. It concludes that the good mechanical strength play an important role in enhancing the shielding properties.

Table 1.1 Electromagnetic shielding parameters such as shielding by absorption (SE_A) and reflection (SE_R), shielding material's thickness and electrical conductivity (σ) of ceramic based nanocomposites in X-band frequency range.

S.No.	Material used	SE_A (dB)	SE_R (dB)	σ (S/cm)	Thickness (mm)	Reference
1.	Conducting ferrofluid nanocomposite	34	7	0.1	3	68
2.	Nickel@graphite nanoplate functional nanoparticles	43.8	13.2	30.8	0.3	72
3.	MoS_2-reduced graphene oxide/Cobalt ferrite nanocomposite	12.62	7.8	-	1.4	19
4.	Reduced graphene oxide aerogels decorated with Cobalt ferrite and zinc oxide	37.06	11.5	0.39	5	73
5.	Graphene nanoplatelet/Nickel/Wax nanocomposite	29	11	3.139	0.7	74
6.	3D faceted-Fe_3O_4-vertical carbon nanotubes(VCNT)@reduced graphene oxide hybrid	25	2	-	1	69
7.	Lanthanum strontium titanate $La_{0.7}Sr_{0.3}TiO_3$ nanomaterials	13	5	13	2	75
8.	Graphene oxide/ferrofluid/cement nanocomposite	40	9	10.4	2	76

Table 1.1 shows the electromagnetic shielding parameters such as shielding by absorption (SE_A) and reflection (SE_R), shielding material's thickness (t) and electrical conductivity (σ) of ceramic based nanocomposites in X-band frequency range reported in literature. There is one more interesting study, where mesocarbon microbeads (MCMB)with multiwalled nanotubes composite paper has been prepared [66] and achieved shielding effectiveness (SE) of ~ 51 dB in X-band of microwave. The thickness of this paper is 0.6 mm. The effect of incorporation of Fe_3O_4 nanoparticles in this composite paper, on the SE have also been studied. The SE is found to be enhanced to be ~ 80 dB at relatively reduced thickness of 0.5 mm. The enhanced shielding effectiveness in Fe_3O_4

nanoparticles incorporated composite paper is due to increase in the interfacial polarization and anisotropy energy. Electromagnetic shielding properties of the composite consisting of conducting ferrofluid have also been investigated in X-band [68]. Reduced graphene oxide (RGO) with Fe_3O_4 nanoparticles have been prepared by co-precipitation method. The values of shielding effectiveness due to absorption (SE_A) and reflection (SE_R) at 10.2 GHz are 34.23 dB and 7 dB respectively for 15 wt% loading of RGO. The obtained total shielding, shielding due to reflection and shielding due to absorption in X-band for 0 (CFF0), 1 (CFF1), 5(CFF5), 10 (CFF10) and 15% (CFF15) of RGO in ferrofluid is shown in Fig. 1.3. The respective high dielectric losses and high magnetic losses caused by RGO and Fe_3O_4 magnetic particles enhance the shielding effectiveness in X-band. Graphene based nanocomposite with dielectric ceramic nanoparticles $BaTiO_3$ was prepared by pressureless sintering method [11]. The graphene is homogeneously distributed over $BaTiO_3$. The increase in graphene nanosheets content in ceramics increases the electrical conductivity of nanocomposite due to conducting nature of graphene which increases the conducting network. The maximum value of total shielding effectiveness is reported as 41.7 dB in X-band for 4 wt% of graphene content at a thickness of 1.5 mm. The good dispersion

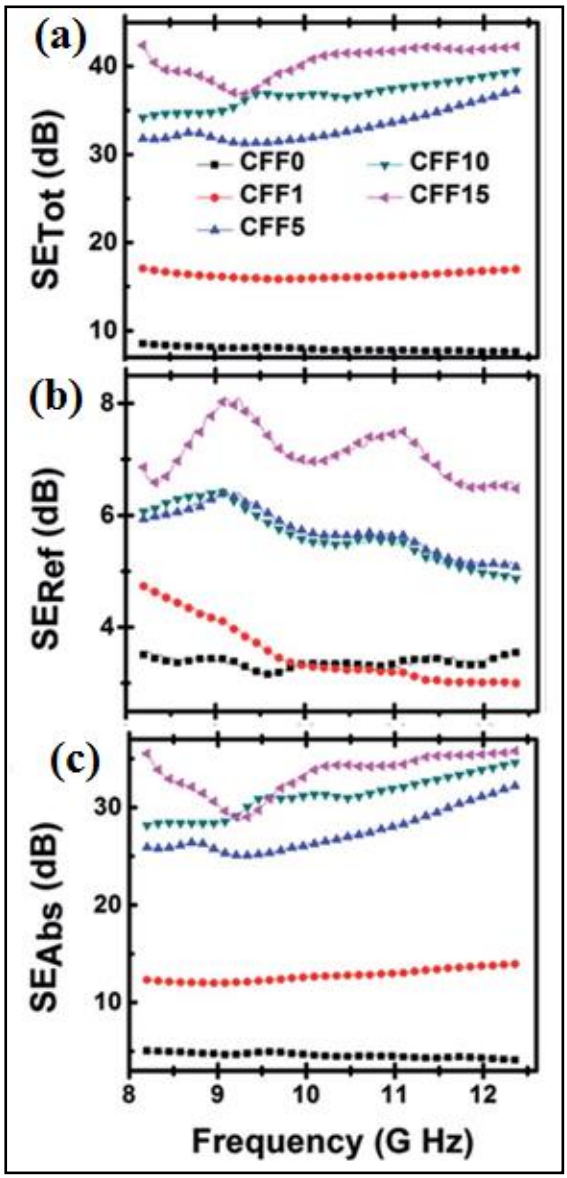

Fig. 1.3 Variation of obtained total shielding, shielding due to reflection and shielding due to absorption for CFF0, CFF5, CFF10 and CFF15 nanocomposites in X-band [67].

of graphene in nanocomposite and highly dielectric nature of $BaTiO_3$ might have played important role in enhancing the shielding effectiveness in X-band. Jin *et. al.* [67] synthesised the nanocomposite of graphene nanoplatelet/Fe_3O_4@$BaTiO_3$ with

multiwalled carbon nanotube (MWCNT) (GFBTM) in methyl vinyl silicon rubber by solvothermal technique. One dimensional MWCNTs act as a bridge for graphene to form conducting network structure inside the nanocomposite and increases the electrical conductivity and, also restrict the negative effect of $BaTiO_3$ and Fe_3O_4 on conductivity of nanocomposite. The nanocomposite shows the maximum SE due to absorption of ~ 25.4 dB along with very low reflection of ~ 6.3 dB in X-band. The synergistic effect of GFBTM filler in nanocomposite enhances the SE due to absorption. The nanocomposites containing facet-Fe_3O_4 with vertical carbon nanotube on RGO have emerged as a promising candidate for good absorption and low reflection in X-band. The nanocomposite has been synthesized simple microwave approach. The specific alignment of VCNT and eddy current loss due to f-Fe_3O_4 on RGO helped in more absorption with suppressed reflection [69].

The review of ceramic based composite materials are elucidating that interfacial polarization, formation of conducting network, high dielectric and magnetic losses leads to enhanced shielding effectiveness.

1.4.3. Polymer based composite materials

Polymer composites with conducting, dielectric and magnetic nanofillers are highly suitable materials for EMI shielding [12,77–84]. Polymer based nanocomposite materials have been largely used due to their advantages such as light weight, easy processibility, high mechanical strength and flexibility. The polymer based nanocomposites investigated for EMI shielding purposes are broadly divided into two categories. The first category is related with the nanocomposites consisting of non-conducting polymers such as polyvinyl alcohol [85], polyvinylidiene fluoride (PVDF) [79], polyurethane [81], poly(methyl methacrylate) (PMMA) [86] etc. with the conducting nanofillers such as carbon nanotube (CNT) [87], reduced graphene oxide (RGO) [88], graphene nanoplatelet [89] and metallic nanoparticles [90]. The second category includes conducting polymer such as polyaniline, polypyrrole etc. with conducting, dielectric and magnetic fillers [12,91–94]. The incorporation of nanostructure carbon materials such as CNT, RGO, graphene etc. in the dielectric polymer based composites have been found to improve electromagnetic interference shielding due to interfacial modification [19,78,95–98]. Subsequent subsection will briefly review the EMI shielding behaviour of polymer based composite materials based on non conducting and conducting polymers.

1.4.3.1. Non-conducting polymer nanocomposites

The nanocomposite containing polyurethane and silver nanowire (AgNW) has been fabricated by freeze-drying process. The electromagnetic shielding properties for different densities of composite in X-band have been studied [99]. The highest shielding effectiveness (SE) is found to be ~ 64 dB for the nanocomposite having density of 45 mg/cm^3. The synergistic effect of induced interfacial polarization and unidirectional alignment of AgNW particles in nanocomposite lead to enhancement of SE due to absorption. The values of SE due to absorption and SE due to reflection are ~ 53.4 dB and ~ 10.6 dB respectively. Polyvinyl alcohol/graphene nanoribbons composite film was developed to get the high performance shielding material. The highest SE in X-band was reported as high as 60 dB for 0.0075 wt% of graphene in nanocomposite and also, observed the increase in shielding with increase in thickness of composite. The thickness of composite plays a very important role in shielding [100]. Datt *et al.* [96] have explained the effect of ferromagnetic resonance of $NiCoFe_2O_4$ with carbon black and polyvinyl alcohol (PVA) on EMI shielding properties. The highest shielding effectiveness (SE) has been observed to be ~ 27 dB along with a low reflection of ~ 7 dB in X-band. The cationic disorder and particle size of nanocomposite film are attributed to increased interfacial polarization and electrical conductivity which enhances the SE of nanocomposite film [96]. The same kind of study has been carried out by other research groups [79,81,101–104]. The polypropylene and carbon nanotube composites has been found to have high shielding effectiveness in X-band [105]. Polypropylene/CNT nanocomposite shows increase in electrical conductivity with increase in filler content. The highest conductivity of 14.25 S/m for 5 wt% of CNTs has been reported. The percolation threshold is achieved at only 0.013 vol% of CNT. The maximum value of shielding due to absorption in polypropylene/CNT nanocomposites is ~ 48.3 dB at a thickness of 2.2 mm. The segregated structure of nanocomposite is the possible cause of enhancement of shielding due to absorption. Shen *et al.* [106] has come up with a multifunctional nanocomposite foam with low density for use as EMI shielding material for X-band applications. Polyetherimide (PEI)/graphene oxide@Fe_3O_4 (G@Fe_3O_4) nanocomposite foam has been prepared by phase separation method. PEI/G@Fe_3O_4 nanocomposites are paramagnetic in nature. The shielding effectiveness is increasing with increase in filler content and reached maximum value of 14-18 dB with least reflection of ~ 1 dB for 10 wt% of G@Fe_3O_4 in X-band. The thickness of nanocomposite is 2.5 mm. The enhanced absorption is attributed to interfacial polarization between the Fe_3O_4 nanoparticles and

graphene oxide and, high dielectric loss. Multiple reflection might be another cause of enhanced absorption which might have resulted due to reflection at the interfaces until absorbed by the shielding material. Table 1.2 is showing the electromagnetic shielding parameters such as shielding by absorption (SE_A) and reflection (SE_R), shielding material's thickness (t), skin depth (δ) and electrical conductivity (σ) of non-conducting polymer based nanocomposites reported in literature. These parameters are measured in X-band.

Table 1.2 Electromagnetic shielding parameters of non-conducting polymer based nanocomposites in X-band such as shielding by absorption (SE_A) and reflection (SE_R), shielding material's thickness (t), skin depth (δ) and electrical conductivity (σ).

S.No.	Material used	SE_A (dB)	SE_R (dB)	Thickness (mm)	δ (mm)	σ (S/cm)	Ref.
1.	Aluminium powder in polyurethane foam	26.7	17.9	-	0.81	-	81
2.	$NiCoFe_2O_4$-carbon black/poly(vinyl alcohol)	20	8	1.5	-	-	96
3.	Functionalised graphene/polyvinylidiene fluoride (PVDF)	20	-	-	-	10^{-6}	57
4.	Polyetherimide/carbon nanotube (CNT) foam	32.3	5.6	-	0.43	0.164	58
5.	Polycarbonate/poly (styrene-co-acrylonitrile)-multiwalled carbon nanotube	22	1.5	10	3.8	0.0834	55
6.	Poly(methyl methacrylate)/Graphene composite foam	18	1	4	-	0.0311	59
7.	Polystyrene/graphene/ Fe_3O_4	30	4	-	-	0.21	107
8.	Multiwalled carbon nanotube/Poly(L-lactide) nanocomposite	26	4	1.5	1.11	0.25	108

1.4.3.2. Conducting polymer nanocomposites

The nanocomposite consisting of conducting polymers with dielectric, magnetic and carbon based nanofillers are of special interest as they exhibit variety of ways to tune the absorption and reflection of electromagnetic wave.

Polyaniline/$Mn_{0.5}Zn_{0.5}Fe_2O_4$ nanocomposite has been developed as a good EM absorbing material [109]. The ferrite nanoparticles of size ~ 9-11 nm have high anisotropy and synthesized with polyaniline by *in-situ* chemical oxidative polymerization. The values of SE_A and SE_R have been reported as 31.2 dB and 4.8 dB respectively. The increased microwave absorption in X-band is assigned to highly anisotropic ferrite particles which increases the magnetic losses. Mann and Srivastava [98] have reported that Fe_3O_4@C@polyaniline core-shell structure exhibited the reflection loss of ~ 33 dB with ~ 47 dB of absorption loss in the frequency range of 2-8 GHz. The enhanced shielding effectiveness is due to the formation of dual interfaces and dielectric-magnetic integration. The formation of dual interfaces in the composite enhances the interfacial polarization and anisotropy which are the main cause of increase in reflection and absorption loss.

Table 1.3 Comparison of electromagnetic parameters such as shielding by absorption (SE_A) and reflection (SE_R), and shielding material's thickness of conducting polymer based nanocomposites reported in literature.

S.No.	Composite materials	Thickness (mm)	SE_A (dB)	SE_R (dB)	Ref.
1.	Poly(3,4-ethylenedioxythiophene) polystyrene/polyvinyl alcohol/ multiwalled carbon nanotube composite film	0.02	55	5.2	110
2.	Polythiophene/$Ni_{0.5}Zn_{0.5}Fe_{2-x}Ce_xO_4$ nanocomposite	-	29	5	53
3.	Natural fibre/polyaniline composite	-	26.66	6.14	54
4.	Cd^{2+} substituted Ni ferrite doped polyaniline composite	2.3	35	7.7	84
5.	Polypyrrole/barium strontium titanate/ reduced graphene oxide/Fe_3O_4 nanocomposite	2	42.75	5.83	46
6.	Fe_3O_4@carbon@polyaniline nanocomposite	2	47	15	98

Table 1.3 shows the comparison of SE_A, SE_R and shielding material thickness of conducting polymer based nanocomposites for X-band frequency range reported in literature. The conducting polymer with a conducting, dielectric and magnetic hybrid filler has been synthesized *via* chemical oxidative polymerization. Graphene oxide (GO), barium strontium titanate (BST) and Fe_3O_4 hybrid (BRF) has been prepared by co-precipitation method which was further used with pyrrole for polymerization [46]. BRF

hybrid showed the SE of ~ 14 dB in X-band and when incorporated with polypyrrole enhanced the SE to ~ 48.58 dB. The dielectric and magnetic fillers significantly contributed to shielding of EM wave. High conductivity of GO increased the polarization of the composite which helped in enhancing the absorbance. The interfacial polarization occurred between the polypyrrole and hybrid material enhanced the SE due to absorption. The SE_A and SE_R values are ~ 42.75 dB and 5.83 dB respectively.

The nanocomposite of polythiophene (PTH) with $Ni_{0.5}Zn_{0.5}Fe_{2-x}Ce_xO_4$ ferrite has been prepared by *in-situ* emulsion polymerization method [53]. The effect of cerium content on dielectric, magnetic, impedance and electromagnetic properties has been investigated in X-band frequency range of microwave. The maximum SE_A of ~ 29 dB along with SE_R ~ 5 dB is achieved for PTH/$Ni_{0.5}Zn_{0.5}Fe_{2-x}Ce_xO_4$ nanocomposite with x=0.04. The enhanced shielding absorption is due to high magnetic losses and the interfacial polarization induced in the nanocomposite. The nanocomposite film of cellulose, graphite and polypyrrole has been synthesized by *in-situ* chemical polymerization of pyrrole monomer on cellulose/graphite film [111]. The electrical conductivity and total shielding effectiveness in X-band have been reported to be ~ 0.55 S/cm and 30 dB in X-band. The increase in conductivity due to graphite increases the electrical conductivity and hence, improve the electromagnetic shielding properties.

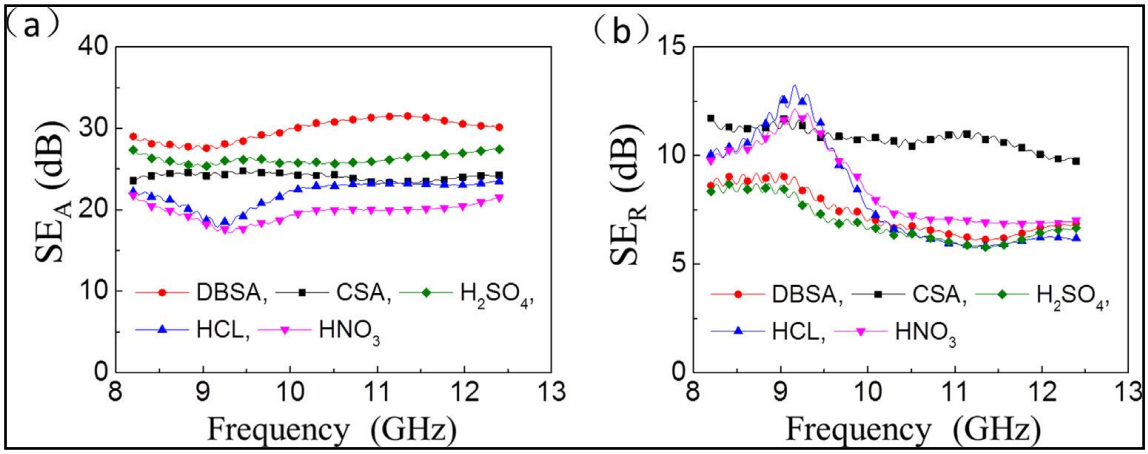

Fig. 1.4 Shielding due to absorption and reflection of redoped natural fiber/polyaniline nanocomposites with different dopants i.e. DBSA, CSA, H_2SO_4, HCl and HNO_3 [54].

The effect of secondary doping such as Dodecylbenzene sulfonic acid (DBSA), sulphuric acid (H_2SO_4), camphorsulfonic acid (CSA), hydrochloric acid (HCl), Nitric acid (HNO_3) on natural fiber/polyaniline nanocomposite has been studied [54]. The variation of shielding due to absorption and reflection of natural fiber/polyaniline nanocomposite redoped with

different solvents viz. DBSA, CSA, H_2SO_4, HCl, HNO_3 with frequency in X-band is shown in Fig. 1.4. The doping creates disorder in the motion of charge carriers by increasing the delocalization of electron concentration in the natural fiber/polyaniline nanocomposites. The disordered motion of charge carriers is responsible for increase in electrical conductivity. The maximum shielding due to absorption (SE_A) and reflection (SE_R) of ~ 30 dB and ~ 6.99 dB respectively have been achieved for DBSA doped nanocomposite in X-band frequency range. The high microwave absorption is assigned to the combined effect of good conductivity, capacitor like structure and interfacial polarization of nanocomposite.

1.5. AIM OF THESIS

As discussed in above sections, the interfacial modification, dielectric and magnetic losses are responsible for enhanced shielding effectiveness in conducting polymer based nanocomposites. The various methods have been adopted to tailor the interfaces in the different nanocomposites and its effect on the electromagnetic interference shielding is investigated. The shielding effectiveness mainly dominated by absorption of electromagnetic wave along with least possible reflection is required in many practical applications in microwave communication, defense etc. This kind of requirement is applicable in all bands of microwave i.e. L, C, K and Ku band. The development of shielding material with high shielding effectiveness due to absorption with negligible reflection in entire frequency band is still a challenging task. The review, rationale and requirement are encouraging to do investigation on conducting polymer based nanocomposites with increased absorption and least reflection.

Considering these aspects, the aim of proposed work is as follows:

(a) To synthesize the graphene nanosheets by low cost exfoliation of graphite.

(b) To synthesize the cobalt ferrite ($CoFe_2O_4$) nanoparticles by hydrothermal method.

(c) Investigation of Electromagnetic shielding behaviour of polypyrrole-graphene and polypyrrole-graphene-cobalt ferrite ($CoFe_2O_4$) nanocomposites.

REFERENCES

1 S. R. Dhakate, K. M. Subhedar and B. P. Singh, *RSC Adv.*, 2015, **5**, 43036–43057.

2 J. M. Thomassin, C. Jérôme, T. Pardoen, C. Bailly, I. Huynen and C. Detrembleur, *Mater. Sci. Eng. R Reports*, 2013, **74**, 211–232.

3 S. Geetha, K. K. S. Kumar, C. R. K. Rao, M. Vijayan and D. C. Trivedi, *J. Appl. Polym. Sci.*, 2009, **112**, 2073–2086.

4 O. Erogul, E. Oztas, I. Yildirim, T. Kir, E. Aydur, G. Komesli, H. C. Irkilata, M. K. Irmak and A. F. Peker, *Arch. Med. Res.*, 2006, **37**, 840–843.

5 S. B. Kondawar and P. R. Modak, *Theory of EMI shielding*, Elsevier Inc., 2020.

6 S. Gupta and N. H. Tai, *Carbon*, 2019, **152**, 159–187.

7 K. Singh, A. Ohlan, V. H. Pham, R. B. Balasubramaniyan, S. Varshney, J. Jang, S. H. Hur, W. M. Choi, M. Kumar, S. K. Dhawan, B. S. Kong and J. S. Chung, *Nanoscale*, 2013, **5**, 2411–2420.

8 D. D. L. Chung, *Carbon*, 2001, **39**, 279–285.

9 J. Ru, Y. Fan, W. Zhou, Z. Zhou, T. Wang, R. Liu, J. Yang, X. Lu, J. Wang, C. Ji, L. Wang and W. Jiang, *ACS Appl. Mater. Interfaces*, 2018, **10**, 39245–39256.

10 T. Tchouank Tekou Carol, J. Mohammed, D. Basandrai, S. K. Godara, G. R. Bhadu, S. Mishra, N. Aggarwal, S. B. Narang and A. K. Srivastava, *J. Magn. Magn. Mater.*, 2020, **501**, 1–12.

11 Q. Yuchang, W. Qinlong, L. Fa, Z. Wancheng and Z. Dongmei, *J. Mater. Chem. C*, 2016, **4**, 371–375.

12 J. Dalal, A. Gupta, S. Lather, K. Singh, S. K. Dhawan and A. Ohlan, *J. Alloys Compd.*, 2016, **682**, 52–60.

13 Y. Choi, Y. Yoo, J. Kim and S. Kim, *Surf. Coat. Technol.*, 2006, **201**, 3775–3782.

14 K. Naishadham, *IEEE Trans. Electromagn. Compat.*, 1992, **34**, 47–50.

15 C. R. Paul, *Introduction to Electromagnetic Compatibility: Second Edition*, 2006.

16 X. Luo and D. D. L. Chung, *Compos. Part B Eng.*, 1999, **30**, 227–231.

17 S. Sankaran, K. Deshmukh, M. B. Ahamed and S. K. Khadheer Pasha, *Compos. Part A Appl. Sci. Manuf.*, 2018, **114**, 49–71.

18 V. G. Harris, *IEEE Trans. Magn.*, 2012, **48**, 1075–1104.

19 J. Prasad, A. K. Singh, K. K. Haldar, M. Tomar, V. Gupta and K. Singh, *RSC Adv.*, 2019, **9**, 21881–21892.

20 S. Varshney, A. Ohlan, V. K. Jain, V. P. Dutta and S. K. Dhawan, *Mater. Chem. Phys.*, 2014, **143**, 806–813.

21 A. K. Singh, A. Kumar, K. K. Haldar, V. Gupta and K. Singh, *Nanotechnology*, 2018, **29**, 245203.

22 A. Kolanowska, D. Janas, A. P. Herman, R. G. Jędrysiak, T. Giżewski and S. Boncel, *Carbon*, 2018, **126**, 31–52.

23 Y. Bhattacharjee, D. Chatterjee and S. Bose, *ACS Appl. Mater. Interfaces*, 2018, **10**, 30762–30773.

24 M. S. Cao, X. X. Wang, W. Q. Cao and J. Yuan, *J. Mater. Chem. C*, 2015, **3**, 6589–6599.

25 X. H. Tang, J. Li, Y. Wang, Y. X. Weng and M. Wang, *Compos. Part B Eng.*, 2020, **196**, 108121.

26 G. George, S. M. Simon, V. Prakashan, M. Sajna, M. Faisal, R. Wilson, A. Chandran, P. R. Biju, C. Joseph and N. V. Unnikrishnan, *RSC Adv.*, 2018, **8**, 30412–30428.

27 D. Hu, X. Huang, S. Li and P. Jiang, *Compos. Sci. Technol.*, 2020, **188**, 107995.

28 H. Xie, Y. Zhou, Z. Ren, X. Wei, S. Tao and C. Yang, *J. Magn. Magn. Mater.*, 2020, **499**, 166244.

29 S. Kashi, R. K. Gupta, T. Baum, N. Kao and S. N. Bhattacharya, *Mater. Des.*, 2016, **95**, 119–126.

30 Y. Mamunya, L. Matzui, L. Vovchenko, O. Maruzhenko, V. Oliynyk, S. Pusz, B.

Kumanek and U. Szeluga, *Compos. Sci. Technol.*, 2019, **170**, 51–59.

31 A. R. Pai, T. Binumol, D. A. Gopakumar, D. Pasquini, B. Seantier, N. Kalarikkal and S. Thomas, *Carbohydr. Polym.*, 2020, **246**, 116663.

32 S. Gupta, C. Chang, C. H. Lai and N. H. Tai, *Compos. Part B Eng.*, 2019, **164**, 447–457.

33 T. K. Gupta, B. P. Singh, V. N. Singh, S. Teotia, A. P. Singh, I. Elizabeth, S. R. Dhakate, S. K. Dhawan and R. B. Mathur, *J. Mater. Chem. A*, 2014, **2**, 4256–4263.

34 D. Munalli, G. Dimitrakis, D. Chronopoulos, S. Greedy and A. Long, *Compos. Part B Eng.*, 2019, **173**, 106906.

35 D. Wanasinghe, F. Aslani, G. Ma and D. Habibi, *Constr. Build. Mater.*, 2020, **231**, 117116.

36 Y. P. Zhang, C. G. Zhou, W. J. Sun, T. Wang, L. C. Jia, D. X. Yan and Z. M. Li, *Compos. Sci. Technol.*, 2020, **197**, 108253.

37 J. Li, J. L. Chen, X. H. Tang, J. H. Cai, J. H. Liu and M. Wang, *J. Colloid Interface Sci.*, 2020, **565**, 536–545.

38 Y. F. Liu, L. M. Feng, Y. F. Chen, Y. D. Shi, X. D. Chen and M. Wang, *Compos. Sci. Technol.*, 2018, **159**, 152–161.

39 D. X. Yan, H. Pang, B. Li, R. Vajtai, L. Xu, P. G. Ren, J. H. Wang and Z. M. Li, *Adv. Funct. Mater.*, 2015, **25**, 559–566.

40 J. D. Jackson, *Classical Electrodynamics, John Wiley & Sons, New York, London*, 1962.

41 A. Ohlan, K. Singh, A. Chandra and S. K. Dhawan, *ACS Appl. Mater. Interfaces*, 2010, **2**, 927–933.

42 W. Y Chiang and Y. S Chiang, *J. Appl. Polym. Sci.*, 1992, **46**, 673–681.

43 A. R. Aparna, V. Brahmajirao and T. V Karthikeyan, *Int. J. Innov. Res. Sci. Eng. Technol.*, 2013, **2**, 7391–7401.

44 N. Gandhi, K. Singh, A. Ohlan, D. P. Singh and S. K. Dhawan, *Compos. Sci.*

Technol., 2011, **71**, 1754–1760.

45 J. S. Li, H. Huang, Y. J. Zhou, C. Y. Zhang and Z. T. Li, *J. Mater. Res.*, 2017, **32**, 1213–1230.

46 P. Sambyal, S. K. Dhawan, P. Gairola, S. S. Chauhan and S. P. Gairola, *Curr. Appl. Phys.*, 2018, **18**, 611–618.

47 K. Yang, X. Huang, F. Liu and P. Jiang, *Proc. IEEE Int. Conf. Solid Dielectr. ICSD*, 2013, 722–725.

48 E. H. Kim, H. S. Lee, B. K. Kwak and B. K. Kim, *J. Magn. Magn. Mater.*, 2005, **289**, 328–330.

49 V. Shukla, *Nanoscale Adv.*, 2019, **1**, 1640–1671.

50 N. F. Colaneri and L. W. Shacklette, *IEEE Trans. Instrum. Meas.*, 1992, **41**, 291–297.

51 J. Prasad, A. K. Singh, K. K. Haldar, V. Gupta and K. Singh, *J. Alloys Compd.*, 2019, **788**, 861–872.

52 J. Luo and D. Gao, *J. Magn. Magn. Mater.*, 2014, **368**, 82–86.

53 M. A. Dar, K. Majid, M. Hanief Najar, R. K. Kotnala, J. Shah, S. K. Dhawan and M. Farukh, *Phys. Chem. Chem. Phys.*, 2017, **19**, 10629–10643.

54 Y. Zhang, Z. Yang, T. Pan, H. Gao, H. Guan, J. Xu and Z. Zhang, *Compos. Part A Appl. Sci. Manuf.*, 2020, **137**, 105994.

55 S. P. Pawar, M. Gandi and S. Bose, *RSC Adv.*, 2016, **6**, 37633–37645.

56 J. Ju, T. Kuang, X. Ke, M. Zeng, Z. Chen, S. Zhang and X. Peng, *Compos. Sci. Technol.*, 2020, **193**, 108116.

57 V. Eswaraiah, V. Sankaranarayanan and S. Ramaprabhu, *Macromol. Mater. Eng.*, 2011, **296**, 894–898.

58 D. Feng, P. Liu and Q. Wang, *Compos. Part A Appl. Sci. Manuf.*, 2019, **124**, 105463.

59 H. Bin Zhang, Q. Yan, W. G. Zheng, Z. He and Z. Z. Yu, *ACS Appl. Mater. Interfaces*, 2011, **3**, 918–924.

60 S. Gao, X. Chen, F. Pan, K. Song, C. Zhao, L. Liu, X. Liu and D. Zhao, *Sci. Rep.*, 2018, **8**, 1–14.

61 J.-S. Roh, Y.-S. Chi, T. J. Kang and S. Nam, *Text. Res. J.*, 2008, **78**, 825–835.

62 J. Zhang, J. Li, G. Tan, R. Hu, J. Wang, C. Chang and X. Wang, *ACS Appl. Mater. Interfaces*, 2017, **9**, 42192–42199.

63 X. H. Chen, L. Z. Liu, J. Liu and F. S. Pan, *Acta Metall. Sin. (English Lett.)*, 2015, **28**, 492–498.

64 D. Chung, *Appl. Mater. Sci.*, 2001, **9**, 350–354.

65 R. Kumar, S. R. Dhakate, T. Gupta, P. Saini, B. P. Singh and R. B. Mathur, *J. Mater. Chem. A*, 2013, **1**, 5727–5735.

66 A. Chaudhary, R. Kumar, S. Teotia, S. K. Dhawan, S. R. Dhakate and S. Kumari, *J. Mater. Chem. C*, 2017, **5**, 322–332.

67 L. Jin, X. Zhao, J. Xu, Y. Luo, D. Chen and G. Chen, *RSC Adv.*, 2018, **8**, 2065–2071.

68 M. Mishra, A. P. Singh, B. P. Singh, V. N. Singh and S. K. Dhawan, *J. Mater. Chem. A*, 2014, **2**, 13159–13168.

69 R. Kumar, A. V. Alaferdov, R. K. Singh, A. K. Singh, J. Shah, R. K. Kotnala, K. Singh, Y. Suda and S. A. Moshkalev, *Compos. Part B Eng.*, 2019, **168**, 66–76.

70 Y. Liu, Y. Fu, L. Liu, W. Li, J. Guan and G. Tong, *ACS Appl. Mater. Interfaces*, 2018, **10**, 16511–16520.

71 A. G. D'Aloia, F. Marra, A. Tamburrano, G. De Bellis and M. S. Sarto, *Carbon*, 2014, **73**, 175–184.

72 X. Wang, B. Wen and X. Yang, *Compos. Part B Eng.*, 2019, **173**, 106904.

73 S. Gupta, S. K. Sharma, D. Pradhan and N. H. Tai, *Compos. Part A Appl. Sci. Manuf.*, 2019, **123**, 232–241.

74 H. J. Im, G. H. Jun, D. J. Lee, H. J. Ryu and S. H. Hong, *J. Mater. Chem. C*, 2017, **5**, 6471–6479.

75 H. A. Reshi, A. P. Singh, S. Pillai, R. S. Yadav, S. K. Dhawan and V. Shelke, *J. Mater. Chem. C*, 2015, **3**, 820–827.

76 A. P. Singh, M. Mishra, A. Chandra and S. K. Dhawan, *Nanotechnology*, 2011, **22**, 465701.

77 Y. Yuan, W. Yin, M. Yang, F. Xu, X. Zhao, J. Li, Q. Peng, X. He, S. Du and Y. Li, *Carbon*, 2018, **130**, 59–68.

78 G. Yin, Y. Wang, W. Wang and D. Yu, *Colloids Surfaces A Physicochem. Eng. Asp.*, 2020, **601**, 125047.

79 B. Zhao, S. Wang, C. Zhao, R. Li, S. M. Hamidinejad, Y. Kazemi and C. B. Park, *Carbon*, 2018, **127**, 469–478.

80 G. H. Lim, S. Woo, H. Lee, K. S. Moon, H. Sohn, S. E. Lee and B. Lim, *ACS Appl. Mater. Interfaces*, 2017, **9**, 40628–40637.

81 R. Kumar, H. Jain, S. Sriram, A. Chaudhary, A. Khare, V. A. N. Ch and D. P. Mondal, *Mater. Chem. Phys.*, 2020, **240**, 122274.

82 S. S. Chauhan, P. Verma, R. S. Malik and V. Choudhary, *J. Appl. Polym. Sci.*, 2018, **135**, 1–11.

83 L. Monnereau, L. Urbanczyk, J.-M. Thomassin, T. Pardoen, C. Bailly, I. Huynen, C. Jérôme and C. Detrembleur, *Polymer*, 2015, **59**, 117–123.

84 M. Saini, R. Shukla and A. Kumar, *J. Magn. Magn. Mater.*, 2019, **491**, 165549.

85 A. S. Roy, S. Gupta, S. Sindhu, A. Parveen and P. C. Ramamurthy, *Compos. Part B Eng.*, 2013, **47**, 314–319.

86 J. Chen, X. Liao, S. Li, W. Wang, F. Guo and G. Li, *Compos. Part A Appl. Sci. Manuf.*, 2020, **138**, 106059.

87 S. Maiti, R. Bera, S. K. Karan, S. Paria, A. De and B. B. Khatua, *Compos. Part B Eng.*, 2019, **167**, 377–386.

88 H. Zhu, Y. Yang, A. Sheng, H. Duan, G. Zhao and Y. Liu, *Appl. Surf. Sci.*, 2019, **469**, 1–9.

89 B. Zhao, C. Zhao, M. Hamidinejad, C. Wang, R. Li, S. Wang, K. Yasamin and C. B. Park, *J. Mater. Chem. C*, 2018, **6**, 10292–10300.

90 H. K. Chitte, N. V. Bhat, N. S. Karmakar, D. C. Kothari and G. N. Shinde, *World J. Nano Sci. Eng.*, 2012, **02**, 19–24.

91 M. Qiao, X. Lei, Y. Ma, L. Tian, X. He, K. Su and Q. Zhang, *Nano Res.*, 2018, **11**, 1500–1519.

92 C. Liu, Y. Xu, L. Wu, Z. Jiang, B. Shen and Z. Wang, *J. Mater. Chem. A*, 2015, **3**, 10566–10572.

93 A. Afzali, V. Mottaghitalab, S. S. Seyyed Afghahi, M. Jafarian and Y. Atassi, *J. Magn. Magn. Mater.*, 2017, **442**, 224–230.

94 S. Varshney, A. Ohlan, V. K. Jain, V. P. Dutta and S. K. Dhawan, *Ind. Eng. Chem. Res.*, 2014, **53**, 14282–14290.

95 A. P. Singh, M. Mishra, P. Sambyal, B. K. Gupta, B. P. Singh, A. Chandra and S. K. Dhawan, *J. Mater. Chem. A*, 2014, **2**, 3581–3593.

96 G. Datt, C. Kotabage and A. C. Abhyankar, *Phys. Chem. Chem. Phys.*, 2017, **19**, 20699–20712.

97 S. Anand, S. Pauline and C. J. Prabagar, *Polym. Test.*, 2020, **86**, 106504.

98 K. Manna and S. K. Srivastava, *ACS Sustain. Chem. Eng.*, 2017, **5**, 10710–10721.

99 Z. Zeng, M. Chen, Y. Pei, S. Ismail, S. Shahabadi, B. Che, P. Wang and X. Lu, *ACS Appl. Mater. Interfaces*, 2017, **9**, 32211–32219.

100 L. M. Malard, M. A. Pimenta, G. Dresselhaus and M. S. Dresselhaus, *Phys. Rep.*, 2009, **473**, 51–87.

101 E. Kar, N. Bose, B. Dutta, N. Mukherjee and S. Mukherjee, *Eur. Polym. J.*, 2017, **90**, 442–455.

102 R. Singh and S. G. Kulkarni, *Polym. Bull.*, 2014, **71**, 497–513.

103 S. P. Pawar, M. Gandi, C. Saraf and S. Bose, *J. Mater. Chem. C*, 2016, **4**, 4954–4966.

104 F. Shahzad, S. Yu, P. Kumar, J. W. Lee, Y. H. Kim, S. M. Hong and C. M. Koo, *Compos. Struct.*, 2015, **133**, 1267–1275.

105 H. Y. Wu, L. C. Jia, D. X. Yan, J. feng Gao, X. P. Zhang, P. G. Ren and Z. M. Li, *Compos. Sci. Technol.*, 2018, **156**, 87–94.

106 B. Shen, W. Zhai, M. Tao, J. Ling and W. Zheng, *ACS Appl. Mater. Interfaces*, 2013, **5**, 11383–11391.

107 Y. Chen, Y. Wang, H.-B. Zhang, X. Li, C.-X. Gui and Z.-Z. Yu, *Carbon*, 2015, **82**, 67–76.

108 K. Zhang, G. H. Li, L. M. Feng, N. Wang, J. Guo, K. Sun, K. X. Yu, J. B. Zeng, T. Li, Z. Guo and M. Wang, *J. Mater. Chem. C*, 2017, **5**, 9359–9369.

109 W. Wang, S. P. Gumfekar, Q. Jiao and B. Zhao, *J. Mater. Chem. C*, 2013, **1**, 2851–2859.

110 J. Dalal, S. Lather, A. Gupta, S. Dahiya, A. S. Maan, K. Singh, S. K. Dhawan and A. Ohlan, *Compos. Sci. Technol.*, 2018, **165**, 222–230.

111 J. Chen, J. Xu, K. Wang, X. Qian and R. Sun, *ACS Appl. Mater. Interfaces*, 2015, **7**, 15641–15648.

CHAPTER 2

EXPERIMENTAL TECHNIQUES

2.1. INTRODUCTION

This chapter describes the complete details of the experimental techniques employed for the synthesis of nanoparticles, their structural and morphological characterization, and electromagnetic shielding properties of the synthesized graphene based polypyrrole nanocomposites. The method adopted for the synthesis of different compounds such as graphene and cobalt ferrite are also discussed. Two-dimensional Graphene has been synthesized by using liquid phase exfoliation of graphite flakes. The soft nanoferrites have been synthesized *via* hydrothermal method. The *in-situ* chemical oxidative polymerization technique has been employed for synthesis of polypyrrole based nanocomposites. The X-ray diffraction and high resolution transmission electron microscopy (HRTEM) are used to study the crystal structure and morphology of nanoparticles. The structural and molecular bonding related studies of synthesized polypyrrole and nanocomposites have been carried out by Fourier transform infrared (FTIR) and Raman spectrum. Magnetic measurements have been done to determine the ferromagnetic nature of cobalt ferrite in nanocomposites. Current-voltage (I-V) measurements have been taken to determine the dc conductivity of the synthesized materials. Electromagnetic shielding measurements have been done to check the trends of shielding effectiveness due to absorption and reflection in X-band (8.2-12.4 GHz) of microwave region. The complex permittivity and permeability values have been checked to examine the electrical and magnetic behaviour of polymer nanocomposites. In the present chapter, the Cole-Cole plot has been used to find the information about the dielectric relaxation behaviour of polypyrrole nanocomposites. Skin depth of the nanocomposites decide the minimum thickness of the shielding material and ac conductivity shows the conducting behaviour of conjugated polymer in nanocomposite in X-band (8.2-12.4 GHz). The aforementioned experimental techniques are essential for carrying out the investigations on electromagnetic interference (EMI) shielding behaviour of graphene based polypyrrole nanocomposites.

2.2. SYNTHESIS OF MATERIAL

Nanosheets of graphene and cobalt ferrite nanoparticles have been synthesized by liquid phase exfoliation and hydrothermal method respectively. Graphene based polypyrrole nanocomposites have been prepared by *in-situ* chemical oxidative polymerization method. The subsequent sections describe the methods of synthesis of these materials.

2.2.1. Synthesis of graphene nanosheets

Graphene nanosheets can be synthesized by several method *viz.* vapour deposition method, chemical reduction of graphite oxide, wet ball milling method, liquid-phase exfoliation approach etc [1–4]. Among these methods, liquid-phase exfoliation of graphite in to graphene nanosheets are at edge due to ease of processibility, high yield etc. [5]. Therefore in the present work, the liquid-phase exfoliation method is used for the synthesis of graphene nanosheets. Following subsection discusses about this method.

2.2.1.1. Liquid phase exfoliation method

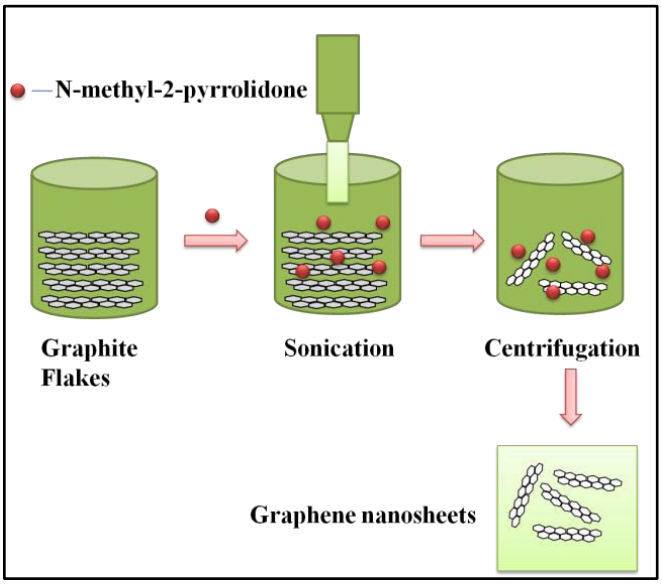

Fig. 2.1 The schematic representation of the exfoliation of graphite into graphene.

Liquid phase exfoliation method [6,7] is a novel method for the synthesis of graphene sheets. The graphite flakes are exfoliated into the graphene nanosheets. Solvent selection for the exfoliation of graphite into graphene is very important. Various solvents have been used for exfoliation of graphite such as N-methylpyrrolidiene (NMP), N, N-Dimethylformamide (DMF), naphthalene etc. [4,8]. Solvent with surface energy nearly comparable to vanderwall bonding energy of graphene sheets in graphite minimizes the effect of interfacial tension between the solvent and graphite flakes [9]. Such kind of interaction between solvent and graphite flakes leads to the formation of graphene. N-methylpyrrolidiene (NMP) is the best suitable polar solvent for the dispersion of graphite flakes. 40 mg/ml of natural flakes of graphite were dispersed in 100 ml of N-methyl-2-pyrrolidene (NMP) solution by using probe sonicator (Model: JYD-750L) for 2 h at different amplitudes of sonicating power *viz.* 60 %, 75% amplitude which give same number of graphene sheets (3-5 layered graphene nanosheets). The dispersed solution was left to stand overnight to allow the unstable aggregates to settle down before further use. The weakening of vanderwall forces between the different layers form the exfoliated graphite. The mixture was then centrifuged at 750 rpm for 90 min to remove the

unexfoliated material. The upper 70% superfluitant solution was removed, filtered and dried to get graphene nanosheets. Centrifugation is done to remove undispersed and large graphite flakes. Schematic representation of exfoliation of graphite into graphene is shown in Fig. 2.1.

In the present study, graphene has been synthesized by liquid phase exfoliation method, which has been discussed in Sec. 3.2.1.1 and Sec. 4.2.1.1 of Chapter 3 and Chapter 4 respectively.

2.2.2. Synthesis of cobalt-ferrite nanoparticles

Cobalt ferrite nanoparticles are soft ferrites which can be synthesized by many methods *viz.* sol-gel method, co-precipitation method, hydrothermal method etc [10–12]. Hydrothermal method is used in the present study due to many advantages over other conventional methods since it can control the phase, morphology and particle size by adjusting the amount of starting material, time and temperature. Therefore, hydrothermal method is used for the synthesis of cobalt ferrite nanoparticles. Subsequent subsection discusses the hydrothermal method.

2.2.2.1. Hydrothermal method

Hydrothermal synthesis of nanoparticles is an heterogeneous chemical reaction which is carried out under the condition of high temperature (above 100^{o}C) and high pressure (above 1 atm). Cobalt ferrite nanoparticles were synthesized by hydrothermal method using cobalt nitrate hexahydrate (Co $(NO_3)_2.6H_2O$) and iron nitrate nonahydrate (Fe $(NO_3)_3.9H_2O$) as the starting materials and sodium hydroxide (NaOH) as the precipitating agent. The stoichiometric amount of nitrates were dissolved in minimum amount of deionised water. Sodium hydroxide was added drop wise to the mixture of metal nitrates to increase the pH of solution to 12 under constant stirring. This solution was stirred for 3 h and, transferred to a 150 ml Teflon-lined stainless steel autoclave. The autoclave was sealed and heated at 180°C for 18 h duration. After the completion of hydrothermal reaction in autoclave, the autoclave was turned off and allowed to cool down to room temperature. The resultant product was filtered and washed with deionised water/ethanol for several times and finally dried at 70^{o}C in the vacuum oven to get $CoFe_2O_4$ nanopowder. The particle size and the morphology of final product can be controlled by varying pH, temperature and the concentration of initial reactants.

2.2.3. Synthesis of polymer based nanocomposites

Polymer based nanocomposites can be synthesized by several polymerization techniques such as *in-situ* or *ex-situ* polymerization, injection molding method, ball milling etc. [13–16]. However, the *ex-situ* polymerization method may lead to non homogeneous dispersion of fillers in polymeric matrix, On the other hand, homogeneous dispersion of fillers in the polymeric matrix is ensured by *in-situ* polymerization of monomer along with the fillers. Therefore, *in-situ* polymerization technique has been employed for synthesis of graphene based polypyrrole nanocomposites.

2.2.3.1. *In-situ* polymerization

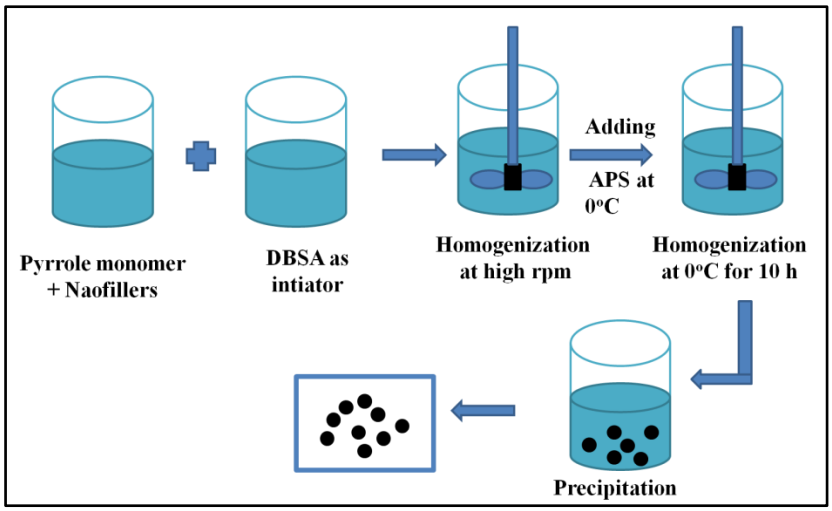

Fig. 2.2 The schematic representation of *in-situ* polymerization.

In-situ oxidative polymerization method [17] is the most widely used method for the synthesis of polymer nanocomposites. This method is suitable for synthesizing the nanocomposites with the thermally unstable and insoluble polymers, which cannot be synthesized by other methods. It is a one step method along with better compatibility of polymer with fillers in the polymer based nanocomposites. The schematic representation of *in-situ* polymerization to synthesize polymer nanocomposite is shown in Fig. 2.2. In this method, the nanoparticles are dispersed in the liquid monomer to form a homogenous mixture. An initiator is added to the mixture at an appropriate temperature for the polymerization reaction to start, which results in the formation of a fine, thermodynamically stable polymer nanocomposite. *In-situ* polymerization method leads to good dispersion of filler in matrix. The polymer nanocomposites synthesized in this way are best suited for investigating their physical properties.

The polypyrrole-graphene and polypyrrole-graphene-cobalt ferrite nanocomposites have been prepared by *in-situ* chemical oxidative polymerization technique which have been discussed in details in Sec. 3.2.1.2 and 4.2.1.3 of the chapter 3 and 4 respectively.

2.3. CHARACTERIZATION OF MATERIALS

Structural and surface morphological studies of synthesized materials have been carried out by X-ray diffraction, high resolution transmission electron microscopy whereas Raman and Fourier transform spectroscopy studies are employed to understand the chemical and molecular bonding. The magnetic behaviour of nanoparticles and nanocomposites have been studied by vibrating sample magnetometer (VSM). The Electrical conductivity and electromagnetic interference (EMI) shielding has been studied by using source measuring unit and vector network analyzer respectively. The details of the aforementioned studies have been given in subsequent subsections.

2.3.1. Structural and morphological studies

X-ray diffraction and high resolution transmission electron microscope have been used to find the crystalline structure, particle size and morphology of the synthesized samples. Raman and Fourier transform spectroscopy have been carried out to analysis of chemical and molecular structure of the samples.

2.3.1.1. X-ray diffraction

X-ray diffraction (XRD) [18,19] technique is used to detect the crystallization and spacing of the crystal lattice in the sample. X-rays are produced by heating a filament in a cathode ray tube with the filament current in the range of 10 mA, to produce electrons. The electrons with kinetic energy in range of KeV are accelerated towards specimen by applying a voltage. Copper is best suitable filament material with wavelength Cu Kα = $1.5418\,\dot{A}$. In the present work, the XRD pattern is recorded by using D8 advance instrument (Bruker AXS) using Cu Kα radiation. Pyrolitic graphite monocromator is used for producing monochromatic Cu Kα wavelength of radiation, which is directed toward the sample and after falling on the sample they are reflected back. The reflected signal is recorded by detector.

When the incoming X-rays interact with the different lattice planes of sample, the reflected ray from the different lattice planes obeys Bragg's law which is given as:

$$n\lambda = 2dsin\theta \quad \text{..... (2.1)}$$

where 'd' is the spacing between the different lattice planes, n is the order of diffraction planes and 'λ' is the wavelength of incident X-rays and 2θ is the angle between the incident beam and the reflected X-ray beam from the lattice planes of the sample. X-ray tube and detector move simultaneously, at an angle of theta (θ). Hence, detector makes angle 2 theta (2θ) with the incident X-ray beam.

In this work, X-ray diffraction pattern has been used to investigate the crystallite size of cobalt ferrite nanoparticles and, to determine the phases of graphene and cobalt ferrite nanoparticles in polypyrrole based nanocomposites.

2.3.1.2. Fourier transform infrared spectroscopy

Fourier transform infrared (FTIR) spectroscopy [20] is used to get information about the molecular structure and the vibration or rotation of chemical bonds of the sample. FTIR method is based either on the absorption mode or transmission mode. In the present work, transmission mode of FTIR spectroscopy (Model: Nicolet, iS10) has been employed. The infrared radiation from the source is directed to the interferometer which split the beam of radiation into two parts. Transmitted light falls on fixed mirror which travel different distance from the reflected ray which falls on moving mirror. The difference in distance travelled is known as optical path difference. The reflected light coming from the both mirrors at beam splitter falls on the sample. these two rays reflected from sample interfere and, produce FTIR spectra, which is recorded by the detector. FTIR spectra is the fingerprint of absorption of molecular bond for which the frequency of vibration correspond to the vibration of bonds between atoms. FTIR spectrum has been used to identify the molecular bonding of nanoparticles and graphene based polypyrrole nanocomposites.

2.3.1.3. High resolution transmission electron microscopy

High resolution transmission electron microscopy (HRTEM) is one of the most important technique to find the surface morphology and microstructural studies in material science. HRTEM is based on the principle of operating an electron beam to transmit through the sample to produce a highly magnified image of the specimen. The high voltage of order of kV is applied to cathode. It generates a beam of electrons which passes through the electromagnetic coils (lens). The condenser lens system contains three stages, one is condenser lens which helps in the formation of beam, another is the objective lens which is used to focus the electron beam on the specimen and the projector lens helps the

electron beam to expand on the phosphor screen and gives the final magnified visible image. The electron beam accelerating through the condenser lens should have a sufficient energy of about 100 to 400 KeV in electron gun to produce an electron beam with a beam diameter of the order of tens of nanometres.

In the present work, HRTEM (Model: Tecnai G2, F30) has been used to get the information related to morphology and size of the cobalt ferrite nanoparticles, graphene and graphene based polypyrrole nanocomposites.

2.3.1.4. Raman spectroscopy

Raman spectroscopy is a vibrational spectroscopy based on inelastic scattering in which the incident radiation transfer energy to the molecular vibrations. It gives the molecular fingerprint of the molecule. When the radiation interact with the molecule, then there is a change in molecular polarizabilty i.e. the distortion of electron cloud. The molecules are excited to higher energy level. The difference in energy of the incident photon to the scattering photon is known as Raman shift.

Raman system comprises of a i) source usually a visible light laser; ii) sample illumination and optical lens for scattering; and iii) a monocromator; and a signal processing unit consisting of detector and the computer operating system. A solid state laser is generally used as source with different wavelengths of 532 nm, 785 nm, 830 nm and 1064 nm. The laser light is focussed on the sample with the help of a set of lens and the scattered light is directed towards monocromator with another set of lens and collected by detector. The monochromator rejects Rayleigh scattering and other light to reach to detector.

In the present work Raman spectrometer (Model: Renishaw nVia Raman spectrometer) is employed to confirm the formation of graphene. A laser with the excitation wavelength of 532 nm is used for recording Raman spectra.

2.3.2. Magnetic studies

Vibrating sample magnetometer (VSM) is used for magnetic studies of cobalt ferrite nanoparticles and graphene based polypyrrole nanocomposites consisting of cobalt ferrite.

2.3.2.1. Vibrating sample magnetometer

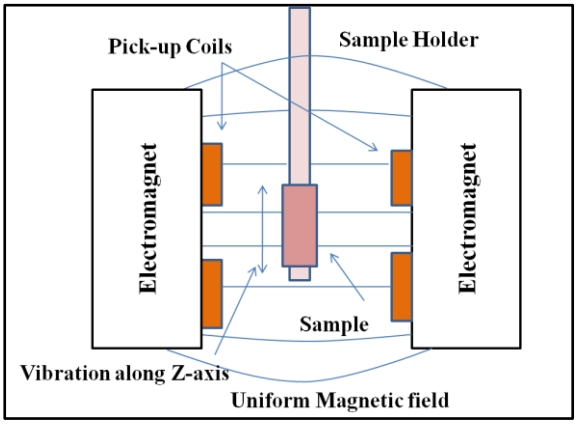

Fig. 2.3 The schematic representation of vibrating sample magnetometer.

Vibrating sample magnetometer (VSM) [21] is the used to measure the magnetic moment with respect to magnetic field of the magnetic materials. The sample is placed in the constant magnetic field where the sample is moving up and down between the pickup coils. The constant magnetic field will induce the magnetic domains to align in a particular direction and the magnetic dipoles of sample will create the magnetic field near the sample which is recorded by pickup coils in the form of induced current. The induced current is proportional to the magnetization of sample. The output from the software shows the hysteresis curve of magnetic field intensity and magnetization which gives information about the coercivity, remanence and saturation magnetization of the magnetic material. The schematic representation of vibrating sample magnetometer is shown in Fig. 2.3.

In the present work, VSM (Model: Lakeshore 7404 series) has been used to get information about coercivity, remanence and saturation magnetization of the cobalt ferrite nanoparticles and, graphene based polypyrrole nanocomposite consisting of cobalt ferrite.

2.3.3. Electrical and electromagnetic studies

The electrical and electromagnetic studies include the study of conducting behaviour and, electromagnetic interference (EMI) shielding properties of synthesized material *viz.* graphene based polypyrrole nanocomposites.

2.3.3.1. Electrical conductivity

Electrical conductivity or dc conductivity is the property of a material to conduct the electric current. The dc conductivity is calculated by the current-voltage measurement done on the source measuring unit (Model: Keithley 2410) at room temperature. The current-voltage measurement has been done by two-probe method in which resistivity of a sample is calculated. A small amount of voltage (V) is applied to the specimen, the

current (I) starts flowing through the two contacts which is measured, and gives the resistivity (ρ) values. According to ohm's law,

$$\rho = \frac{VA}{IL} \quad \text{and} \quad \sigma = \frac{1}{\rho} \qquad \text{.....(2.2)}$$

where 'A' is the cross-sectional area and 'L' is the length of the specimen. The conductivity (σ) is the reciprocal of resistivity.

2.3.3.2. Electromagnetic shielding properties

Electromagnetic interference (EMI) shielding properties of graphene based polypyrrole nanocomposite is measured by using vector network analyzer. The details of vector network analyzer and the methods adopted for studying the EMI shielding properties are discussed in the subsequent subsections.

2.3.3.2.1. Vector network analyzer

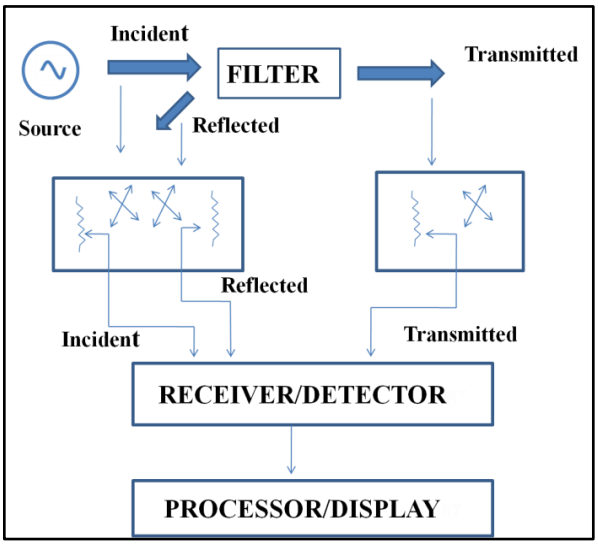

Fig. 2.4 Block diagram of vector network analyzer.

The shielding effectiveness can be measured by using network analyzers. The network analyzer is a instrument used to measure the impedance. At low frequencies, the impedance can be measured by measuring the current and voltage by using sine wave, voltmeter, ammeter and a calculating device. There are generally two types of network analyzers, one is scalar network analyzer (SNA) which gives the amplitude of EM wave and the other is vector network analyzer (VNA), which gives the amplitude as well as the phases of EM wave. SNA capture the signal and convert it into DC signal or low ac signal to measure the power of the signal. SNA is scalar in nature, so it does not give the accurate results. SNA cannot measure the complex permittivity and permeability whereas the VNA can measure the complex values easily. Vector network analyzer is a two port system [22]. Fig. 2.4 shows the block diagram of vector network analyzer. The main principle of using VNA is to measure amplitude and phase of incident, reflected and transmitted radiation of the device under test. When a two port network is under test, then

the measurements are done in various conditions and computed in a set of parameters which describe the electrical behaviour of network. At low frequencies, the overall current and voltage are measured in terms of H, Y and Z-parameters with open-circuit and short circuit conditions. At high frequency i.e. microwave frequency, the measurement of current and voltage are difficult. Therefore, S-parameters are used to measure the current and voltage by using a complex design with use of incident and reflected wave. S-parameters are easy to measure and do not require open or close circuit. The others parameters i.e. H, Y and Z-parameters can be easily derived from the S-parameters. S-parameters can easily do the loss, gain and reflection coefficient measurements. The details of S-parameters are as follows.

2.3.3.2.2. S-parameters

When an EM wave passes through the two-port network, the wave is forwarded by both ports toward the source and the relationship between the incident, reflected and transmitted wave is given by the scattering parameters (S_{11}, S_{12}, S_{21}, S_{22}). The schematic of the two port network is shown in Fig. 2.5. Scattering parameters (S-parameters) describe the magnitude and phase relationship between the incident wave and the reflected wave.

$$S_{11} = \frac{V_{1o}}{V_{1i}} \text{(when } V_{2i}=0 \text{ i.e. the impedance match at port 1)} \quad \text{.....(2.3)}$$

$$S_{22} = \frac{V_{2o}}{V_{2i}} \text{ (when } V_{1i}=0 \text{ i.e. the impedance match at port 2)} \quad \text{..... (2.4)}$$

$$S_{21} = \frac{V_{2o}}{V_{1i}} \quad \text{..... (2.5)}$$

$$S_{12} = \frac{V_{1o}}{V_{2i}} \quad \text{.....(2.6)}$$

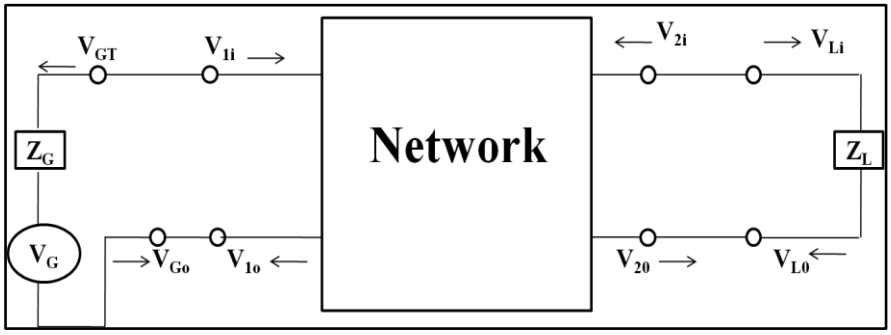

Fig. 2.5 The schematic representation of the two port network.

The reflection measurements are expressed by S_{11}, S_{22} parameters and the transmitted measurements are expressed by S_{12} and S_{21} parameters. The reflection and absorption coefficients are calculated from measured S-parameters as:

$$R = |S_{11}|^2 = |S_{22}|^2 \quad \text{.....(2.7)}$$

$$T = |S_{12}|^2 = |S_{21}|^2 \quad \text{.....(2.8)}$$

$$SE_R = -10log_{10}(1 - R) \quad \text{.....(2.9)}$$

$$SE_A = 10\log\left(1 - A_{eff}\right) = -10log(T/1 - R) \quad \text{.....(2.10)}$$

In the present study, S-parameters for graphene based polypyrrole nanocomposites have been carried out by Agilent N5230C vector network analyzer (VNA) in X-band (8.2-12.4 GHz). The nanocomposites are pressed in the form of rectangular pallets of thickness 2 mm and inserted in the sample holder connected between the waveguide of network analyzer. Nicolson-Ross-Weir method is used to calculate the complex quantities (electrical permittivity and magnetic permeability), which are discussed in the following section.

2.3.3.2.3. Nicolson-Ross-Weir method

Nicolson and Ross in 1970 and Weir in 1974 combined their theories to calculate the electrical permittivity and magnetic permeability of material by reflection and transmission coefficients of EM wave and named it as Nicholson-Ross-Weir algorithm (NRW) [23]. NRW method is one of the simplest method to find the complex permittivity and the permeability from the measured scattering parameters by using some simple calculations. The complex permittivity and permeability are:

$$\varepsilon = \varepsilon_r\varepsilon_o = (\varepsilon' + j\varepsilon'')\varepsilon_o \quad \text{.....(2.11)}$$

$$\mu = \mu_r\mu_o = (\mu' + j\mu'')\mu_o \quad \text{.....(2.12)}$$

The Reflection coefficient is given as:

$$\Gamma = X \pm \sqrt{X^2 - 1} \quad \text{.....(2.13)}$$

where $X = \frac{S_{11}^2 - S_{21}^2 + 1}{2S_{11}}$ and the transmission coefficient is given as:

$$T = \frac{S_{11} - S_{21} + \Gamma}{1 - (S_{11} + S_{21})\Gamma} \quad \text{.....(2.14)}$$

The dielectric permittivity and magnetic permeability of sample with thickness L are calculated from reflection and transmission coefficient using following equations:

$$\mu_r = \frac{1+\Gamma}{\Lambda(1-\Gamma)\sqrt{{}^{1}/_{\lambda_0^2} - {}^{1}/_{\lambda_c^2}}} \quad \text{.....(2.15)}$$

$$\varepsilon_r = \frac{\lambda_0^2}{\mu_r}\left[\frac{1}{\lambda_c^2} - \left(\frac{1}{2\pi L} ln\left(\frac{1}{T}\right)\right)^2\right] \quad \text{.....(2.16)}$$

where $\frac{1}{\Lambda^2} = \left(\frac{1}{2\pi L} ln\left(\frac{1}{T}\right)\right)^2$

λ_0 is the wave's wavelength and the λ_c is the waveguide cut-off frequency.

Skin depth is the important parameter related to the EMI shielding. It decides the minimum thickness of shielding material used in the application for the attenuation of the microwave in X-band. Skin depth depends on the magnetic permeability and electrical permittivity and is expressed as follows:

$$\delta = \sqrt{\frac{2}{\sigma\omega\mu'}} \quad \text{.....(2.17)}$$

where σ is the ac conductivity, μ' is the imaginary permeability. Furthermore, the ac conductivity can be defined as:

$$\sigma_{ac} = \omega\varepsilon_0\varepsilon'' \quad \text{.....(2.18)}$$

where ε'' is the imaginary permittivity and ε_0 is the permittivity in vacuum. Attenuation constant of microwave is the property of effectiveness of material to attenuate the microwave exposed on it.. It causes the decrease in signal of incident wave while propagating through the shielding material and is expressed as:

$$\alpha = \frac{\sqrt{2}\pi f}{c}\sqrt{(\mu''\varepsilon'' - \mu'\varepsilon') + \sqrt{(\mu''\varepsilon'' - \mu'\varepsilon')^2 + (\mu'\varepsilon'' + \varepsilon'\mu'')^2}} \quad \text{.....(2.19)}$$

where f is the frequency of microwave.

In the present study, all shielding parameters *viz.* skin depth, ac conductivity, attenuation constant of the graphene based polypyrrole nanocomposites are calculated from dielectric

permittivity and magnetic permeability which are measured from S-parameters by using Nicolson Ross-Weir method.

REFERENCES

1 H. Huang, W. Chen, S. Chen and A. T. S. Wee, *ACS Nano*, 2008, **2**, 2513–2518.

2 B. Hu, H. Ago, Y. Ito, K. Kawahara, M. Tsuji, E. Magome, K. Sumitani, N. Mizuta, K. I. Ikeda and S. Mizuno, *Carbon*, 2012, **50**, 57–65.

3 L. Zhu, X. Zhao, Y. Li, X. Yu, C. Li and Q. Zhang, *Mater. Chem. Phys.*, 2013, **137**, 984–990.

4 W. Zhao, M. Fang, F. Wu, H. Wu, L. Wang and G. Chen, *J. Mater. Chem.*, 2010, **20**, 5817–5819.

5 Y. Hernandez, V. Nicolosi, M. Lotya, F. M. Blighe, Z. Sun, S. De, I. T. McGovern, B. Holland, M. Byrne, Y. K. Gun'ko, J. J. Boland, P. Niraj, G. Duesberg, S. Krishnamurthy, R. Goodhue, J. Hutchison, V. Scardaci, A. C. Ferrari and J. N. Coleman, *Nat. Nanotechnol.*, 2008, **3**, 563–568.

6 W. Du, X. Jiang and L. Zhu, *J. Mater. Chem. A*, 2013, **1**, 10592–10606.

7 M. Lotya, Y. Hernandez, P. J. King, R. J. Smith, V. Nicolosi, L. S. Karlsson, F. M. Blighe, S. De, W. Zhiming, I. T. McGovern, G. S. Duesberg and J. N. Coleman, *J. Am. Chem. Soc.*, 2009, **131**, 3611–3620.

8 C. Liu, G. Hu and H. Gao, *J. Supercrit. Fluids*, 2012, **63**, 99–104.

9 M. Monajjemi, *J. Mol. Liq.*, 2017, **230**, 461–472.

10 G. Allaedini, S. M. Tasirin and P. Aminayi, *Int. Nano Lett.*, 2015, **5**, 183–186.

11 P. P. Hankare, K. R. Sanadi, K. M. Garadkar, D. R. Patil and I. S. Mulla, *J. Alloys Compd.*, 2013, **553**, 383–388.

12 Y. Zhang, Z. Yang, D. Yin, Y. Liu, C. Fei, R. Xiong, J. Shi and G. Yan, *J. Magn. Magn. Mater.*, 2010, **322**, 3470–3475.

13 T. K. Gupta, B. P. Singh, R. B. Mathur and S. R. Dhakate, *Nanoscale*, 2014, **6**, 842–851.

14 Y. Huang, Z. Liu, R. Chen, S. Zheng, C. Feng, L. Chen, W. Yang and M. Yang, *Compos. Sci. Technol.*, 2019, **171**, 127–134.

15 Y. P. Zhang, C. G. Zhou, W. J. Sun, T. Wang, L. C. Jia, D. X. Yan and Z. M. Li, *Compos. Sci. Technol.*, 2020, **197**, 108253.

16 Y. Du, W. Liu, R. Qiang, Y. Wang, X. Han, J. Ma and P. Xu, *ACS Appl. Mater. Interfaces*, 2014, **6**, 12997–13006.

17 V. Mittal, *In-Situ Synth. Polym. Nanocomposites*, 2011, 1–25.

18 B.D.Cullity, *Element of X-Ray Diffraction*, Addison-wesley 1956.

19 Y. Waseda, E. Matsubara and K. Shinoda, eds. Y. Waseda, E. Matsubara and K. Shinoda, Springer Berlin Heidelberg, Berlin, Heidelberg, 2011, pp. 1–20.

20 *Fourier Transform Infrared Spectrom.*, 2007, 75–95.

21 S. Preparation, C. Setup, I. Setup, C. Samples and I. Shutdown, 1994, **294**, 1–5.

22 N. Shoaib, ed. N. Shoaib, Springer International Publishing, Cham, 2017, pp. 37–46.

23 M. Farukh, A. P. Singh and S. K. Dhawan, *Compos. Sci. Technol.*, 2015, **114**, 94–102.

CHAPTER 3

STUDIES ON ELECTROMAGNETIC SHIELDING BEHAVIOUR OF POLYPYRROLE-GRAPHENE NANOCOMPOSITES

3.1. INTRODUCTION

Materials exhibiting very good electromagnetic interference (EMI) shielding have gained considerable interest of scientific community due to their technological applications such as microwave communication, defence, and for checking electromagnetic pollution etc. [1–3]. EMI shielding is achieved by reflection, absorption and multiple reflection of EM wave from the shielding material [4]. Large number of materials have been investigated by different research groups for EMI shielding applications [5–7]. Carbon nanofillers based polymer nanocomposite [8–12] have been observed as promising material by virtue of their good mechanical strength, electrical and thermal behaviour, light weight, low cost and ease of processing etc. But, for most of the applications such as microwave communication, stealth technology in defence and checking of EM wave pollution, a very good microwave absorption along with suppressed reflection is required [13–15]. Carbon nanofillers based polymer nanocomposites have been widely investigated in order to have very good EMI shielding behaviour [16–20]. Observation on polypropylene/*in-situ* reduced graphene oxide (PP/RGO) nanocomposite has found to have shielding effectiveness by absorption (SE_A) and reflection (SE_R) of ~ 42 dB and ~ 8 dB respectively for 20 wt% loading of RGO [17]. The enhanced shielding effectiveness is attributed to increased conductivity and formation of microcapacitors leading towards attenuation of microwave. Ma *et al.* [18] have investigated the shielding effectiveness of polymer/carbon light weight nanocomposite. This composite exhibited SE_A and SE_R of ~ 19 dB and ~ 9 dB respectively for material of thickness 2 mm. The enhanced shielding effectiveness is ascribed to attenuation of microwave reflection caused by porous microstructure. The incorporation of 70 wt% of polyvinyl chloride beads in polyvinyl chloride/multiwalled carbon nanotube (PVC/MWCNT) nanocomposite exhibits the SE_A ~ 23 dB and SE_R ~ 4 dB in X-band [19]. The non conducting beads form the microcapacitors and the polarization centre which increases the imaginary permittivity leading to higher absorption of EM radiation. The thermoplastic polyurethane with reduced graphene oxide (RGO) composite form a segregated structure with conducting network which is attributed to enhanced shielding effectiveness of shielding material. The total shielding effectiveness (SE_T) for 3.17 vol% loading of RGO is found to be ~ 21.8 dB [20]. The polyetherimide/carbon nanotube composite foam has been developed by sinter molding foam method and the maximum SE_A of ~ 32.3 dB, SE_R of ~ 5.6 dB for 2.94 vol% loading of carbon nanotube have been reported [21]. The enhanced SE is caused due to improved conductivity of

nanocomposite with increase in carbon nanotube content in composite. Role of interfaces and interfacial polarization have been found to be important cause for improving shielding effectiveness of carbon nanofillers based polymer composites.

This chapter presents, the synthesis of graphene encapsulated polypyrrole-graphene (PG) nanocomposite by *in-situ* chemical oxidative polymerization method. Detailed structural investigation and analysis of microwave dielectric and shielding effectiveness behaviour of polypyrrole-graphene nanocomposites are carried out in X-band (8.2-12.4 GHz) of microwave region.

3.2. EXPERIMENTAL

The experimental section is broadly divided in three parts *viz.* synthesis of material, structural and morphological studies, electrical and electromagnetic shielding studies. The discussion related with them is presented in subsequent sections.

3.2.1. Synthesis of materials

Graphene has been synthesized by liquid phase exfoliation method (Sec. 2.2.1.1). The polypyrrole-graphene nanocomposites have been synthesized by *in-situ* chemical oxidative polymerization method (Sec. 2.2.3.1). These methods are briefly described in subsequent subsections.

3.2.1.1. Synthesis of graphene

The synthesis of graphene has been carried out by liquid phase exfoliation method, where the graphite flakes are dissolved in N-methyl-2-pyrrolidene (NMP) solution by using tip sonicator at an amplitude of 75%. The resulting solution consisting of exfoliated graphite flakes, which has been left for 24 hrs to settle down the unexfoliated graphite flakes. Settled solution is again subjected to sonication for 2 h that converts the exfoliated graphite flakes in to graphene. After sonication it is centrifuged at 750 rpm for 90 min to remove the unexfoliated graphite. The upper 70% superfluitant solution was removed and filtered. The filtered materials is dried in vacuum oven at 60^{o} to get the graphene nanosheets.

3.2.1.2. Synthesis of polypyrrole-graphene nanocomposite

Polypyrrole-graphene (PG) nanocomposite has been synthesized by *in-situ* chemical

oxidative polymerization [9]. Pyrrole monomer and graphene sheets were taken in the ratio 1:0, 1:0.1 and 1:0.2 by weight for polypyrrole-graphene nanocomposites named as PG0, PG1 and PG2 respectively. The graphene nanosheets were homogenized in DBSA solution at 6000 rpm to get the uniform dispersion. DBSA has been used as dopant in order to increase the conductivity [22]. Pyrrole monomer was added dropwise to this homogenized mixture during continuous stirring for 1 h. The resulting solution was cooled to 5^0 C in the ice bath. After that 0.1M $FeCl_3$ was added drop wise to the precooled solution which was further subjected to continuous stirring for 12 h. This process leads to formation of dark brown precipitates; which were washed thoroughly with ethanol and distilled water to remove all impurities. Finally, the precipitates were dried in oven at 60^0C for 24 h. The schematic representation of synthesis of polypyrrole-graphene nanocomposites is shown in Fig. 3.1.

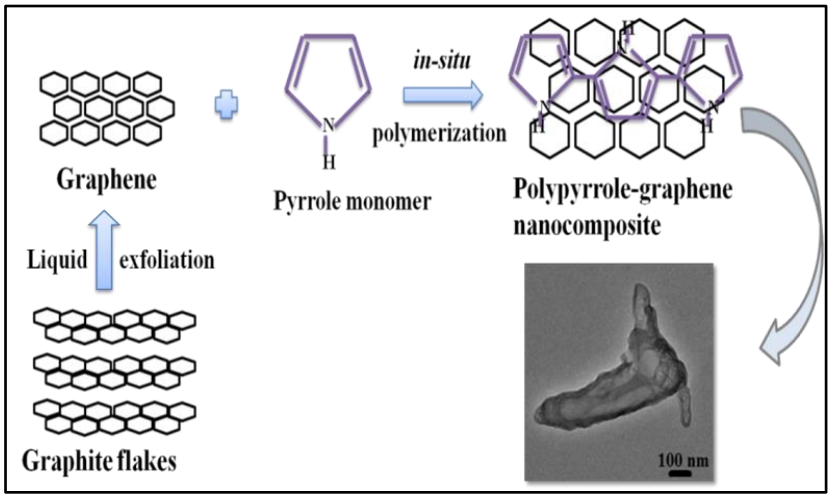

Fig. 3.1 The schematic representation of synthesis of Polypyrrole-graphene nanocomposites.

3.2.2. Structural and morphological studies

The phase identification and morphological studies of synthesized materials are carried out by the X-ray diffraction (XRD) and high resolution transmission electron microscopy (HRTEM) respectively. These techniques are discussed in Sec. 2.3.1.1 and Sec 2.3.1.3 of Chapter 2 whereas Fourier transform infrared (FTIR) and Raman spectroscopy are employed to investigate the molecular and chemical bonding of the synthesized materials. The discussion related with these techniques are given in Sec. 2.3.1.2 and Sec. 2.3.1.4 of Chapter 2.

3.2.3. Electrical and electromagnetic studies

The electrical and electromagnetic studies include the study of dc conductivity and, electromagnetic interference (EMI) shielding properties of synthesized material *viz.* graphene based polypyrrole nanocomposites. They are briefly mentioned in the following subsections.

3.2.3.1. DC electrical conductivity

The dc conductivity of graphene based nanocomposites have been measured from the current-voltage data by using ohm's law. The detail of dc conductivity measurement are discussed in Sec 2.3.3.1 of Chapter 2.

3.2.3.2. Electromagnetic interference (EMI) shielding

Electromagnetic shielding behaviour and related parameter such as electrical permittivity, magnetic permeability, skin depth etc. have been measured. The details of these studies are discussed in Sec. 2.3.3.2.2 and Sec. 2.3.3.2.3 of Chapter 2.

3.3. RESULTS AND DISCUSSION

The structural and morphological studies have been carried out for graphene and polypyrrole-graphene nanocomposites. Whereas electrical and electromagnetic studies are performed for polypyrrole-graphene nanocomposites. The results of these studies are discussed in subsequent subsections.

3.3.1. Structural and morphological studies on graphene

Structural studies on graphene is carried out by using X-ray diffraction and Raman spectroscopy. The high resolution transmission electron microscopy (HRTEM) is used for investigating the morphological behaviour of synthesized graphene nanosheets. The results of these studies are discussed in following subsections.

3.3.1.1. X-ray diffraction

Fig. 3.2 shows the XRD structure of graphene. Graphene exhibits a single intense peak at $2\theta = 26^0$ corresponds to (002) plane of graphitic carbon [23].

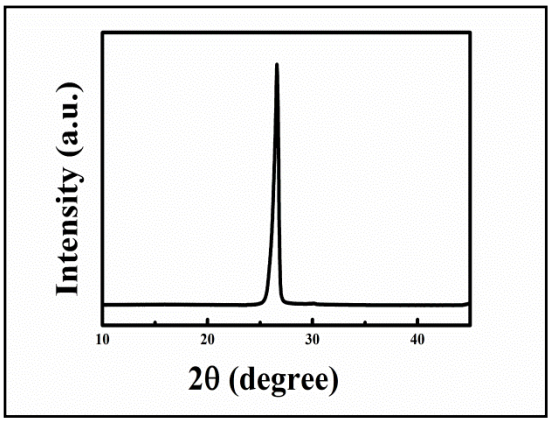

Fig. 3.2 X-ray diffraction of graphene.

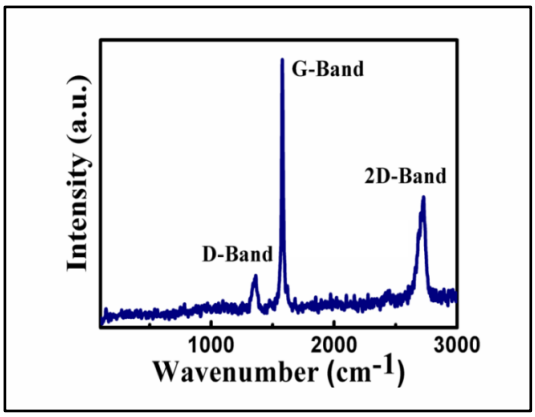

Fig. 3.3 Raman spectra of graphene.

3.3.1.2. Raman spectroscopy

Fig. 3.3 shows the Raman spectra of graphene. Raman spectra of graphene exhibits peaks at 1336 cm^{-1} (D-band) and 1575 cm^{-1} (G-band). D-band peak is associated with the vibrations of carbon atoms in in-plane discontinuation of graphite. G-band is associated with the sp^2 hybridised carbon atoms in the hexagonal structure, and is due to C=C stretching [24]. The ratio of D-band to G-band (I_D/I_G) is found to be nearly 0.26, which confirms that the synthesized graphene nanosheets consist of more than 3-layers [25,26].

3.3.1.3. High resolution Transmission electron microscopy

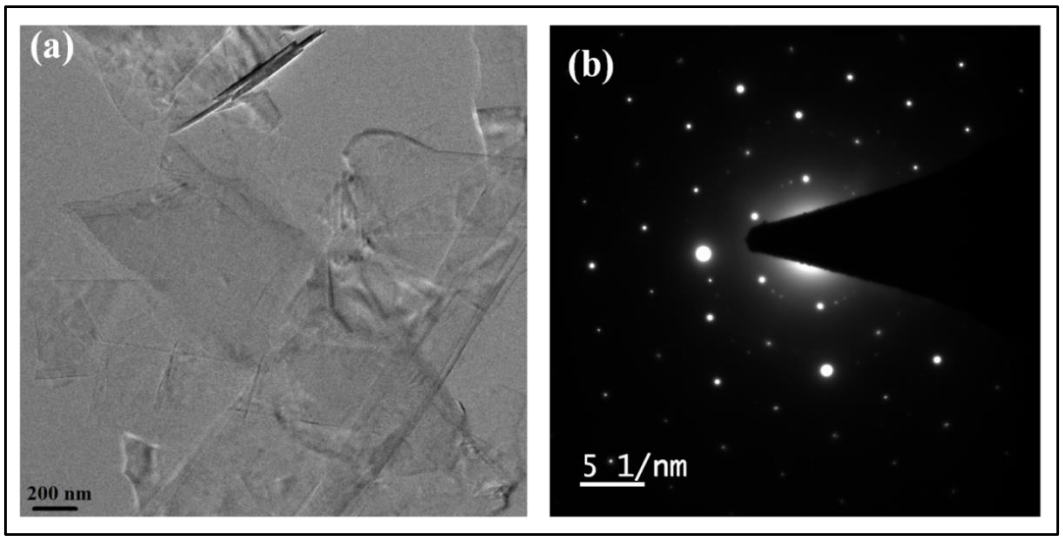

Fig. 3.4 (a) Transmission electron micrograph and (b) SAED pattern of graphene.

Fig. 3.4 shows the TEM image of graphene and SAED pattern of graphene. The TEM image of graphene shows layered structure of graphene. The formation of graphene sheet of different dimensions are also confirmed. SAED pattern of graphene shows the

hexagonal structure of graphene. The diffraction pattern exhibits the six fold symmetry of graphene which show the crystallite nature of graphene.

3.3.2. Structural and morphological studies of polypyrrole-graphene nanocomposites

Structural studies on polypyrrole-graphene nanocomposites is carried out by using X-ray diffraction, Fourier transform infrared (FTIR) and Raman spectroscopy. The HRTEM is used for investigating the morphological behaviour of synthesized nanocomposites. The results of these studies are discussed in following subsections.

3.3.2.1. X-ray diffraction

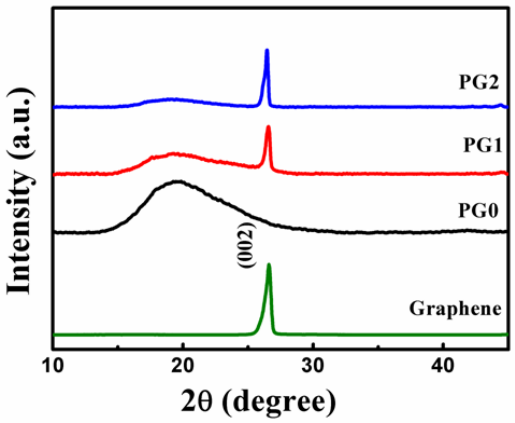

Fig. 3.5 X-ray diffraction of graphene and PG nanocomposites.

Fig. 3.5 shows the X-ray diffraction pattern of graphene, polypyrrole and polypyrrole-graphene nanocomposites. The PG0 nanocomposite i.e. the polypyrrole with no graphene, has only one broad peak lying between angle 18^0 to 22^0 confirms the amorphous nature of polypyrrole [23]. On the other hand, PG1 and PG2 nanocomposites consist of broad peak of polypyrrole as well as graphene; which confirm the formation of polypyrrole-graphene nanocomposites. The intense broad peak of polypyrrole becomes relatively weak with the incorporation of graphene in polypyrrole-graphene nanocomposite.

3.3.2.2. Fourier transform infrared spectroscopy

Fig. 3.6 shows the Fourier transform infrared spectra of Polypyrrole and PG nanocomposites. The FTIR spectra of polypyrrole nanoparticles are observed at the absorption bands of 667 cm^{-1}, 778 cm^{-1}, 894 cm^{-1},962 cm^{-1}, 1035 cm^{-1}, 1171 cm^{-1}, 1293 cm^{-1}, 1455 cm^{-1}, 1538 cm^{-1}, 2885 cm^{-1} and 3434 cm^{-1}. The absorption bands at 962 cm^{-1} and 1035 cm^{-1} are assigned to =C-H out-of-plane and in-plane deformation vibration respectively, and the bands at 667 cm^{-1} and 1455 cm^{-1} are assigned to C-C stretching vibrational mode [27]. The bands at 894 cm^{-1} and 2885 cm^{-1} are assigned to C-H stretching

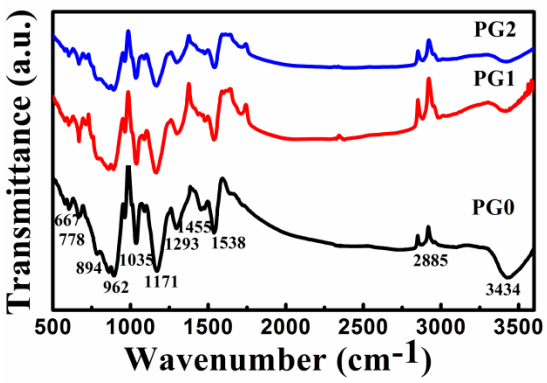

Fig. 3.6 Fourier transform infrared spectra of polypyrrole-graphene nanocomposites.

of aromatic pyrrole ring, and the band at 1538 cm^{-1} corresponds to symmetric and antisymmetric vibrational mode of pyrrole monomer ring. The broad band occurring at 3434 cm^{-1} is due to C-C and N-H symmetric stretching, and the weak band at 778 cm^{-1} is arising due to C-H vibration [28]. PG1 and PG2 nanocomposites exhibit an additional absorption band at 712 cm^{-1}, which might be resulting from the interaction of graphene nanosheets with polypyrrole chain [29].

3.3.2.3. Raman spectroscopy

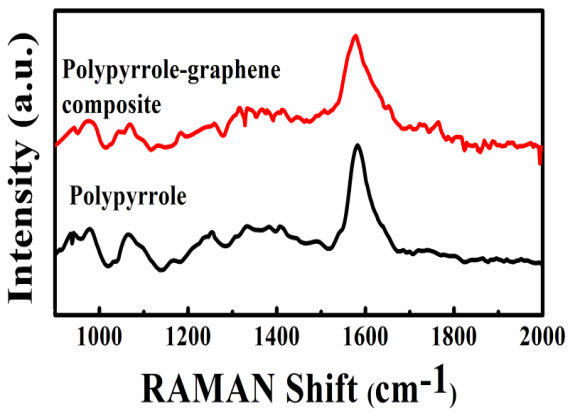

Fig. 3.7 Raman spectra of polypyrrole and polypyrrole-graphene (PG) nanocomposite.

Raman spectra of polypyrrole has a peak at 1065 cm^{-1}, which corresponds to C-H bond deformation of pyrrole ring. The less intense peaks at 942 cm^{-1} and 976 cm^{-1} are due to the distortion of pyrrole ring. The in-plane bending of C-H bond occurs at 1250 cm^{-1} and the C-N stretching occurs at 1332 cm^{-1} of pyrrole [30]. The peak at 1581 cm^{-1} belongs to the conjugation of polypyrrole. The process of vibrational mode of polypyrrole and graphene in nanocomposite confirm the formation of polypyrrole-graphene nanocomposite [31]. Fig. 3.7 shows the RAMAN spectra of polypyrrole and polypyrrole-graphene nanocomposite.

3.3.2.4. High resolution transmission electron spectroscopy

Fig. 3.8 (a, b, c) shows the transmission electron micrographs of polypyrrole and polypyrrole-graphene nanocomposites. Polypyrrole has globular or spherical type structure as shown in Fig. 3.8 (a). Fig. 3.8 (b, c) represent TEM images of PG1 and PG2 nanocomposite. The composite of polypyrrole-graphene shows the encapsulation of graphene by polypyrrole. The encapsulation of graphene in polypyrrole can be seen in the

magnified view of TEM image, as shown in inset of Fig. 3.8(c). Interfacial layer of polypyrrole-polypyrrole, polypyrrole-graphene and graphene-graphene are shown by

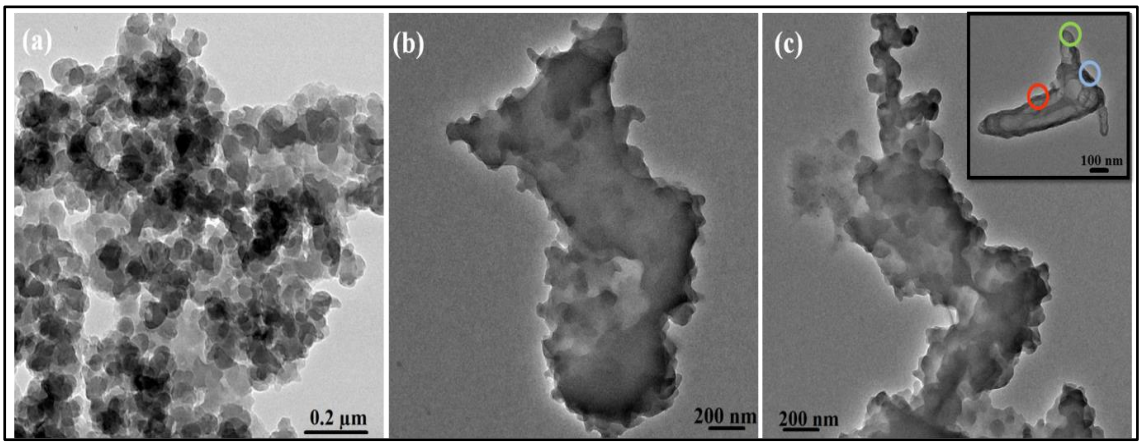

Fig. 3.8 Transmission electron micrograph of polypyrrole (a), polypyrrole-graphene nanocomposites (b, c).

blue, red and green colour circles respectively. Interfacial forces due to electronegativity difference of carbon of graphene and nitrogen of polypyrrole may be responsible for encapsulation of graphene by polypyrrole.

3.3.3. Electrical and electromagnetic studies of polypyrrole-graphene nanocomposites

The electrical and electromagnetic studies includes the study of dc conductivity and, electromagnetic interference (EMI) shielding properties of synthesized material *viz.* graphene based polypyrrole nanocomposites. The detailed analysis of microwave dielectric and shielding effectiveness and associated parameter (such as skin depth, ac conductivity, attenuation constant and impedance matching) of PG nanocomposite are carried out in X-band (8.2-12.4 GHz) of microwave region. The detailed discussion of these results and analysis are presented in subsequent subsections.

3.3.3.1. DC electrical conductivity

DC electrical conductivity of polypyrrole has been found to be ~ 1.44 S/cm. Just by adding 0.1% (w/w) graphene in polypyrrole, fivefold increase in conductivity i.e. ~ 7.51 S/cm is observed. Increase in conductivity with increase of graphene content is only found upto 0.2% (w/w) graphene. Table 3.1 shows the electrical conductivity of all the PG nanocomposites. The enhancement in conductivity of PG nanocomposite is ascribed to

highly conducting nature of graphene. But, when the graphene content becomes greater than 0.2% (w/w), conductivity starts decreasing. This decrease could be associated with shortening of mean free path of charge carrier, which arises from large number of scattering centre at the polypyrrole-graphene interface. Therefore, the microwave dielectric behaviour and shielding properties were studied for PG0, PG1 and PG2 nanocomposites.

Table 3.1. The electrical conductivity of PG nanocomposites.

Sample Name	Electrical Conductivity (S/cm)
PG0	**1.44**
PG1	**7.51**
PG2	**8.70**

3.3.3.2. Microwave dielectric and electromagnetic interference shielding

The observed microwave dielectric and electromagnetic interference (EMI) shielding behaviour of polypyrrole-graphene nanocomposite in X band (8.2-12.4 GHz), are discussed in subsequent subsections.

3.3.3.2.1 Microwave dielectric studies

Fig. 3.9 (a, b, c) shows the variation of real, imaginary part of permittivity and the dielectric loss of PG nanocomposites with frequency in X-band of microwave region. The real permittivity (ε') of all the nanocomposites decrease with increase in frequency; which is ascribed to lag in response of dipole with respect to frequency of applied ac field [32]. It is clearly observed that ε' decreases with increase in content of graphene in polypyrrole-graphene nanocomposite. The values of ε' (at 8.2 GHz) for nanocomposites PG0, PG1 and PG2 are ~ 130, 70 and 40 respectively. The decrease in ε' with the increase in graphene content might be arising due to

1. formation of series combination of large number of microcapacitors by virtue of interfacial dipole moment arising due to electronegativity difference of C of graphene and N of polypyrrole .
2. The parallel capacitance network between the polypyrrole chain is broken by incorporation of conducting graphene.

The permittivity value of PG0 exhibits a minima at ~ 11 GHz; which shows that the

dipoles of polypyrrole resonating with applied ac field [32]. The main objective of present work is to design an excellent microwave absorber. The absorbing material must exhibits the lossy behaviour so that it can easily attenuate the microwave passing through it.

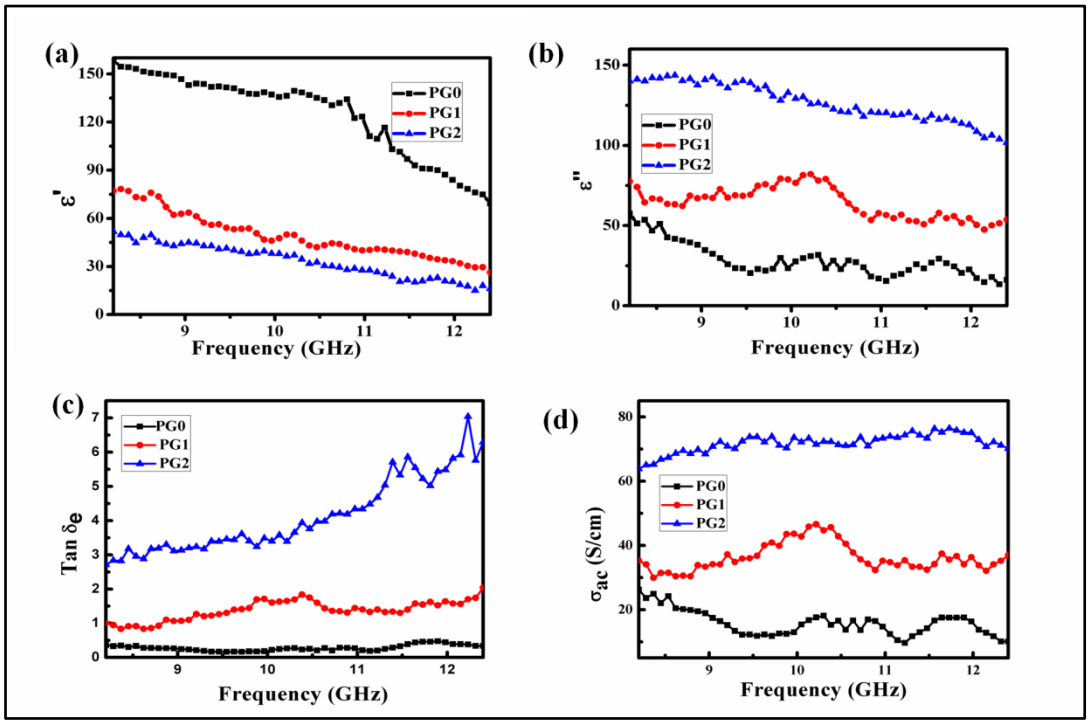

Fig. 3.9 The frequency dependence of real (a), imaginary part (b) of permittivity, dielectric loss (c) and ac conductivity (d) of PG nanocomposites.

The imaginary part of permittivity has been found to increase with the incorporation of graphene. The values of ε'' (at 8.2 GHz) are found to be ~ 56, 78 and 136 for PG0, PG1 and PG2 nanocomposites respectively. The enhancement of ε'' with increased loading of graphene leads towards increased dielectric loss (Fig. 3.9 (c)). Graphene is conducting in nature and forms conducting pathways in polypyrrole matrix; which leads to increased dielectric loss [33]. Incorporation of graphene in polypyrrole matrix results in formation of large number of interfaces, which may contribute to increased loss by interfacial polarization [34].

The variation of ac conductivity with frequency is shown in Fig. 3.9 (d). AC conductivity is found to increase with increase of graphene content in polypyrrole graphene nanocomposite. At 8.2 GHz, the value of ac conductivity for PG0 nanocomposite is ~ 25 S/m, whereas, it is ~ 65 S/m for PG2 nanocomposite. The formation of conducting pathways; and multiple relaxation processes among dipole due to interfacial effect might be responsible for enhancement of conductivity with increase in graphene content [35].

Besides, the dielectric behaviour of polypyrrole and polypyrrole-graphene nanocomposite; the relaxation behaviour of dipoles are also important. The relaxation phenomena could be understood within the frame work of Debye theory [6]. According to Debye theory, the relationship between real and imaginary permittivity can be described as [6]:

$$\varepsilon_r = \varepsilon_\infty + \frac{\varepsilon_s - \varepsilon_\infty}{1 + i\omega\tau} = \varepsilon' - j\varepsilon'' \quad \text{.....(3.1)}$$

$$\varepsilon' = \varepsilon_\infty + \frac{\varepsilon_s - \varepsilon_\infty}{1 + \omega^2\tau^2} \quad \text{..... (3.2)}$$

$$\varepsilon'' = \frac{(\varepsilon_s - \varepsilon_\infty)\omega\tau}{1 + \omega^2\tau^2} \quad \text{.....(3.3)}$$

where $\varepsilon_\infty, \varepsilon_s$, ω and τ are the permittivity at infinite frequency, static permittivity, frequency and relaxation time respectively. Hence, the relationship between ε' and ε'' can be given as:

$$(\varepsilon' - \varepsilon_\infty)^2 + (\varepsilon'')^2 = (\varepsilon_s - \varepsilon_\infty)^2 \quad \text{..... (3.4)}$$

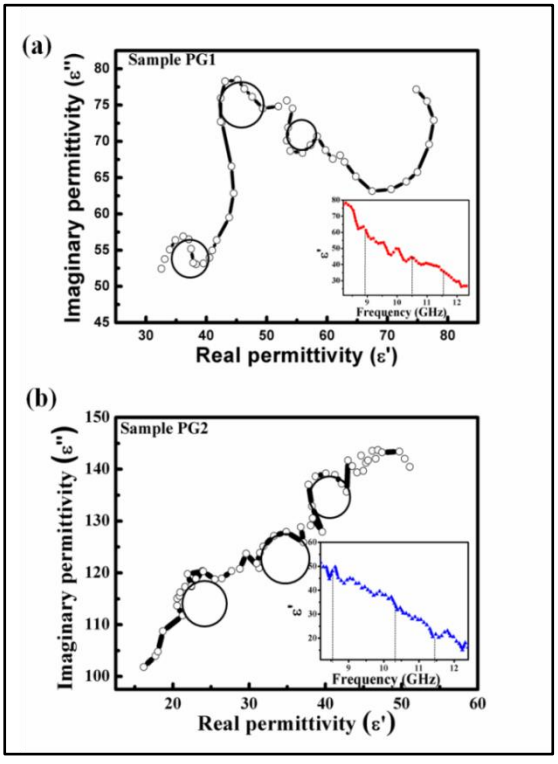

Fig. 3.10 (a, b) Cole-Cole plot of polypyrrole-graphene nanocomposites.

The curve between ε' and ε'' is Cole-Cole plot, semicircular behaviour of Cole-Cole plot represents to Debye relaxation. Fig. 3.10 (a, b) shows the cole-cole plot of PG1 and PG2 nanocomposites. Each incomplete semicircle represent dielectric relaxation. Semicircles centred around 11.6 GHz, 10.2 GHz and 9.2 GHz have been observed for PG1 nanocomposite (Fig. 3.10 (a)). The fluctuation in dielectric constant i.e. polarization behaviour has also been observed around same frequencies. Similarly, semicircles centred around 11.3 GHz, 10.3 GHz and 9.8 GHz have been observed for PG2 nanocomposite (Fig. 3.10 (b)).

The variation of dielectric constant with frequency is shown in the inset of Fig. 3.10 (a, b). Observation of semicircles is assigned to multiple relaxation elsewhere [12]. These multiple relaxation causes the enhanced microwave absorption. But exact reason for occurrence of multiple semicircle in cole-cole plot has not been described. In this work, there is the formation of large number of interfaces i.e. polypyrrole-polypyrrole, polypyrrole-graphene and graphene-graphene. Moreover, some interfacial charges are also being developed at interfaces. Combined effect of interfacial charges and three kind of interfaces in PG nanocomposites cause delay in molecular polarization with respect to change in frequency of applied field. Presence of these interfaces causes multiple relaxation; which leads to increased microwave absorption behaviour [12].

3.3.3.2.2. Electromagnetic Interference shielding

Microwave shielding is defined as the attenuation of microwave by the process of reflection, absorption and transmission. The total shielding effectiveness (SE_T) is given by [10]:

$$SE_T = SE_A + SE_R + SE_M \quad \text{.....(3.5)}$$

where SE_A, SE_R and SE_M are shielding effectiveness due to absorption, reflection and multiple reflection respectively. When the value of $SE_T > 10$ dB, SE_M can be neglected. Thus, the shielding effectiveness due to absorption (SE_A) and reflection (SE_R) can be calculated as [10]:

$$SE_R = -10log_{10}(1 - R) \quad \text{.....(3.6)}$$

$$SE_A = 10\log(1 - A_{eff}) = -10log(T/1 - R) \quad \text{.....(3.7)}$$

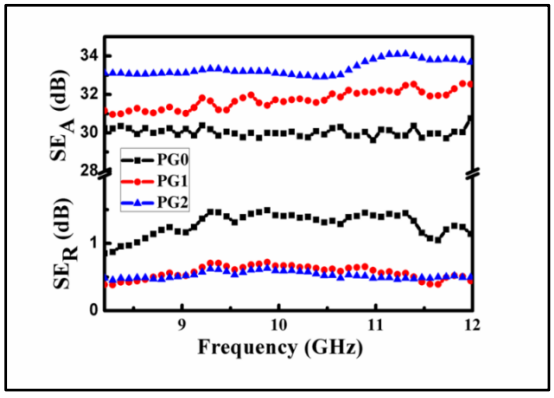

Fig. 3.11 Variation of SE_A and SE_R with frequency in X-band.

The reflectance (R) and effective absorbance (A_{eff}) are calculated from scattering parameters. The variation of shielding effectiveness with frequency for all the nanocomposites measured in X-band (8.2 – 12.4 GHz) are shown in Fig. 3.11. The shielding effectiveness due to absorption (SE_A) are found to be ~ 30 dB, 31 dB and 33 dB for PG0, PG1 and PG2 nanocomposites

respectively at 8.2 GHz. The shielding effectiveness due to absorption increases from PG0 to PG2 because of the presence of extremely high conductive graphene sheets. The value of SE_R is nearly 1 dB for all the nanocomposites. SE_A is more dominating than SE_R as shown in Fig. 3.11. Incorporation of graphene in polypyrrole-graphene nanocomposite is increasing the shielding effectiveness by absorption. Moreover, SE_A also remain stable with frequency in X-band region of microwave. Enhancement in microwave absorption due to increase in graphene content is attributed to increased dielectric loss; which attenuate microwave in X-band region of microwave [6]. Increased dielectric loss is ascribed to interfacial polarization and multiple relaxation as discussed in previous section [34].

In order to develop more understanding about microwave absorption behaviour of polypyrrole-graphene nanocomposite, SE_A and SE_R are analyzed in view of AC conductivity and skin depth. According to classical electromagnetic theory, the SE due to absorption and reflection can be expressed as [9]:

$$SE_A(dB) = 20\left(\frac{t}{\delta}\right) loge = 20t\sqrt{\frac{\mu_r \omega \sigma_{ac}}{2}}\, loge \quad \text{.....(3.8)}$$

$$SE_R(dB) = 10log\left(\frac{\sigma_{ac}}{16\omega\varepsilon_0\mu'}\right) \quad \text{.....(3.9)}$$

where σ_{ac} is the conductivity and is given as $\sigma_{ac} = \omega\varepsilon_0\varepsilon''$ and δ is the skin depth which is given as $\delta = \sqrt{2/\sigma\omega\mu'}$ where μ' is the permeability, t is the sample thickness of the material.

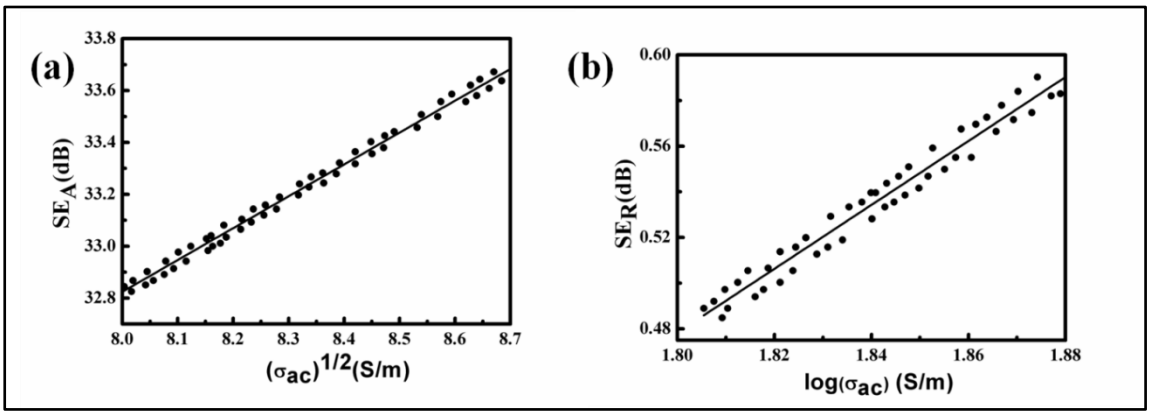

Fig. 3.12 (a, b) Variation of SE_A vs $(\sigma_{ac})^{1/2}$ and SE_R vs $\log(\sigma_{ac})$ of PG2 nanocomposite where σ_{ac} is the ac conductivity.

SE_A and SE_R are showing the linear variation with $(\sigma_{ac})^{1/2}$ and $\log(\sigma_{ac})$ respectively as shown in Fig. 3.12 (a, b). SE_A is very high as compared to SE_R in X-band; which is attributed to shallow skin depth and high conductivity at high frequencies [12].

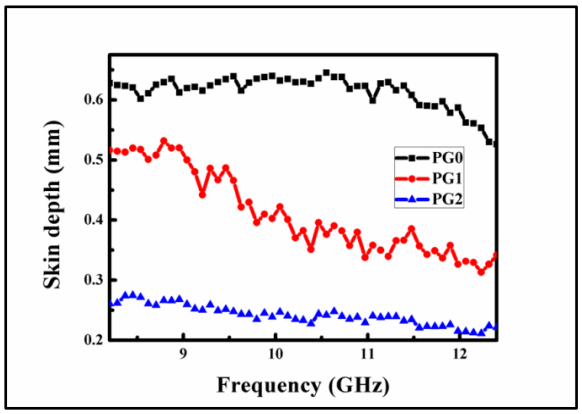

Fig. 3.13 Variation of skin depth with frequency of PG0, PG1 and PG2 nanocomposites.

Thickness of material employed for microwave absorption and shielding is one of the important parameter. Minimum thickness of shield material is always desirable; which is decided by skin depth of shield material. Fig. 3.13 shows that the skin depth decreases with increase in graphene content in polypyrrole-graphene nanocomposite. The value of skin depth for PG2 nanocomposite is ~ 250 µm; which is very less. The increase in graphene reduces the skin depth values and prevents the penetration of EM wave inside the material. One more parameter, attenuation constant tells about the property of material to attenuate the microwave. The microwave attenuation constant (α) is estimated by the formula [6]:

$$\alpha = \frac{\sqrt{2}\pi f}{c}\sqrt{(\mu''\varepsilon'' - \mu'\varepsilon') + \sqrt{(\mu''\varepsilon'' - \mu'\varepsilon')^2 + (\mu'\varepsilon'' + \varepsilon'\mu'')^2}} \quad \text{.....(3.10)}$$

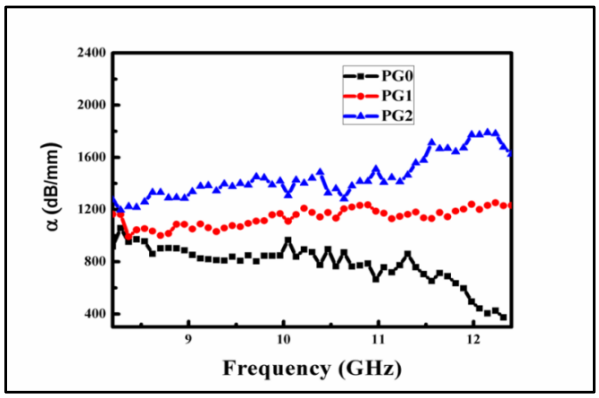

Fig. 3.14 Variation of attenuation constant of PG nanocomposites.

The microwave attenuation constant (α) with frequency for all the PG nanocomposites is shown in Fig. 3.14. The PG2 nanocomposite shows the maximum microwave attenuation which results in higher shielding effectiveness of PG2 nanocomposite. Observed highest value of microwave attenuation coefficient is also ascribed to formation of large number of interfaces in PG2 nanocomposite and high dielectric loss by virtue of encapsulation of graphene by polypyrrole. Along with increased shielding effectiveness by absorption, decreased reflection is required for various applications mentioned earlier [14,16,36,37].

Shielding effectiveness by reflection (SE_R) is << 1 dB; for PG1 and PG2 nanocomposite. Therefore, attenuation of microwave by process of reflection is negligibly small. The reflection loss can be given as [38]:

$$R_L = 20log\left|\frac{Z_{in}-Z_o}{Z_{in}+Z_o}\right| \quad \text{.....(3.11)}$$

where Z_{in} and Z_o are the input impedance and impedance in air of microwave shielding material. The input impedance can be calculated as [38]:

$$Z_{in} = Z_o\left(\frac{\mu_r}{\varepsilon_r}\right)^{1/2}\tanh\left\{j\left(\frac{2\pi fd}{c}\right)\left(\mu_r\varepsilon_r\right)^{1/2}\right\} \quad \text{.....(3.12)}$$

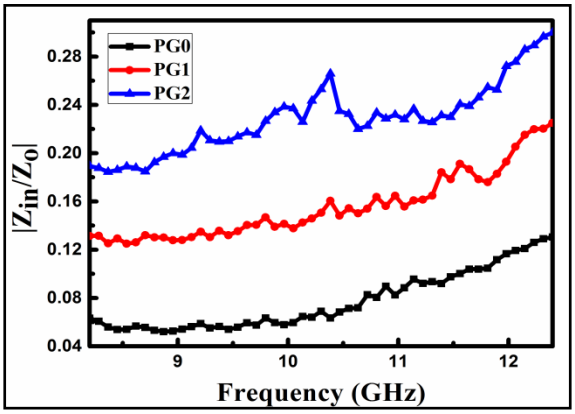

Fig. 3.15 Variation of $|Z_{in}/Z_o|$ of PG nanocomposites in X-band.

For the good matching impedance, the ratio of impedances i.e. $|Z_{in}/Z_o| \approx 1$. Fig. 3.15 shows the variation of $|Z_{in}/Z_o|$ with frequency for all the PG nanocomposites, and the values are less than 1 for all the nanocomposites, which is attributed to suppressed microwave reflection of polypyrrole- graphene nanocomposite. Our investigation and analysis of microwave dielectric behaviour, and shielding effectiveness confirm that PG2 nanocomposite is excellent microwave absorber along with very small value of skin depth. Microwave dielectric behaviour and shielding effectiveness have been investigated and analyzed at all parameters. It is found that PG2 nanocomposite exhibit very good microwave absorption along with reduced reflection << 1 dB. The qualitative explanation about the mechanism of microwave absorption and reflection behaviour is discussed in the following subsection.

3.3.3.2.2.1. Mechanism of absorption and reflection behaviour

Slight reflection of electromagnetic wave is arising due to conducting nature of graphene and polypyrrole. But, EMI shielding is dominated by absorption of microwave instead of reflection. Electronegativity difference of carbon of graphene and nitrogen of polypyrrole provides the interfacial force which encapsulate graphene nanosheets by polypyrrole. Various kinds of interfaces such as polypyrrole-polypyrrole (lateral and longitudinal), polypyrrole-graphene, graphene-graphene are also present in polypyrrole-graphene

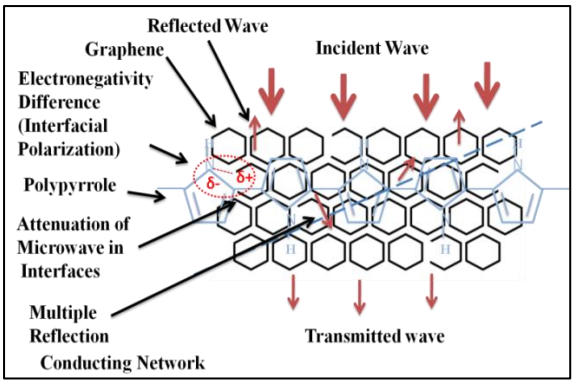

Fig. 3.16 Mechanism of EMI shielding of polypyrrole-graphene nanocomposites.

nanocomposites. These interfaces cause interfacial polarization; which leads to multiple dielectric relaxation. Multiple dielectric relaxation is confirmed from analysis of dielectric behaviour and cole-cole plot. Multiple dielectric relaxation enhances the microwave absorption [39]. Mechanism of shielding of electromagnetic wave of graphene encapsulated polypyrrole-graphene nanocomposite is shown in Fig. 3.16. The comparison of material thickness, SE_A, SE_R, skin depth and electrical conductivity of various composite materials with graphene encapsulated polypyrrole-graphene nanocomposite are shown in Table 3.2.

Table 3.2. Comparison of thickness of material (t), electromagnetic shielding effectiveness due to absorption (SE_A), due to reflection (SE_R), skin depth (δ) and electrical conductivity (σ) of various composite materials reported in literature with polypyrrole-graphene nanocomposite in X band of microwave region.

S.No.	Material with filler loading	t (mm)	SE_A (dB)	SE_R (dB)	δ (mm)	σ_{ac} (S/cm)	Ref.
1.	4 wt% $PbTiO_3$ in $PbTiO_3$/RGO/poly(3,4-ethylenedioxythiophene) composite	2.5	46.1	8	0.45	-	3
2.	3D faceted-Fe_3O_4-vertical carbon nanotubes (VCNT)@reduced graphene oxide (RGO) hybrids	1	25	2	0.34	-	7
3.	1 wt% of MWCNT in polycarbonate/poly(styrene-co-acrylonitrile) multiwalled CNT composite	10	22	1.5	3.8	0.0834	10
4.	7 wt% of *in-situ* reduced graphene oxide (IRGO) in ethylene methyl acrylate-IRGO composite	-	1.4	34	1.5	10^{-6}	17
5.	2.94 vol% of CNT in Polyetherimide/carbon nanotube(CNT) foam	-	32.3	5.6	0.43	0.164	21
6.	0.2 wt% of graphene in polypyrrole-graphene composite	2	33	< 1	0.25	8.1	Present Study

3.4. CONCLUSION

Polypyrrole encapsulated graphene (PG) nanocomposite has been successfully synthesized by *in-situ* chemical oxidative polymerization. Microwave shielding and dielectric behaviour of these nanocomposites have been investigated. The PG2 nanocomposite containing 0.2 wt% of graphene exhibits maximum shielding effectiveness due to absorption (SE_A) of ~ 33 dB and suppressed shielding effectiveness due to reflection (SE_R) < 1 dB in X-band (8.2-12.4 GHz) of microwave region. Apart from enhanced SE_A, PG2 nanocomposite shows very low value of skin depth (~ 250 μm) and increased attenuation constant. Enhanced microwave absorption of PG2 nanocomposite is attributed to increased dielectric loss arising due to conducting pathways, interfacial polarization and multiple relaxation. This investigation could be useful for development of novel material having very good microwave absorbing characteristic; which could be useful for defence, and microwave communication applications.

REFERENCES

1 Y. Xu, Y. Yang, D. X. Yan, H. Duan, G. Zhao and Y. Liu, *ACS Appl. Mater. Interfaces*, 2018, **10**, 19143–19152.

2 Y. Zeng, X. Luo, K. Yu and K. Qian, *Chem. Phys. Lett.*, 2019, **715**, 166–172.

3 J. Dalal, S. Lather, A. Gupta, S. Dahiya, A. S. Maan, K. Singh, S. K. Dhawan and A. Ohlan, *Compos. Sci. Technol.*, 2018, **165**, 222–230.

4 H. Wei, J. Dong, X. Fang, W. Zheng, Y. Sun, Y. Qian, Z. Jiang and Y. Huang, *Compos. Sci. Technol.*, 2019, **169**, 52–59.

5 K. Singh, A. Ohlan, V. H. Pham, R. B. Balasubramaniyan, S. Varshney, J. Jang, S. H. Hur, W. M. Choi, M. Kumar, S. K. Dhawan, B. S. Kong and J. S. Chung, *Nanoscale*, 2013, **5**, 2411–2420.

6 X. Wang, B. Wen and X. Yang, *Compos. Part B Eng.*, 2019, **173**, 106904.

7 R. Kumar, A. V. Alaferdov, R. K. Singh, A. K. Singh, J. Shah, R. K. Kotnala, K. Singh, Y. Suda and S. A. Moshkalev, *Compos. Part B Eng.*, 2019, **168**, 66–76.

8 L. C. Jia, D. X. Yan, X. Jiang, H. Pang, J. F. Gao, P. G. Ren and Z. M. Li, *Ind. Eng. Chem. Res.*, 2018, **57**, 11929–11938.

9 N. Gill, A. L. A. L. Sharma, V. Gupta, M. Tomar, O. P. Pandey and D. P. Singh, *J. Alloys Compd.*, 2019, **797**, 1190–1197.

10 H. Bizhani, V. Nayyeri, A. A. Katbab, A. Jalali-Arani and H. Nazockdast, *Eur. Polym. J.*, 2018, **100**, 209–218.

11 H. Hu, T. Gao, X. Zhao, J. Zhang, Y. Zhang, G. Qin and X. Zhang, *Carbon*, 2019, **153**, 330–336.

12 G. Datt, C. Kotabage and A. C. Abhyankar, *Phys. Chem. Chem. Phys.*, 2017, **19**, 20699–20712.

13 L. Jin, X. Zhao, J. Xu, Y. Luo, D. Chen and G. Chen, *RSC Adv.*, 2018, **8**, 2065–2071.

14 H. Zhu, Y. Yang, A. Sheng, H. Duan, G. Zhao and Y. Liu, *Appl. Surf. Sci.*, 2019,

469, 1–9.

15 L. Monnereau, L. Urbanczyk, J.-M. Thomassin, T. Pardoen, C. Bailly, I. Huynen, C. Jérôme and C. Detrembleur, *Polymer*, 2015, **59**, 117–123.

16 Y. Hu, D. Li, L. Wu, J. Yang, X. Jian and Y. Bin, *Compos. Sci. Technol.*, 2019, **181**, 107699.

17 G. George, S. M. Simon, V. Prakashan, M. Sajna, M. Faisal, R. Wilson, A. Chandran, P. R. Biju, C. Joseph and N. V. Unnikrishnan, *RSC Adv.*, 2018, **8**, 30412–30428.

18 X. Ma, B. Shen, L. Zhang, Y. Liu, W. Zhai and W. Zheng, *Compos. Sci. Technol.*, 2018, **158**, 86–93.

19 S. Maiti, R. Bera, S. K. Karan, S. Paria, A. De and B. B. Khatua, *Compos. Part B Eng.*, 2019, **167**, 377–386.

20 Q. Jiang, X. Liao, J. Li, J. Chen, G. Wang, J. Yi, Q. Yang and G. Li, *Compos. Part A Appl. Sci. Manuf.*, 2019, **123**, 310–319.

21 D. Feng, P. Liu and Q. Wang, *Compos. Part A Appl. Sci. Manuf.*, 2019, **124**, 105463.

22 P. Jayamurgan, V. Ponnuswamy, S. Ashokan and T. Mahalingam, *Iran. Polym. J.*, 2013, **22**, 219–225.

23 D. Zhang, X. Zhang, Y. Chen, P. Yu, C. Wang and Y. Ma, *J. Power Sources*, 2011, **196**, 5990–5996.

24 M. Cai, D. Thorpe, D. H. Adamson and H. C. Schniepp, *J. Mater. Chem.*, 2012, **22**, 24992–25002.

25 M. Lotya, A. Rakovich, J. F. Donegan and J. N. Coleman, *Nanotechnology*, 2013, **24**, 265703.

26 Y. Hernandez, V. Nicolosi, M. Lotya, F. M. Blighe, Z. Sun, S. De, I. T. McGovern, B. Holland, M. Byrne, Y. K. Gun'ko, J. J. Boland, P. Niraj, G. Duesberg, S. Krishnamurthy, R. Goodhue, J. Hutchison, V. Scardaci, A. C. Ferrari and J. N. Coleman, *Nat. Nanotechnol.*, 2008, **3**, 563–568.

27 J. Luo and D. Gao, *J. Magn. Magn. Mater.*, 2014, **368**, 82–86.

28 J. Lei, W. Liang and C. R. Martin, *Synth. Met.*, 1992, **48**, 301–312.

29 N. Gandhi, K. Singh, A. Ohlan, D. P. Singh and S. K. Dhawan, *Compos. Sci. Technol.*, 2011, **71**, 1754–1760.

30 Y. Xie and H. Du, *RSC Adv.*, 2015, **5**, 89689–89697.

31 S. Biswas and L. T. Drzal, *Chem. Mater.*, 2010, **22**, 5667–5671.

32 J. Luo, Y. Zuo, P. Shen, Z. Yan and K. Zhang, *RSC Adv.*, 2017, **7**, 36433–36443.

33 F. Ren, D. Song, Z. Li, L. Jia, Y. Zhao, D. Yan and P. Ren, *J. Mater. Chem. C*, 2018, **6**, 1476–1486.

34 N. N. Beladakere, S. C. K. Misra, M. K. Ram, D. K. Rout, R. Gupta, B. D. Malhotra and S. Chandra, *J. Phys. Condens. Matter*, 1992, **4**, 5747–5756.

35 M. Mishra, A. P. Singh, B. P. Singh, V. N. Singh and S. K. Dhawan, *J. Mater. Chem. A*, 2014, **2**, 13159–13168.

36 Y. Xu, Y. Yang, D.-X. Yan, H. Duan, G. Zhao and Y. Liu, *ACS Appl. Mater. Interfaces*, 2018, **10**, 19143–19152.

37 A. Balmori, *Pathophysiology*, 2009, **16**, 191–199.

38 D. Moitra, S. Dhole, B. K. Ghosh, M. Chandel, R. K. Jani, M. K. Patra, S. R. Vadera and N. N. Ghosh, *J. Phys. Chem. C*, 2017, **121**, 21290–21304.

39 X. Jian, B. Wu, Y. Wei, S. X. Dou, X. Wang, W. He and N. Mahmood, *ACS Appl. Mater. Interfaces*, 2016, **8**, 6101–6109.

CHAPTER 4

STUDIES ON ELECTROMAGNETIC SHIELDING BEHAVIOUR OF POLYPYRROLE-COBALT FERRITE-GRAPHENE NANOCOMPOSITES

4.1. INTRODUCTION

Design and development of electromagnetic interference (EMI) shielding materials have attracted a lot of attention because of its industrial, defence and electronics applications [1–3]. EMI shielding in a material is achieved by process of reflection, absorption and multiple reflection of electromagnetic wave. Shielding effectiveness by reflection (SE_R) is achieved in highly conducting material such as metals. Metal shield exhibits very good electromagnetic reflection; but they have several disadvantages such as high cost, high density, corrosion etc [4]. To achieve the shielding effectiveness by absorption (SE_A); the material should be either magnetic or dielectric. When an EM wave is incident on such material; it will create an internal magnetic field and electric field which may lead/lag with respect to applied field. Accordingly, magnetic loss and dielectric loss is created which is responsible for shielding effectiveness by absorption [5]. In contrast to metal, the polymer based nanocomposites are advantageous as they have low density, easy to process, free from corrosion, and can be applied over large area [6]. The combination of moderate conducting material with dielectric/magnetic material has been proven to be excellent EMI shielding material [7–9]. The conducting polymer based composite such as PANI/$CoFe_2O_4$ [7], Ppy/ferrofluid [8], Fe_3O_4@polypyrrole [9], have been investigated for this purpose. The inclusion of carbon based material in conducting polymers has also been found to exhibit good shielding effectiveness (SE) [10]. Carbon material used for this purpose, include graphite [11] , carbon black [12], carbon fibre [13], reduced graphene oxide [14], graphene [15] etc. Polymer based composite with very small amount of ceramic/carbon material filler will not compromise with the mechanical strength [16]. Therefore, conducting polymer based composite with low filler content of ceramic/carbon material would be extremely useful. Shielding behaviour of a material in X-band (i.e. 8.2 – 12.4 GHz) of microwave is of particular importance for Doppler weather radar, TV transmission, vehicular detection, defence trading etc [17]. More SE_A along with negligible SE_R is important for aerospace application, better known as “stealth technology” [18], where microwave transmitter RADAR does not have capability to locate the position and velocity of aircraft. Degree of SE_A for this purpose should be greater than ~ 30 dB. Various studies are available in literature related to the investigation of SE in X-band [17]. Shielding effectiveness (SE) of functionalized graphene/PVDF composite has reported SE_T ~ 20 dB in X-band for 5 wt% of functionalized graphene and also observed the drastic change in conductivity from 10^{-16} S/m for pure PVDF to 10^{-4} S/m for 0.5 wt%

functionalized graphene for functionalised graphene/PVDF nanocomposite [19]. Observed SE is attributed to increase in conductivity of foam composite by formation of graphene conducting network in PVDF matrix. Graphene foam/conducting polymer (PEDOT: PSS) composites have shown the excellent EMI shielding behaviour in X-band [20]. Though, SE_R and SE_A have been found to be ~ 10 dB and ~ 60 dB respectively. Inherent conducting network and porous structure of graphene has been assigned as cause for high shielding effectiveness. Structurally, reduced graphene oxide (RGO)/ Polystyrene (PS) composite exhibits SE_T ~ 30 dB for shield thickness of 2 mm. The shielding effectiveness by reflection (SE_R) is also found to be reduced to ~ 1 dB. The segregated architecture of RGO/PS provides numerous reflecting and absorbing surfaces that leads to enhanced shielding effectiveness [16]. Graphene/PVA/Fe_3O_4 composite has shown the SE_T of ~ 12 dB for very low shield thickness of 0.3 mm [21]. The occurrence of interfacial polarization due to accumulation of charges at interfaces and formation of large dipoles is assigned as a cause for observed SE. Zhang *et al*. [22] observed ultralow percolation threshold and enhanced EMI shielding in poly (L-lacide)/multiwalled carbon nanotube nanocomposites. SE_R of ~ 5 dB and SE_T of ~ 30 dB have been reported. The observed shielding effectiveness is mainly attributed to abundant interfaces produced by segregated structure. SE of ferroelectric polymer/graphene nanocomposite has also been investigated [23], where SE_R and SE_A are found to be ~ 3 dB and ~ 23 dB respectively. Some studies are focussed for search of good microwave absorbing and less microwave reflecting material [17,21,22].

Studies on conducting polymer based composites have made it clear that moderate conductivity along with very good dielectric and magnetic behaviour is essential for very good microwave absorption. The multicomponent material consisting of polypyrrole-cobalt ferrite-graphene has been synthesized in order to develop a novel EMI shielding material. Here, in the present chapter the microwave absorption and shielding effectiveness behaviour of polypyrrole-cobalt ferrite-graphene nanocomposite have been carried out in X-band (8.2-12.4 GHz). The detailed account of correlation among the shielding effectiveness, permittivity, permeability and ac conductivity has also been discussed.

4.2. EXPERIMENTAL

The experimental section includes the synthesis of materials, structural, morphological and magnetic studies, electrical and electromagnetic shielding of nanocomposites, which

are described in subsequent sections.

4.2.1. Synthesis of materials

Graphene and cobalt ferrite have been synthesized by liquid phase exfoliation (Sec. 2.2.1.1) and hydrothermal method (Sec. 2.2.2.2) respectively. The as-synthesized graphene nanosheets and cobalt ferrite nanoparticles have been further used in polymerization with pyrrole monomer to get polymer nanocomposites (Sec. 2.2.3.1). A brief account of synthesis is described in the subsequent subsections.

4.2.1.1. Synthesis of materials

Cobalt ferrite nanoparticles have been synthesized by hydrothermal method. The stoichiometric amount of nitrates were dissolved in distilled water and pH of above solution was maintained at 12. The solution was transferred to Teflon-lined autoclave for 18 h at 180^{o}C. The resulting precipitates were filtered and washed many times to get cobalt ferrite nanoparticles.

4.2.1.2. Synthesis of graphene

The synthesis of graphene has been carried out by liquid phase exfoliation method which has been discussed in detail in Sec. 2.2.1.1, where the graphite flakes are dissolved in N-methyl-2-pyrrolidene (NMP) solution by using tip sonicator for 2 *h* at an amplitude of 60%. The dispersed solution was left overnight to settle down the unexfoliated graphite. The dispersed solution was centrifuged at 750 rpm for 90 min to remove the unexfoliated graphite. The upper 70% solution was removed and filtered. The filtered material was dried in vacuum oven at 60^{o} to get the graphene nanosheets.

4.2.1.3. Synthesis of polypyrrole-cobalt ferrite-graphene (PCG) nanocomposite

Polypyrrole-cobalt ferrite-graphene (PCG) nanocomposite has been synthesized by *in-situ* chemical oxidative polymerization where graphene nanosheets and cobalt ferrite nanoparticles were homogeneously dispersed in polypyrrole matrix. The cobalt ferrite nanoparticles and graphene were homogenized in 0.01M dodecylbenzene sulfonic acid (DBSA) solution by stirring them at 5000 rpm to get the uniform dispersion. Pyrrole monomer was added drop wise to this solution during continuous stirring for 1 h. DBSA to pyrrole monomer ratio was taken as 1:2.33 during the complete reaction.

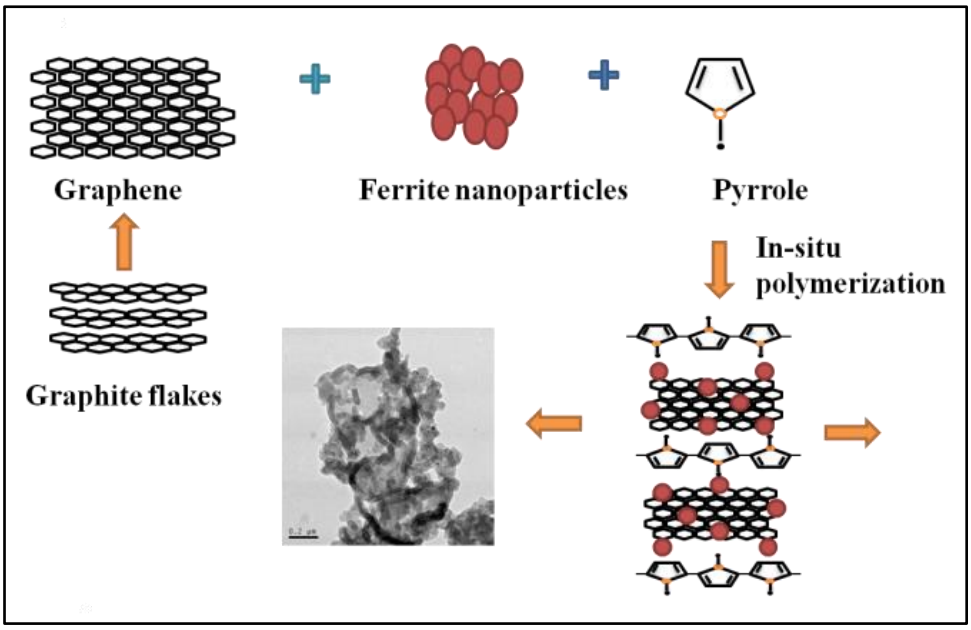

Fig. 4.1 Schematic representation of the synthesis of the polypyrrole-cobalt ferrite-graphene (PCG) nanocomposite by *in-situ* polymerization.

Temperature of solution containing pyrrole monomer, $CoFe_2O_4$ and graphene in DBSA was kept in range of 0-10 $^{\circ}$C. 0.1M $FeCl_3$ was added drop wise in the resulting solution which was subjected to continuous stirring for 12 h. The temperature was maintained at 0-10 $^{\circ}$C. The obtained black precipitates were washed thoroughly with ethanol to remove all impurities and dried at 60 $^{\circ}$C for 24 h in an oven. In order to synthesize PCG nanocomposites, composition of pyrrole monomer: cobalt ferrite: graphene in different composites were taken as 1:0.5:0, 1:0.5:0.1, 1:0.5:0.2 and 1:0.5:0.3 by weight which were designated as PCG0, PCG1, PCG2 and PCG3 respectively. The schematic representation of the synthesis of the polypyrrole-cobalt ferrite-graphene nanocomposite by *in-situ* polymerization is shown in Fig. 4.1.

4.2.2. Structural, morphological and magnetic studies

X-ray diffraction and transmission electron microscopy have been employed to determine the crystalline size and surface morphology respectively. The discussion related with these techniques have been given in Sec. 2.3.1.1 and Sec. 2.3.1.3 of Chapter 2. The Fourier transform infrared (FTIR) and Raman spectroscopy are used to understand the chemical and molecular bonding in the synthesized materials. The detailed discussion of these techniques have been given in Sec. 2.3.1.2 and Sec. 2.3.1.4 of Chapter 2. Vibrating sample magnetometer (Sec. 2.3.2.1) has been employed to detect the magnetic behaviour of magnetic nanoparticles and nanocomposites.

4.2.3. Electrical and electromagnetic studies

The electrical and electromagnetic studies include the dc conductivity and electromagnetic interference shielding behaviour of synthesized nanocomposites. These are briefly discussed in the subsequent subsection.

4.2.3.1. DC Electrical studies

The two probe method has been used to carried out the current-voltage (I-V) measurements. The electrical conductivity has been measured from the I-V values, which has been discussed in Sec. 2.3.3.1 of Chapter 2 .

4.2.3.2. Electromagnetic interference (EMI) studies

Electromagnetic shielding has been carried out by measuring Scattering parameters of all the nanocomposites. The electromagnetic shielding parameters such as dielectric permittivity, magnetic permeability, skin depth and ac conductivity have been discussed in details in Sec 2.3.3.2.2 of Chapter 2.

4.3. RESULTS AND DISCUSSION

The structural and morphological studies have been carried out for graphene nanosheets, cobalt ferrite nanoparticles and polypyrrole-cobalt ferrite-graphene nanocomposites. The magnetic studies have been done on cobalt ferrite nanoparticles and polypyrrole-cobalt ferrite-graphene nanocomposites. The electrical and electromagnetic studies have been performed for polypyrrole-graphene-cobalt ferrite nanocomposites. The results for all these studies have been given in following subsections.

4.3.1. Structural, morphological and magnetic studies of cobalt ferrite

Structural studies on cobalt ferrite has been carried out by using X-ray diffraction and Fourier transform infrared spectroscopy. The surface morphology and particle size have been determined by high resolution transmission electron microscopy and, magnetic studies has been done by vibrating sample magnetometer. The results of these studies have been given in following subsections.

4.3.1.1 X-ray diffraction

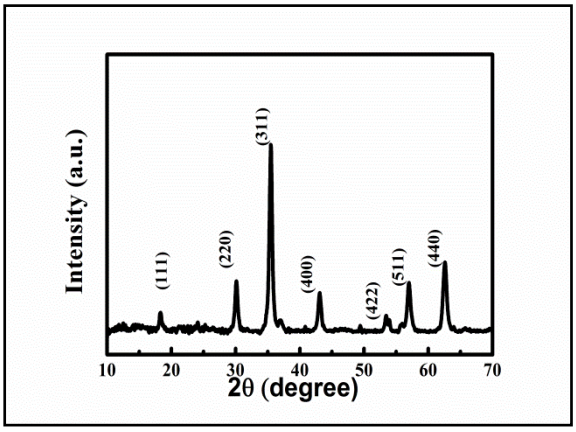

Fig. 4.2 X-ray diffraction of cobalt ferrite nanoparticles.

The X-ray diffraction of cobalt ferrite nanoparticles have been shown in Fig. 4.2. The peaks of cobalt ferrite are observed at an angles of $2\theta = 18.2^0$, 30.1^0, 35.6^0, 37.05^0, 43.1^0, 53.5^0, 57.1^0 and 62.5^0, which corresponds to (111), (220), (311), (222), (400), (422), (511) and (440) lattice planes respectively [24]. All the observed peaks of $CoFe_2O_4$ are matched with the standard pattern of XRD (JCPDS card no 22-1086). The crystallite size of $CoFe_2O_4$ has been calculated using Scherer's formula and estimated to be ~ 17 nm.

4.3.1.2 Fourier transform infrared spectroscopy

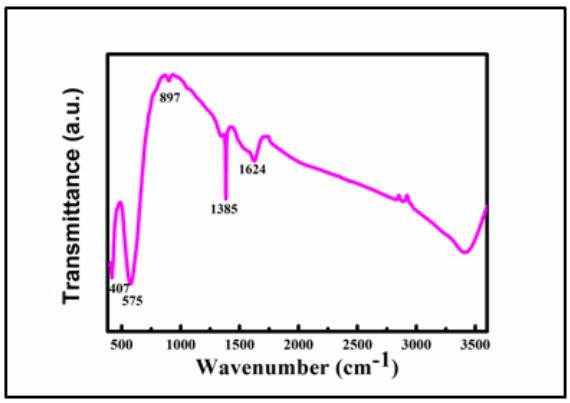

Fig. 4.3 Fourier transform infrared spectra of cobalt ferrite nanoparticles.

Fig. 4.3 shows the Fourier transform infrared spectra of cobalt ferrite nanoparticles. From the bottom, the characteristic peaks of cobalt ferrite are observed at 575 cm^{-1} and 407 cm^{-1} which represent the Fe-O stretching vibration in tetrahedral sites and Co-O vibration in octahedral sites respectively which is observed due to spinal structure of ferrite. The antisymmetric vibrational stretching of C=C group, symmetric stretching of carboxylic (C=O) group and out of plane bending vibrational peak of C-C group of cobalt ferrite are observed at 1624 cm^{-1}, 1385 cm^{-1} and 897 cm^{-1} [24].

4.3.1.3 High resolution transmission electron microscopy

Fig. 4.4 (a) shows the transmission electron micrograph of cobalt ferrite nanoparticles. TEM image of $CoFe_2O_4$ ferrite shows the presence of semi-spherical particles with some degree of agglomeration. The mean size of the nanoparticles is found to be ~ 21 nm.

The selected area diffraction pattern (SAED) pattern of ferrite is shown in Fig. 4.4 (b) where all planes corresponding to $CoFe_2O_4$ are indexed. The formation of bright rings in SAED pattern confirm the crystalline nature of ferrite nanoparticles.

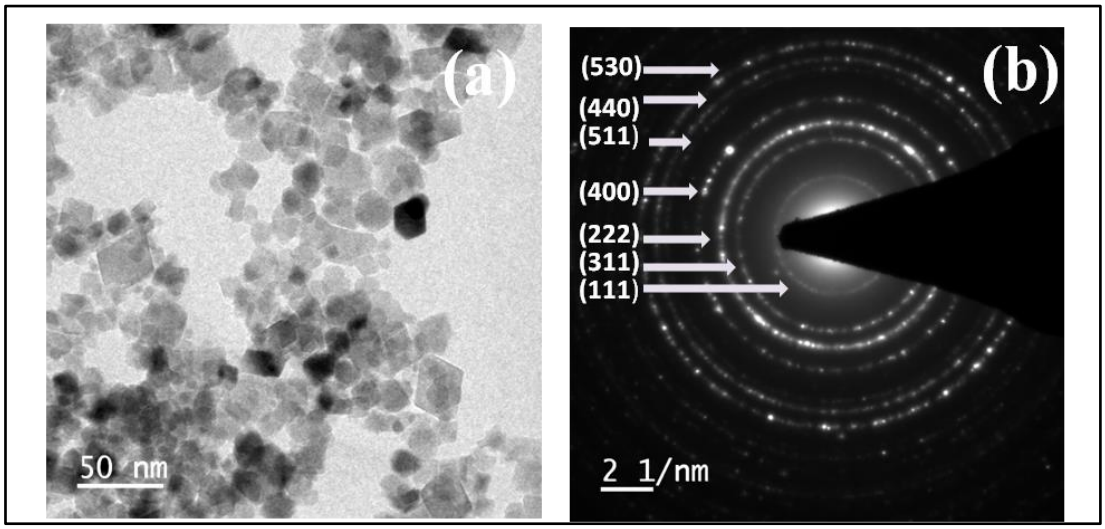

Fig. 4.4 Transmission electron micrograph (a) and SAED pattern (b) of cobalt ferrite nanoparticles.

4.3.1.4. Magnetization vs Magnetic field

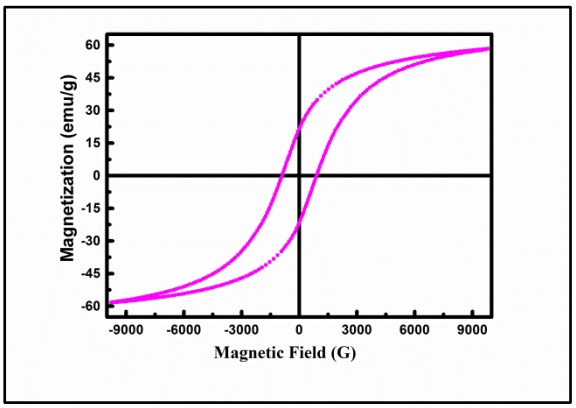

Fig. 4.5 Magnetization vs magnetic field curve of cobalt ferrite.

Fig. 4.5 shows the magnetization vs magnetic field curve of cobalt ferrite nanoparticles. The hysteresis loop of composites show a typical ferromagnetic behaviour of $CoFe_2O_4$ nanoparticles. The saturation magnetization of pure cobalt ferrite is found to be 58.5 emu g^{-1}.

4.3.2. Structural and morphological studies on graphene

Structural studies on graphene is carried out by using X-ray diffraction and Raman spectroscopy. The HRTEM is used for investigating the morphological behaviour of synthesized graphene nanosheets. The results of these studies are discussed in following subsections.

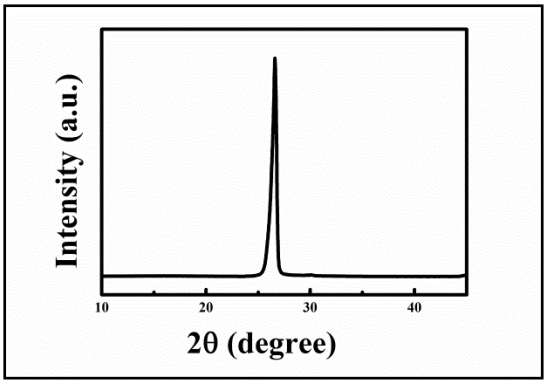

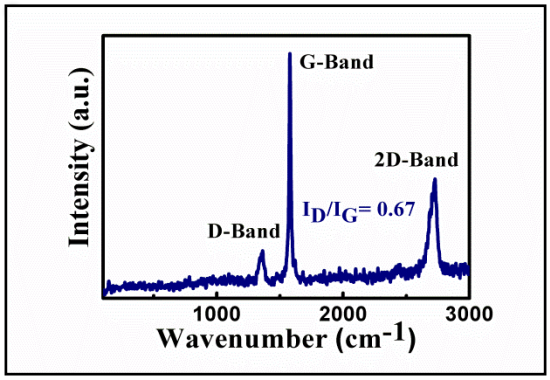

Fig. 4.6 X-ray diffraction of graphene.

Fig. 4.7 Raman spectra of graphene.

4.3.2.1. X-ray diffraction

Fig. 4.6 shows the XRD structure of graphene. Graphene exhibits a single intense peak at $2\theta = 26^0$ corresponds to (002) plane of graphitic carbon [25].

4.3.2.2. Raman Spectroscopy

Fig. 4.7 shows the Raman spectra of graphene at a wavelength of 5 40 nm; where three peaks at 1363 cm^{-1}, 1580 cm^{-1}, 2700 cm^{-1} are observed. Observed peaks at 1380 cm^{-1} and 2700 cm^{-1} corresponds to G-band and 2D-band respectively. G-band corresponds to E_{2g} mode is usually observed for sp^2 hybridised state of carbon in graphene and 2D-band is attributed to interaction of phonon with opposite momentum present in graphene [26]. The intensity ratio of 2D and G-band i.e. I_{2D}/I_G is usually used to find out the number of graphene layers [27]. In our case, $I_{2D}/ I_G \approx 0.67$; which confirm that the synthesized graphene nanosheets have less than 4 graphene layers.

4.3.2.3. High Resolution Transmission Electron Microscopy

Fig. 4.8 (a) shows the HRTEM image of layered graphene nanosheets. TEM image of graphene reveals the few layer graphene with large flakes. The average length, width and thickness of graphene layer are found to be ~ 293 nm, ~ 271 nm and ~ 20 nm respectively. The image also shows no aggregates of graphite. Fig. 4.8 (b) shows the SAED pattern of graphene.

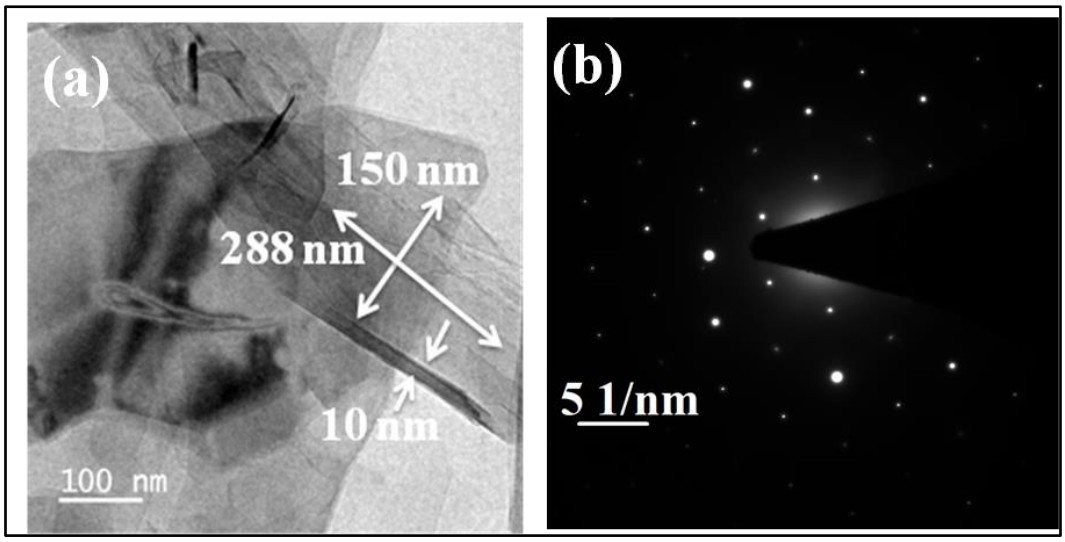

Fig. 4.8 Transmission electron micrograph of graphene nanosheets showing length, width and thickness of nanosheets (a) and, SAED pattern of graphene (b).

4.3.3. Structural, morphological and magnetic studies of polypyrrole-graphene-cobalt ferrite nanocomposites

Structural studies on nanocomposites have been carried out by using X-ray diffraction and fourier transform infrared spectroscopy. High resolution transmission electron microscopy (HRTEM) and vibrating sample magnetometer (VSM) have been used to investigate the morphological and magnetic behaviour of synthesized nanocomposites. The results of these studies have been given in following subsections.

4.3.3.1. X-ray diffraction

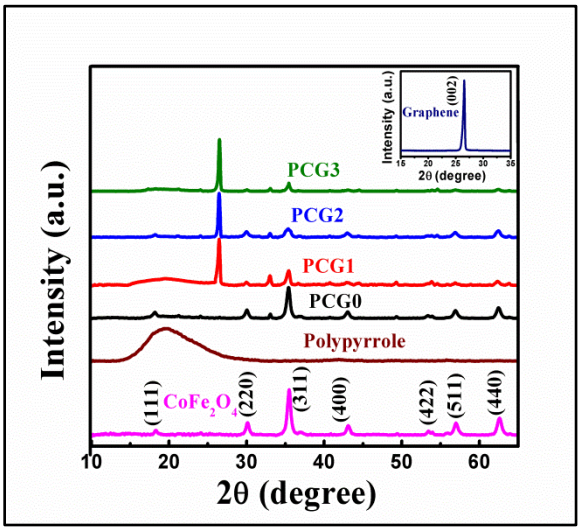

Fig. 4.9 X-ray diffraction plot of $CoFe_2O_4$, polypyrrole and PCG nanocomposites.

Fig. 4.9 shows the X-ray diffraction plot of $CoFe_2O_4$, polypyrrole and PCG nanocomposites. Single broad peak at $2\theta = 19.2^0$ reveals the amorphous nature of polypyrrole conducting polymer [9]. The characteristic peaks of polypyrrole, graphene and $CoFe_2O_4$ are clearly observed in XRD pattern of PCG nanocomposites; which confirms the inclusion of graphene nanosheets and $CoFe_2O_4$ nanoparticles in polypyrrole.

4.3.3.2. Fourier transform infrared spectroscopy

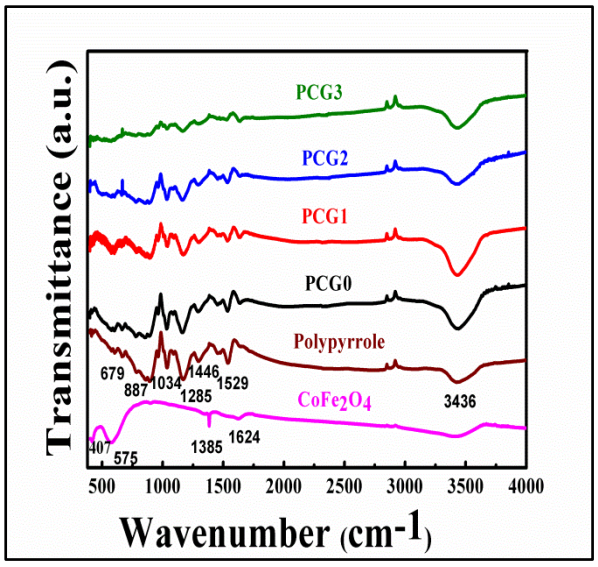

Fig. 4.10 Fourier transform infrared spectra of cobalt ferrite, polypyrrole and PCG nanocomposites.

Fig. 4.10 shows the FTIR spectra of the cobalt ferrite, polypyrrole and PCG nanocomposites. The peak observed at 1529 cm^{-1} and 1446 cm^{-1} are associated with antisymmetric and symmetric vibration of pyrrole ring respectively. The peaks at 1285 cm^{-1}, 1166 cm^{-1} and 1034 cm^{-1} are attributed to C-H in - plane deformation, C-N stretching vibrational mode and C-H in-plane deformation vibrational mode respectively. The C-H and C-C out of plane ring deformational vibrations are observed at 887 cm^{-1} and 679 cm^{-1} respectively. A broad peak at 3000-3500 cm^{-1} describes C-H and N-H stretching vibration [28]. The characteristic peak of $CoFe_2O_4$ observed at 574 cm^{-1} is shifted to 578 cm^{-1} which confirms the interaction of polypyrrole with ferrite [9]. The FTIR spectra of PCG composites show all the characteristic peaks of Polypyrrole and $CoFe_2O_4$.

4.3.3.3 High Resolution Transmission Electron Microscopy

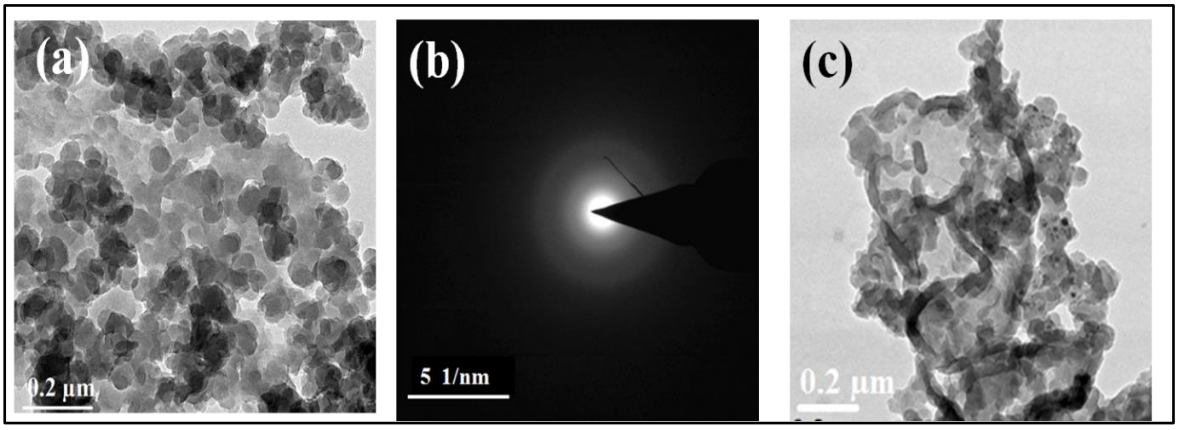

Fig. 4.11 (a, b) Transmission electron micrograph and SAED pattern of polypyrrole and (c) TEM image of nanocomposite.

Fig. 4.11 shows the HRTEM images of Polypyrrole and PCG nanocomposite. SAED pattern of polypyrrole shown in Fig. 4.11(b) is attributed to the amorphous nature of

polymer polypyrrole. TEM image of PCG composite (Fig. 4.11(c)) shows the distribution of small sized ferrite nanoparticles and graphene nanosheets along the chain of polypyrrole. This structure shows some rod like structure; which is coming due to rolling of graphene sheets along width during polymerization [29].

4.3.3.4. Magnetization vs magnetic field

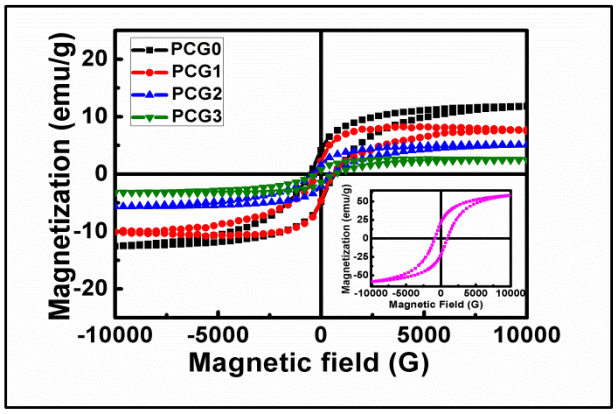

Fig. 4.12 Magnetization vs magnetic field induction (B) curve of PCG nanocomposite.

Fig. 4.12 shows the M-H loop of PCG nanocomposites. Polypyrrole and graphene show no magnetization because they are conducting and non magnetic in nature. The hysteresis loop of the nanocomposites show a typical ferromagnetic behaviour due to the presence of $CoFe_2O_4$ nanoparticles. Saturation magnetization value of 11.8 emu g^{-1} is exhibited by PCG0 nanocomposite with no loading of graphene. The saturation magnetization decreases from 11.8 emu g^{-1} to 2.4 emu g^{-1} with increase in graphene fraction by weight from 0 to 0.3 in PCG composites. The increased saturation magnetization with decrease in graphene content enhances the complex permeability of nanocomposites and increases the eddy current loss and natural resonance loss which is responsible for the enhanced magnetic loss [30].

4.3.4. Electrical and electromagnetic studies of polypyrrole-graphene-cobalt ferrite nanocomposites

The electrical and electromagnetic studies involve the dc conductivity and the electromagnetic shielding of synthesized polypyrrole-cobalt ferrite-graphene nanocomposites. The detailed analysis of microwave dielectric and magnetic behaviour as well as shielding effectiveness are carried out in X-band (8.2-12.4 GHz) of microwave region. The correlation of associated parameter such as skin depth, ac conductivity, attenuation constant and impedance matching of PCG nanocomposites with shielding effectiveness is also discussed. The detailed discussion of these results and, analysis have been described in subsequent sections.

Table 4.1 The electrical conductivity and saturation magnetization of polypyrrole, cobalt ferrite ($CoFe_2O_4$) and PCG nanocomposites.

Sample name	Ppy	$CoFe_2O_4$	PCG0	PCG1	PCG2	PCG3
Electrical conductivity(S/cm)	2.19	-	1.3	4.8	10.6	20.5
Saturation Magnetization (emu/g)	-	58.3	11.8	7.7	5.1	2.5

4.3.4.1. DC electrical conductivity

Polypyrrole - ferrite (PCG0) composite with no loading of graphene has least conductivity of ~ 1.34 S/cm because the magnetic particles are insulating in nature. They provide resistance and hinder the free flow of electrons within the composite and reduce the electrical conductivity of composite. The electrical conductivity for composite PCG3 is highest. The conductivity increases with increase in graphene content because graphene dispersed in polypyrrole matrix form a conducting network for free flow of electrons. The interfacial affinity between graphene and polypyrrole also increases the number of conductive path [31]. But, the increase of graphene content beyond 0.3% (w/w) is found to exhibit decrease in dc conductivity, which might be due to percolation threshold [32]. The electrical conductivity and saturation magnetization of polypyrrole, CoFe2O4 and PCG nanocomposites at room temperature are shown in Table 4.1.

4.3.4.2. Microwave dielectric, magnetic and electromagnetic interference shielding

The results of microwave dielectric and magnetic behaviour along with electromagnetic shielding are discussed in subsequent subsections.

4.3.4.2.1. Microwave dielectric and magnetic studies

The investigation of microwave dielectric and magnetic behaviour is essential for understanding the electromagnetic shielding behaviour of PCG nanocomposites. These studies provide information about dielectric and magnetic relaxation, which is affective the shielding effectiveness behaviour.

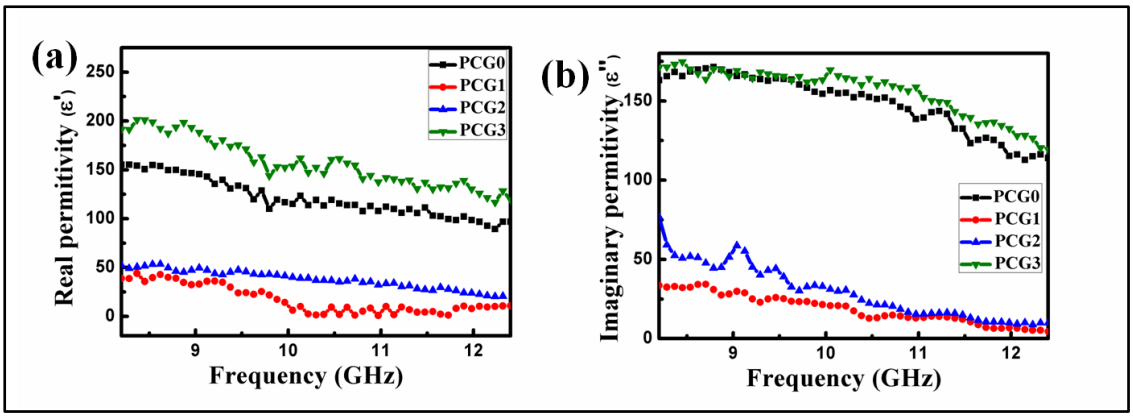

Fig. 4.13 Frequency dependence of (a) real (ε') and, (b) imaginary (ε'') part of permittivity of PCG nanocomposites.

Dielectric constant (ε') and dielectric loss (ε'') are found to decrease with frequency; for PCG composites. Values ε' and ε'' are increasing with increase in loading of graphene as shown in Fig. 4.13 (a, b). The value of ε' at 8.2 GHz for PCG3 composite is found to be highest i.e. ~ 200; whereas for PCG1 it is lowest i.e. ~ 50. The imaginary part of permittivity (ε'') for same sample i.e. PCG3 at 8.2 GHz is ~ 175. The increased loading of graphene in composite forms a large conducting network; enabling a reduction in resistivity and ε″ becomes higher with increasing content of graphene. The trend of variation of ε′ and ε″ is similar for all composites in the frequency range 8.2-12.4 GHz. The values of ε', ε'' and ac conductivity of PCG1, PCG2 nanocomposite are found to be less in entire spectrum of X-band; whereas the corresponding values of PCG3 nanocomposite are higher than PCG0 nanocomposite.

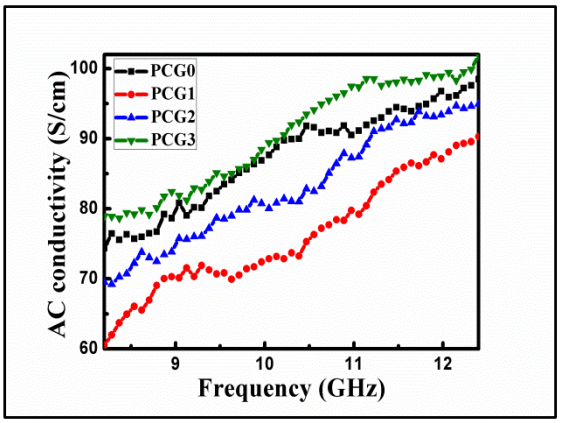

Fig. 4.14 Frequency dependence of ac conductivity of PCG nanocomposites in X-band.

The variation of AC conductivity with frequency is shown in Fig. 4.14. AC conductivity also increases with increase of graphene content in PCG nanocomposites. For PCG3 it is found to be highest; it is nearly equal to 85 S/cm at 8.2 GHz. The ac conductivity of PCG0 nanocomposite is smaller than PCG3 nanocomposite but it is larger than PCG1 and PCG2 nanocomposites.

When graphene loading is 0.3 (w/w); then percolation threshold is achieved [32]. The percolation threshold leads to formation of large number of micro capacitive network that increase the dielectric permittivity and, hence increases the ac conductivity.

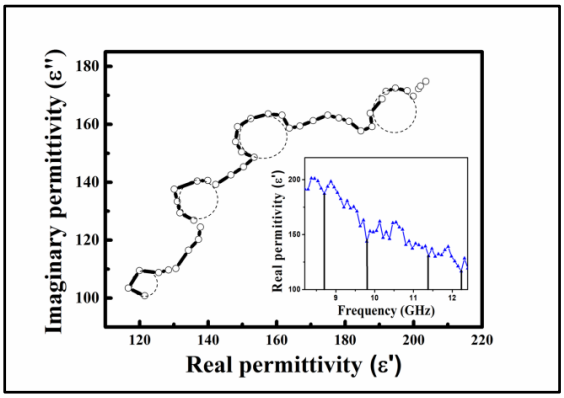

Fig. 4.15 Cole-Cole plot of PCG3 nanocomposite.

The contribution of interfacial polarization created by different interfaces among polypyrrole, cobalt ferrite and graphene in PCG nanocomposite also leads to the dielectric relaxation. The dielectric relaxation behaviour could be better understood within the frame work of Debye theory, which is explained is Sec. 3.3.3.2.1 of Chapter 3.

Debye relaxation behaviour is generally explained by the semicircles cantered around the frequency of dipolar relaxation in the ε' and ε"plot. The plots between ε' and ε" is called as Cole-Cole plot. Fig. 4.15 shows the Cole-Cole plot of PCG3 nanocomposite. The presence of four incomplete semicircles have been observed in the Cole-Cole plot of PCG3 nanocomposite. Each incomplete semicircle represent the dielectric relaxation. Semicircles centred around 8.6 GHz, 9.7 GHz, 11.3 GHz and 12.2 GHz have been observed for PCG3 nanocomposite. The fluctuation in dielectric constant, which resulting from fluctuation in polarization behaviour has also been observed around same frequencies. The variation of dielectric constant with frequency of PCG3 nanocomposite has been shown in inset of Fig. 4.15. Observation of semicircle is assigned to multiple relaxation which leads to enhanced microwave absorption of PCG nanocomposite.

Fig. 4.16 (a) and, Fig. 4.16 (b) show the variation of real permeability (μ') and imaginary permeability (μ'') for all nanocomposites. The graphene is a non-magnetic entity; but its inclusion in PCG nanocomposite might be creating interfacial magnetic domain; which increases the magnetic permeability slightly by virtue of changes in the edge state of graphene sheets at the interface [33]. The variation trend for all the samples is similar; it is found to fluctuate between 0.6 to 1.4 in X-band i.e. 8.2 – 12.4 GHz. Variation of μ'' is attaining a multi resonance peak at 11-12 GHz; which is attributed to small size effect,

surface effect and spin wave excitations where the resonance frequency is dependent on particle radius [9,33].

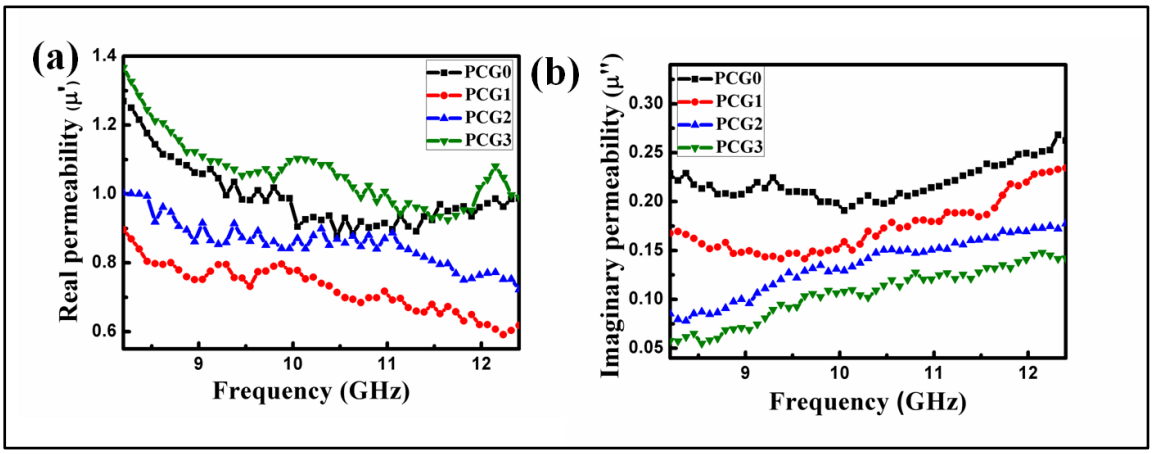

Fig. 4.16 Frequency dependence of (a) real (μ') and, (b) imaginary (μ'') part of permeability of PCG nanocomposites.

4.3.4.2.2. Electromagnetic interference shielding

The effect of loading of graphene in polypyrrole – cobalt ferrite - graphene (PCG) nanocomposite on shielding effectiveness is calculated from scattering parameters measured by a Vector Network Analyzer. The total SE is the sum of SE due to absorption (SE_A) and SE due to reflection (SE_R) which were calculated with formula [9]

$$SE_R = -10\log_{10}(1-R) \quad \text{.....(4.1)}$$

$$SE_A = 10\log(1-A_{eff}) = -10\log(T/1-R) \quad \text{.....(4.2)}$$

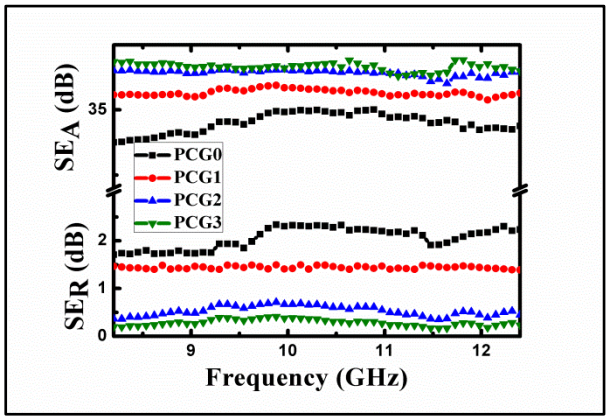

Fig. 4.17 The shielding due to absorption and reflection of PCG nanocomposites.

where R denotes the reflection coefficient, T denotes the transmission coefficient and A_{eff} denotes the effective absorption coefficient. Fig. 4.17 shows with increase in content of graphene in composite, shielding effectiveness by absorption (SE_A) increases and reflection (SE_R) decreases with frequency. SE_A for PCG3 composite is highest, whereas SE_R is lowest. SE_A for this composite is ~ 37

dB and it shows excellent frequency stability i.e. almost constant in X-band. The increase in graphene content is found to enhance the microwave absorption; which is attributed to increase in interfacial polarization. The combined effect of magnetic and dielectric loss (i.e. due to interfacial polarization) contributes to increase in microwave absorption [34]. The shielding effectiveness by reflection (SE_R) is found to be negligibly small for PCG3 where graphene nanosheets are taken as 0.3 weight fraction of polypyrrole, i.e. < 1 dB. Therefore, the contribution of shielding effectiveness by absorption is several times larger as compared to reflection.

Table 4.2 Shielding due to absorption, Shielding due to reflectance, dielectric and magnetic parameter of all the PCG nanocomposites at 8.2 GHz.

Sample Name	SE_A	SE_R	ε'	ε''	μ'	μ''
PCG0	30.20	0.79	155.20	163.17	1.20	0.22
PCG1	33.70	2.33	39.80	33.50	0.89	0.15
PCG2	35.50	1.49	52.30	76.72	1.01	0.08
PCG3	36.80	0.41	191.40	151.20	1.36	0.06

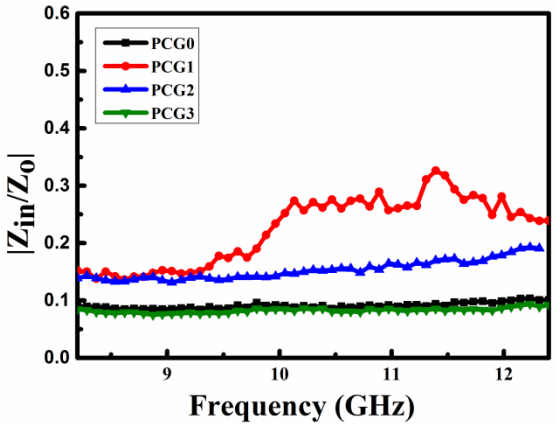

Fig. 4.18 Variation of $|Z_{in}/Z_o|$ of all PCG nanocomposites with frequency.

To further understand the causes of observed shielding effectiveness by absorption and reflection, the impedance and attenuation constant analysis have also been carried out. Reflection loss is usually calculated by following eqn [35]

$$R_L = 20\log\left|\frac{Z_{in}-Z_o}{Z_{in}+Z_o}\right| \text{.....(4.3)}$$

$$Z_{in} = Z_o\left(\frac{\mu_r}{\varepsilon_r}\right)^{1/2}\tanh\left\{j\left(\frac{2\pi f d}{c}\right)\left(\mu_r\varepsilon_r\right)^{1/2}\right\} \text{.....(4.4)}$$

where Z_{in} is the input impedance of absorber, Z_o is the impedance of air, f is the frequency of electromagnetic wave, d is the thickness of a microwave absorber and c is the velocity of light in vacuum. Fig. 4.18 shows the variation of $|Z_{in}/Z_o|$ with frequency

for all PCG nanocomposites. The values of all the PCG nanocomposites are less than 1 which is ascribed by decreased reflection loss of polypyrrole-graphene-cobalt ferrite nanocomposite. The value of reflection loss is less than 1 dB implying the best impedance matching. It is only possible if $1 < (Z_{in} - Z_o)/(Z_{in} + Z_o) < 2$. Hence, good impedance matching may be one of the cause of decreased reflection loss.

Attenuation constant of microwave is the property of effectiveness of material to attenuate the microwave exposed on it and is expressed as [36]

$$\alpha = \frac{\sqrt{2}\pi f}{c}\sqrt{(\mu''\varepsilon'' - \mu'\varepsilon') + \sqrt{(\mu''\varepsilon'' - \mu'\varepsilon')^2 + (\mu'\varepsilon'' + \varepsilon'\mu'')^2}} \quad \text{.....(4.5)}$$

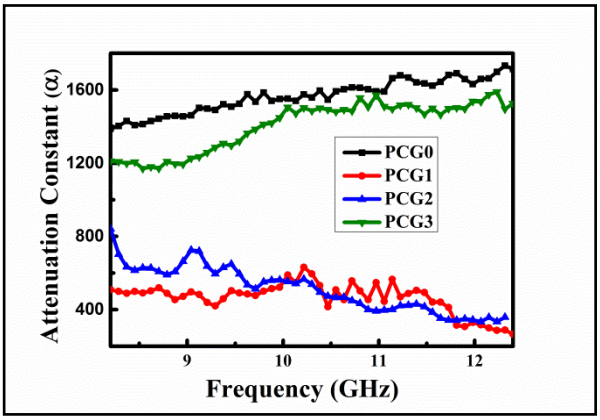

Fig. 4.19 Variation of attenuation constant with frequency in X-band.

Fig. 4.19 shows the attenuation constant (α) for all the PCG nanocomposites as a function of frequency in X-band. PCG3 nanocomposite shows the maximum attenuation constant of ~ 1211 at 8.2 GHz which results in higher ac conductivity and SE_A. The highest values of ac conductivity and SE_A for PCG3 sample are also confirming the inclusion of graphene in composite providing more interconnected regions, which in turn enhances the interfacial polarization helping in attenuation of microwave. The highest attenuation of PCG3 nanocomposite is attributed to increase in interfacial polarization and interconnected conducting network which is due to the conducting nature of graphene.

Thus microwave absorption is main contributor to total EMI shielding effectiveness for PCG composites. The dominance of shielding effectiveness by absorption is also reported for PANI/GN/MWCNT's and PS/GN/Fe_3O_4 composites [14,31]. In our case, the enhanced shielding effectiveness is attributed to following factors

1. Polypyrrole-graphene-cobalt ferrite composite enhances the interfacial polarization.
2. Presence of graphene in composite provides the internal connecting bridge for increase in conductivity and enhances the dielectric loss in electromagnetic field [31].

3. Embedded cobalt ferrite nanoparticles by being magnetic in nature enhance the magnetic loss.

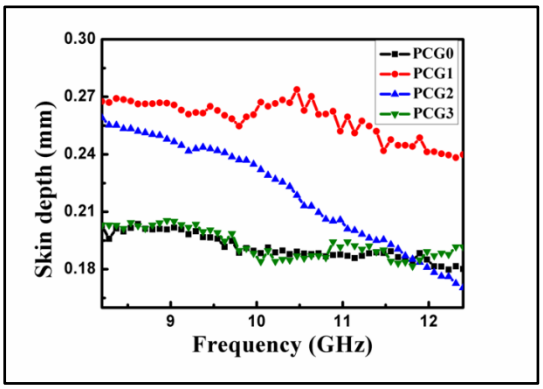

Fig. 4.20 Frequency dependence of skin depth of PCG nanocomposites in X-band.

The critical thickness of material required for practical applications is determined by the skin depth (δ) that depends on its magnetic permeability and electrical permittivity. It is reported that high performance of EMI shielding is achieved at thickness of sample beyond skin depth [5]. The skin depth vs frequency is plotted in Fig. 4.20. Skin depth decreases with the frequency for all the samples i.e. from PCG0 to PCG3. The value of skin depth is found to be lowest for PCG3 nanocomposite. The value of skin depth for PCG3 sample is found to vary from 0.12 mm to 0.2 mm in X-band. Therefore, 0.2 mm is optimum thickness to apply this material for practical applications.

For further understanding the microwave absorption behaviour of PCG composites, SE_A and SE_R are further analyzed in view of ac conductivity and skin depth and are given as

$$SE_A = 8.68t\sqrt{\sigma_{ac}\pi f \mu_0 \mu'} \quad \text{.....(4.6)}$$

$$SE_R(\text{dB}) = 10\log\left(\frac{\sigma_{ac}}{16\omega\varepsilon_0\mu'}\right) \text{.....(4.7)}$$

where μ_0, μ' and t are vacuum permeability, real permeability and sample thickness respectively.

SE_A is more dominant as compared to SE_R in X-band; which is ascribed to shallow skin depth and high conductivity at high frequencies [8]. Fig. 4.21 (a) shows variation of SE_A with $(\sigma_{ac})^{1/2}$, where SE_A decreases with $(\sigma_{ac})^{1/2}$. Higher values of conductivity are required for high SE due to reflection. Fig. 4.21(b) shows the plot of SE_R with conductivity. Observed high microwave absorption in PCG nanocomposites has also been analyzed by using magnetic and dielectric studies.

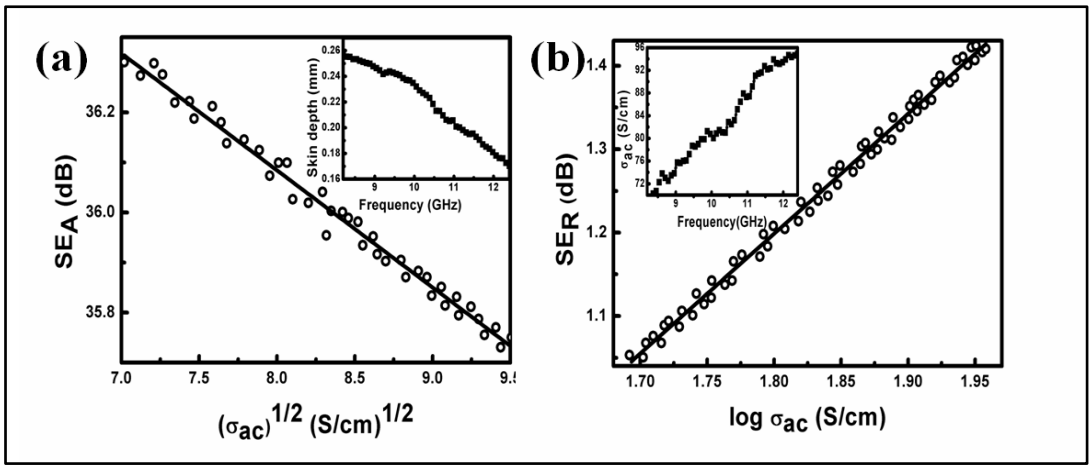

Fig. 4.21 (a) SE_A vs $(\sigma_{ac})^{1/2}$ of PCG2 nanocomposite and, (b) SE_R vs $\log\sigma_{ac}$ of PCG2 nanocomposite where σ_{ac} is the ac conductivity.

Table 4.3 Electromagnetic shielding efficiency and electrical conductivity of graphene based nanocomposites in X-band reported in literature.

S.No	Sample detail with filler loading	Thickness (mm)	SE_A (dB)	SE_R (dB)	Electrical Conductivity	Ref.
1.	15 wt% RGO in Conducting ferrofluid	3	34.23	7	0.1 S/cm	5
2.	25 wt% of $NiCoFe_2O_4$ in $NiCoFe_2O_4$-carbon black/poly(vinyl alcohol)	1.5	20	8	-	6
3.	2.24 vol% of graphene in Polystyrene/graphene/ Fe_3O_4	-	30	4	21 S/m	14
4.	30 wt% of GNP/Ni in GNP/Ni/Wax	0.7	29	11	3.139 S/cm	15
5.	5 wt% of functionalised graphene in Graphene/PVDF foam	-	20	-	10^{-4} S/m	19
6.	16 wt% of graphene in Polypyrrole/$CoFe_2O_4$/ graphene	2	37	1	20.5 S/cm	this work

The comparison of finding of earlier report on the parameters such as material thickness, SE_A, SE_R and electrical conductivity of various composite materials with polypyrrole-cobalt ferrite-graphene nanocomposites are shown in Table 2. The qualitative explanation of the microwave absorption and reflection of the polypyrrole-graphene-cobalt ferrite nanocomposites is discussed in following subsection.

4.3.4.2.2.1. Mechanism for observed microwave absorption and reflection

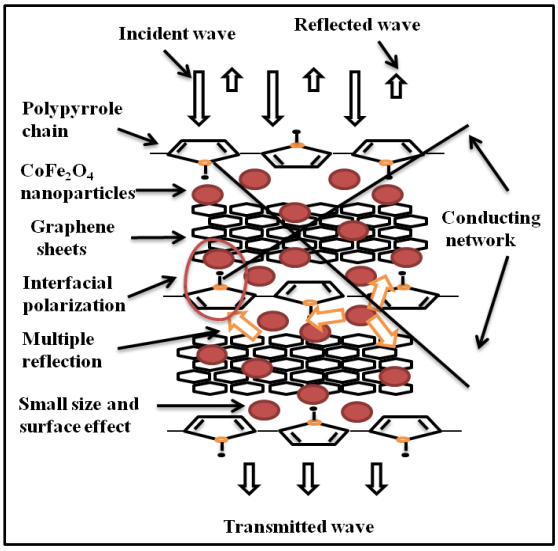

Fig. 4.22 Schematic representation of microwave absorbing mechanism of PCG nanocomposite.

The interfaces between polypyrrole/cobalt ferrite/graphene composite might be leading to multiple dielectric losses. Hence, analysis of dielectric and magnetic properties of PCG composites suggests that the inclusion of graphene increases the dielectric loss which is the main cause of increased shielding effectiveness due to absorption. The schematic representation of mechanism of microwave absorption and reflection, multiple reflection of nanocomposite is shown in Fig. 4.22.

4.4. CONCLUSION

The polypyrrole-cobalt ferrite-graphene (PCG) nanocomposites have been successfully synthesized by *in-situ* chemical oxidative polymerization. The dielectric permittivity, magnetic permeability and electromagnetic shielding behaviour in X band (8.2 GHz – 12.4 GHz) of PCG nanocomposites have been investigated. The shielding effectiveness by absorption (SE_A) and by reflection (SE_R) for PCG3 nanocomposite is found to be ~ 37 dB and ~ 1 dB respectively. Microwave absorption and reflection behaviour has been analyzed and, correlated with dielectric permittivity, magnetic permeability, skin depth and ac conductivity. Enhanced microwave absorption and suppressed microwave reflection is attributed to increased dielectric loss due to increase in interfacial polarization and, formation of conducting network in composite. Substantially enhanced microwave absorption and decreased reflection may be useful for defence applications and microwave communications.

REFERENCES

1 A. Balmori, *Pathophysiology*, 2009, **16**, 191–199.

2 X. Luo and D. D. L. Chung, *Compos. Part B Eng.*, 1999, **30**, 227–231.

3 K. Zhang, J. Luo, N. Yu, M. Gu and X. Sun, *J. Alloys Compd.*, 2019, **779**, 270–279.

4 D. D. L. Chung, *Carbon*, 2001, **39**, 279–285.

5 M. Mishra, A. P. Singh, B. P. Singh, V. N. Singh and S. K. Dhawan, *J. Mater. Chem. A*, 2014, **2**, 13159–13168.

6 G. Datt, C. Kotabage and A. C. Abhyankar, *Phys. Chem. Chem. Phys.*, 2017, **19**, 20699–20712.

7 N. Gandhi, K. Singh, A. Ohlan, D. P. Singh and S. K. Dhawan, *Compos. Sci. Technol.*, 2011, **71**, 1754–1760.

8 S. Varshney, A. Ohlan, V. K. Jain, V. P. Dutta and S. K. Dhawan, *Mater. Chem. Phys.*, 2014, **143**, 806–813.

9 M. Qiao, X. Lei, Y. Ma, L. Tian, K. Su and Q. Zhang, *Ind. Eng. Chem. Res.*, 2016, **55**, 6263–6275.

10 K. Manna and S. K. Srivastava, *ACS Sustain. Chem. Eng.*, 2017, **5**, 10710–10721.

11 P. Nimbalkar, A. Korde and R. K. Goyal, *Mater. Chem. Phys.*, 2018, **206**, 251–258.

12 N. C. Das, D. Khastgir, T. K. Chaki and A. Chakraborty, *J. Elastomers Plast.*, 2002, **34**, 199–223.

13 D. Munalli, G. Dimitrakis, D. Chronopoulos, S. Greedy and A. Long, *Compos. Part B Eng.*, 2019, **173**, 106906.

14 Y. Chen, Y. Wang, H.-B. Zhang, X. Li, C.-X. Gui and Z.-Z. Yu, *Carbon*, 2015, **82**, 67–76.

15 H. J. Im, G. H. Jun, D. J. Lee, H. J. Ryu and S. H. Hong, *J. Mater. Chem. C*, 2017,

5, 6471–6479.

16 D. X. Yan, H. Pang, B. Li, R. Vajtai, L. Xu, P. G. Ren, J. H. Wang and Z. M. Li, *Adv. Funct. Mater.*, 2015, **25**, 559–566.

17 H. Wang, G. Wang, W. Li, Q. Wang, W. Wei, Z. Jiang and S. Zhang, *J. Mater. Chem.*, 2012, **22**, 21232–21237.

18 A. Kolanowska, D. Janas, A. P. Herman, R. G. Jędrysiak, T. Giżewski and S. Boncel, *Carbon*, 2018, **126**, 31–52.

19 V. Eswaraiah, V. Sankaranarayanan and S. Ramaprabhu, *Macromol. Mater. Eng.*, 2011, **296**, 894–898.

20 Y. Wu, Z. Wang, X. Liu, X. Shen, Q. Zheng, Q. Xue and J. K. Kim, *ACS Appl. Mater. Interfaces*, 2017, **9**, 9059–9069.

21 B. V Bhaskara Rao, P. Yadav, R. Aepuru, H. S. Panda, S. Ogale and S. N. Kale, *Phys. Chem. Chem. Phys.*, 2015, **17**, 18353–18363.

22 K. Zhang, G. H. Li, L. M. Feng, N. Wang, J. Guo, K. Sun, K. X. Yu, J. B. Zeng, T. Li, Z. Guo and M. Wang, *J. Mater. Chem. C*, 2017, **5**, 9359–9369.

23 K. Sabira, M. P. Jayakrishnan, P. Saheeda and S. Jayalekshmi, *Eur. Polym. J.*, 2018, **99**, 437–444.

24 G. Allaedini, S. M. Tasirin and P. Aminayi, *Int. Nano Lett.*, 2015, **5**, 183–186.

25 D. Zhang, X. Zhang, Y. Chen, P. Yu, C. Wang and Y. Ma, *J. Power Sources*, 2011, **196**, 5990–5996.

26 A. C. Ferrari, *Solid State Commun.*, 2007, **143**, 47–57.

27 A. Eckmann, A. Felten, A. Mishchenko, L. Britnell, R. Krupke, K. S. Novoselov and C. Casiraghi, *Nano Lett.*, 2012, **12**, 3925–3930.

28 J. Lei, W. Liang and C. R. Martin, *Synth. Met.*, 1992, **48**, 301–312.

29 M. Calvaresi, M. Quintana, P. Rudolf, F. Zerbetto and M. Prato, *ChemPhysChem*, 2013, **14**, 3447–3453.

30 T. K. Gupta, B. P. Singh, V. N. Singh, S. Teotia, A. P. Singh, I. Elizabeth, S. R. Dhakate, S. K. Dhawan and R. B. Mathur, *J. Mater. Chem. A*, 2014, **2**, 4256–4263.

31 T. K. Gupta, B. P. Singh, R. B. Mathur and S. R. Dhakate, *Nanoscale*, 2014, **6**, 842–851.

32 M. Slota, A. Keerthi, W. K. Myers, E. Tretyakov, M. Baumgarten, A. Ardavan, H. Sadeghi, C. J. Lambert, A. Narita, K. Müllen and L. Bogani, *Nature*, 2018, **557**, 691-696.

33 V. P. Shilov, J.-C. Bacri, F. Gazeau, F. Gendron, R. Perzynski and Y. L. Raikher, *J. Appl. Phys.*, 1999, **85**, 6642–6647.

34 L. Jin, X. Zhao, J. Xu, Y. Luo, D. Chen and G. Chen, *RSC Adv.*, 2018, **8**, 2065–2071.

35 M. H. Al-saleh and U. Sundararaj, *J. Phys. D: Appl. Phys.* 2013, **46**, 035304.

36 S. P. Pawar, M. Gandi and S. Bose, *RSC Adv.*, 2016, **6**, 37633–37645.

CHAPTER 5

SUMMARY

AND

FUTURE WORK

5.1. INTRODUCTION

Carbon based nanofillers such as carbon nanotube, graphene and reduced graphene oxide etc. in polymer nanocomposites have recently been investigated and they are found to be good candidate for electromagnetic interference (EMI) shielding applications. EMI shielding is mainly governed by electromagnetic (EM) wave absorption and reflection. There are certain applications, where high microwave absorption along with less reflection is required such as defence and microwave communication etc. Present work is focussed to develop a material having high microwave absorption and low reflection. Therefore, the investigations on EMI shielding behaviour of graphene based polypyrrole nanocomposites have been carried out.

5.2. COMPONENT OF STUDY

The investigation on EMI shielding behaviour of graphene based polypyrrole nanocomposites have been carried out. These investigations consist of the following components.

5.2.1. Synthesis of materials

The synthesis of materials include synthesis of graphene nanosheets, cobalt ferrite nanoparticles, polypyrrole-graphene nanocomposites and polypyrrole-cobalt ferrite-graphene nanocomposites.

5.2.1.1. Synthesis of graphene nanosheets

Graphene nanosheets have been synthesized by liquid phase exfoliation of graphite flakes. The details have been given in the Sec. 3.2.1.1 and Sec. 4.2.1.2 of Chapter 3 and 4 respectively.

5.2.1.2. Synthesis of cobalt ferrite nanoparticles

The cobalt ferrite nanoparticles have been synthesized by hydrothermal method. The details are given in the Sec. 4.2.1.1 of Chapter 4.

5.2.1.3. Synthesis of polypyrrole-graphene nanocomposites

Polypyrrole-graphene nanocomposites have been synthesized by *in-situ* chemical oxidative polymerization. The details have been given in Sec. 3.2.1.2 of Chapter 3.

5.2.1.4. Synthesis of polypyrrole -cobalt ferrite- graphene nanocomposite

The polypyrrole-graphene-cobalt ferrite nanocomposites have been synthesized by *in-situ* chemical oxidative polymerization method. The details have been given in Sec. 4.2.1.3 of Chapter 4.

5.2.2. Structural and morphological studies

X-ray diffraction (XRD) and high resolution transmission electron microscopy (HRTEM) have been carried out to determine the crystalline phase and surface morphology of the nanoparticles and nanocomposites whereas Fourier transform infrared (FTIR) and Raman spectroscopy have been employed to understand the molecular and chemical bonding in synthesized materials (Sec. 2.3.1, Chapter 2).

5.2.3. Magnetic studies

Magnetic measurements have been done for studying the magnetic properties of cobalt ferrite nanoparticles and polypyrrole-graphene-cobalt ferrite nanocomposites (Sec. 2.3.2, Chapter 2).

5.2.4. Electrical and electromagnetic studies

The electrical and electromagnetic studies include the study of dc conductivity, microwave dielectric and electromagnetic interference (EMI) shielding properties of the synthesized material *viz.* graphene based polypyrrole nanocomposites. The details of these studies have been given in Sec. 2.3.3 of Chapter 2.

5.3. RESULTS

Results of structural, morphological, electrical and electromagnetic studies of graphene based polypyrrole nanocomposites are briefly summarized in the following sections.

5.3.1. Polypyrrole-graphene nanocomposites

This section gives the brief summary about the results of structural, morphological, electrical and electromagnetic studies of the polypyrrole-graphene nanocomposites.

5.3.1.1. Structural and morphological studies

The X-ray diffraction of polypyrrole shows a single broad peak which represents the amorphous nature of polypyrrole. The high resolution transmission electron micrograph of polypyrrole shows globular or spherical type structure (Sec. 3.3.2, Chapter 3). Graphene shows a single intense peak of graphitic carbon and the transmission electron micrograph shows the layered structure of graphene (Sec. 3.3.1.1, Chapter 3). Raman spectra demonstrated that the intensity ratios of D-band and G-band is ~ 0.34 which confirms the formation of multilayered graphene having number of layers less than 5 (Sec. 3.3.1, Chapter 3). Transmission electron microscopic image of nanocomposite shows the encapsulation of graphene with polypyrrole with polypyrrole chain (Sec. 3.3.2.4, Chapter 3).

5.3.1.2. Electrical and electromagnetic studies

The electrical and electromagnetic studies include the study of dc conductivity, microwave dielectric and, electromagnetic interference (EMI) shielding properties. Their results are summarized as follows.

5.3.1.2.1. DC electrical conductivity

DC electrical conductivity has been measured at room temperature and is found to increase by increasing graphene content in polypyrrole-graphene nanocomposites upto certain loading of graphene in nanocomposites i.e. 0.2 % w/w. With further increase of graphene, electrical conductivity start decreasing.

5.3.1.2.2. Microwave dielectric studies

Dielectric studies of polypyrrole-graphene nanocomposites include the dielectric permittivity and the relaxation behaviour of nanocomposites in X-band (8.2-12.4 GHz) of microwave region. The real permittivity decreases and imaginary permittivity increases with increase in graphene content in nanocomposites. Incorporation of graphene in polypyrrole matrix results in formation of number of interfaces, which contribute to the dielectric loss. The ac conductivity increases with graphene due to formation of conducting pathways; and multiple relaxation processes.

Debye relaxation results of nanocomposites have been observed by the Cole-Cole plots which show the incomplete multiple semicircles due to multiple relaxation behaviour.

The formation of large number of interfaces with polypyrrole and graphene in the nanocomposites is the main cause of multiple relaxation.

5.3.1.2.3. Electromagnetic interference studies

The electromagnetic interference (EMI) shielding results explain the shielding effectiveness due to absorption and reflection of microwave from the shielding materials. EMI shielding has been carried out in X-band (8.2-12.4 GHz) frequency range. Shielding due to absorption is found to be dominant over the shielding due to reflection in X-band. The maximum shielding due to absorption is found to be ~ 33 dB. The values of shielding due to reflection is nearly 1 dB for all the nanocomposites. Thickness of the shielding material is very important for microwave absorption and the minimum thickness of the shielding material is decided by the skin depth. The value of minimum skin depth is found to be ~ 250 μm.

The attenuation constant is parameter related with ability of material to attenuate the microwave. Increased value of attenuation constant with graphene is caused by large number of interfaces and high dielectric loss. At high frequency range, the increased absorption with decreased reflection is required for many applications such as microwave communication and stealth technology in defence etc.

5.3.2. Polypyrrole-cobalt ferrite-graphene nanocomposite

The results of structural, morphological, electrical and electromagnetic studies of the polypyrrole-cobalt ferrite and graphene nanocomposites are briefly summarized as follows.

5.3.2.1. Structural and morphological studies

X-ray diffraction of cobalt ferrite confirms the formation crystal structure and shows the crystalline size of ~ 17 nm. Transmission electron microscope shows the semi spherical particles with some agglomeration and particle size was found to be ~ 21 nm (Sec. 4.3.1, Chapter 4). Raman studies confirm the formation of multi layered structure of graphene. Transmission electron micrograph of graphene shows the layered structure with large flakes (Sec. 4.3.2, Chapter 4).

Fourier spectra shows a shift of characteristic peak of cobalt ferrite in nanocomposites due to interaction of polypyrrole with ferrite at lower wavenumber. Transmission electron

microscopic image of nanocomposite shows the distribution of small sized ferrite particles and graphene sheets along the chain of polypyrrole (Sec. 4.3.3, Chapter 4).

5.3.2.2. Magnetic studies

Saturation magnetization of cobalt ferrite is found to be ~ 58.5 emu/g which confirm the formation of cobalt ferrite nanoparticles. The saturation magnetization of polypyrrole-graphene-cobalt ferrite nanocomposites are found to be less as compared to that of cobalt ferrite, but it increases with increase in the loading of cobalt ferrite in nanocomposites (Sec. 4.3.3.4, Chapter 4).

5.3.2.3. Electrical studies

The electrical conductivity of the nanocomposites have been studied at room temperature. Graphene is highly conducting in nature and form conducting pathways for charge carriers to move. The conductivity of nanocomposites increases with increase of graphene content in nanocomposites.

5.3.2.4. Electromagnetic studies

The effect of loading of graphene in polypyrrole-cobalt ferrite-graphene nanocomposite has been studied in X-band. The shielding due to absorption is found to be maximum and shielding due to reflection is found to be minimum. The maximum shielding effectiveness due to absorption is found to be ~ 37 dB and shielding due to reflection is less than 1. The thickness of material has been investigated by skin depth of the nanocomposites. The optimum thickness for the polypyrrole-cobalt ferrite-graphene nanocomposite is found to be 0.2 mm. AC conductivity of the nanocomposites confirm the inclusion of graphene to form interconnected network. It increases the interfacial polarization which enhances the shielding due to absorption of the nanocomposite.

The dielectric permittivity and magnetic permeability studies have been done to investigate the role of dielectric and magnetic materials in nanocomposites. Presence of graphene increases the conducting network which increases the dielectric loss and presence of cobalt ferrite enhances the magnetic loss. The observation of dielectric and magnetic loss ensure the increase in absorbance of shielding material (Sec. 4.3.4.2, Chapter 2).

5.4. CONCLUSIONS

The important conclusions drawn from the present investigations are briefly summarized in the following subsections.

5.4.1. Polypyrrole-graphene nanocomposites

Graphene is synthesized by liquid phase exfoliation method. Transmission electron micrograph of graphene show the layered structure. Raman spectra confirms the formation of multilayered graphene by analysing the intensity ratios of D-band and G-band, which confirms the formation of graphene having less than 5 layers. Polypyrrole-graphene nanocomposite is successfully, synthesized by *in-situ* chemical oxidative polymerization method. Synthesis of the nanocomposite is aimed to develop a novel material in order to study the EMI shielding behaviour in X-band (8.2-12.4 GHz) of microwave region.

The transmission electron micrograph of nanocomposite shows the encapsulation of graphene by the polypyrrole. The analysis of electrical studies confirms the increase in electrical conductivity with increase in graphene content in polypyrrole-graphene nanocomposites upto certain loading of graphene in nanocomposites i.e. 0.2 % w/w. With further increase of graphene, electrical conductivity start decreasing.

Dielectric studies has been done to investigate the effect of permittivity on electromagnetic shielding of nanocomposites. The analysis of the dielectric behaviour by Debye relaxation mechanism shows multiple relaxation behaviour due to formation of large number of interfaces and interfacial charges in nanocomposites.

The analysis on electromagnetic shielding of polypyrrole-graphene nanocomposite has been done in X-band frequency range. The maximum shielding effectiveness due to absorption is found to be ~ 33 dB. The shielding effectiveness due to reflection for all the samples are found to be nearly 1 dB. Shielding due to absorption is dominating over shielding due to reflection. The minimum skin depth for the shielding material is ~ 250 µm which is the minimum thickness required for material to be used for shielding purposes in X-band. Enhanced microwave absorption of polypyrrole-graphene nanocomposite is attributed to increased dielectric loss arising due to conducting pathways, interfacial polarization and multiple relaxation.

5.4.2. Polypyrrole-cobalt ferrite-graphene nanocomposite

Cobalt-ferrite nanopowder is synthesized by hydrothermal method. X-ray diffraction confirms the crystalline nature of cobalt ferrite. High resolution transmission electron micrograph of cobalt ferrite confirms the semi spherical particles and the mean particle size is found to be ~ 21 nm. The magnetic properties have been determined by the magnetization *vs* magnetic field intensity hysteresis curve of cobalt ferrite nanoparticles.

Polypyrrole-cobalt ferrite-graphene nanocomposite is synthesized by *in-situ* chemical oxidative polymerization method. The synthesis of this nanocomposite is aimed to investigate the effect of graphene on the electromagnetic shielding properties of ferrite based polypyrrole nanocomposites in X-band (8.2-12.4 GHz) of microwave region.

Transmission electron microscopic image confirms the distribution of ferrite particles and graphene along polypyrrole chain. A increase in conductivity is observed in nanocomposites with the loading of graphene. Graphene is highly conducting and forms a conducting network for free flow of electrons.

The analysis of data shows that the inclusion of graphene in the polypyrrole-cobalt ferrite-graphene nanocomposites leads to the increased shielding due to absorption with suppressed reflection. The role of dielectric permittivity and magnetic permeability are very important for understanding the shielding effectiveness behaviour. The dielectric loss increases with increase in graphene content in the nanocomposites. The graphene enhances the dielectric loss by providing internal connecting bridge due to conductivity and cobalt ferrite enhances the magnetic loss. The polypyrrole-cobalt ferrite-graphene nanocomposite exhibited the shielding effectiveness due to absorption and reflection as ~ 37 dB and 1 dB respectively. Microwave absorption and reflection behaviour have been analyzed and, correlated with dielectric permittivity, magnetic permeability, skin depth and ac conductivity. Enhanced microwave absorption with suppressed microwave reflection is attributed to increased dielectric loss due to increase in interfacial polarization and, formation of conducting network in composites. The optimum thickness for polypyrrole-cobalt ferrite-graphene nanocomposites i.e. skin depth is 0.2 mm for all practical applications. The polypyrrole-cobalt ferrite-graphene nanocomposites have been found to be an excellent microwave absorbing material.

5.5. FUTURE SCOPE OF THESIS

Based on the present study, there are many areas of interest which may be suggested for future research work. A material having good dielectric and magnetic properties with moderate conductivity is found to be suitable for shielding applications. The work presented in thesis is centred on the development of EMI shielding material, which have very good microwave absorbance and minimal reflection. But the improvement in processing condition and interfaces, in the graphene based polypyrrole nanocomposite could provide more insight towards which would be important from academic, scientific and technological point of view. Therefore, some of the areas of interest are suggested as follows.

1. Effect of decoration of graphene by various transition metal oxides such as MnO_2, TiO_2 etc. and other functional groups, in the graphene based polypyrrole nanocomposite may create additional interfaces which may lead to improved microwave dielectric behaviour as well as absorption behaviour. This has to be further investigated.
2. Variation of size and shape of nanoferrites (such as nanorod, nanowire, nanotubes) and its functionalization with different functional group e.g. $–NH_2$, $-SO_3H$, -OH in graphene based polypyrrole nanocomposites could also yield improved microwave shielding effectiveness. This also has to be investigated.
3. The investigation on different form of polypyrrole i.e. acidic, basic, doped etc. in graphene based polypyrrole nanocomposites on shielding effectiveness and various other associated properties in microwave frequency range is also important due to change in conducting behaviour of polypyrrole in the nanocomposites.